

MAGNETO-OPTICAL TRAPPING OF
POTASSIUM ISOTOPES

by

Robert Sylvester Williamson III

A dissertation submitted in partial fulfillment
of the requirements for the degree of

Doctor of Philosophy
(Physics)

at the

UNIVERSITY OF WISCONSIN – MADISON

1997

Abstract

We have demonstrated a magneto-optical trap (MOT) suitable for capturing radioactive potassium produced on-line with the UW-Madison 12 MeV tandem electrostatic accelerator. To do this, we made and characterized the first MOT for potassium, measured the potassium ultracold collision rate, and developed a numerical trap-loading rate model that makes useful quantitative predictions. We have created a cold beam of collimated potassium atoms using a pyramidal magneto-optical funnel and used it to load a long-lifetime MOT operating at ultrahigh vacuum. We have also built a target that produces a beam of radioactive ^{37}K and ^{38}K and coupled it to the magneto-optical funnel and trap. Once a trap of radioactive ^{38}K has been demonstrated, the primary goal of this project is to measure the beta-asymmetry parameter in the decay of ^{38}K , performing a sensitive test of the Standard Model of weak interactions.

Acknowledgments

I owe a great debt to many people for their help and encouragement throughout my years here in Wisconsin. Chief among them of course is my advisor, Thad Walker, who took me on as one of his first students in the summer of 1990. Working with Thad has been a tremendous learning experience and he has given me many opportunities and challenges. Thank you for taking me on as your student and for giving me the opportunity to work on this project.

I am also grateful to Paul Quin for collaborating with us on this project and for providing his nuclear physics expertise and for making the nuclear group's facilities available. This project would not have been possible without him.

Paul Voytas, who joined this collaboration as a post-doc about two years ago, provided both the inspiration and perspiration to create radioactive potassium isotopes on-line. I have enjoyed working with him tremendously. His positive attitude and good spirits have made the past few demanding months of this project much more bearable. Of course, he has taught me many things through his experimental skills and knowledge of nuclear physics. His dedication has been unflagging and I thank him for the long hours he has logged.

Paul Feng and Dominik Hoffmann, both fellow graduate students, have been great friends and colleagues throughout the years. Paul Feng provided youthful and mirthful distractions from the seriousness of laboratory work. He encouraged my "wind addiction" and kept me up-to-date on sports, music, movies, and other irrelevant events. Dominik defies a concise description, both personally and professionally. With his wry sense of humor, he managed to fool nearly everyone with outrageous but nearly believable stories. On the more serious side, his construction abilities and attention to detail in the lab were both useful and inspiring. I've thoroughly enjoyed the time spent working with both of these guys in the labs, building and learning.

Renée Nesnidal's energy, humor, and thoughtfulness has brought a lot of joy to

the lab and made long afternoons in the dark a bit more fun. Together we've taught each other some physics (remember "Stupid Question Club"?), burned time playing a variety of games ("Drag"*), and had some refreshingly good conversations about life beyond graduate school. Her exceptional memory, clear understanding of numerous physics concepts, and patient willingness to explain them to us won't be soon forgotten.

Charles Sukenik has been one of the most entertaining people I've worked with in the department. I've never known someone with such a quick, biting wit who was also so very caring and concerned about his fellow workers. He is indeed the most dedicated physicist I've worked with, and of course I wish him the greatest success as Professor Ira at Old Dominion University. His late-night visits to my office these past few months have provided me with lots of encouragement and entertainment.

Steve Kadlecik's sundry abilities and kind temperament have made him a pleasure to work with. He has a keen, inquisitive mind and isn't afraid to ask tough questions. He has helped me to understand some of the subtleties of quantum mechanics. Ian Nelson's mellowness and good humor have made the lab a better place.

I have also enjoyed working with visiting exchange students Stefan König from Germany and Michiel Peters from the Netherlands. Their outlook gave me a fresh perspective on life and America. So too did our post-doc Samir Bali, who shared sundry stories of India and Rochester, New York.

There are many others in the department who make our work so much easier, and Ed Sloten easily tops this list. His willingness to jump bureaucratic hurdles for us has made years of buying stuff and dealing with unresponsive companies so much easier. His assistants through the years, Jesse Prochaska, Jean LeBeck, Louise Olbrantz, and Karen Fiene, have all been kind and helpful. I would also like to thank all of the physics department staff, especially Barb Schutz, Melody Schneeberger, and Pat Cady for all of their assistance.

Special thanks goes to Mike Gerber for a fine job of machining the rather complex copper pyramid pieces. I'd also like to thank Lee Potratz, Norbert Meier, and Dave Guitzkow for other machine work they've contributed to this project. Of course, Walt Wigglesworth and even Art Fritsche deserve credit for assistance in the student machine shop. Some of our electronics were built by the folks in the electronics shop, Mike Murray, Jerry Glowacki, and Art Webb.

*A person, usually a graduate student (often Renée), is dragged on a sheet of teflon down the freshly-waxed halls of Sterling's third floor.

To all my friends and roommates, past and present, thank you. You have been wonderful and I've enjoyed hanging out with you in Madison.

Madison is a wonderful, beautiful city and has provided a wonderful setting to grow and learn outside of the realm of physics. Summer is especially pleasant, but even in the cold winter months there is always something to do amid the stark beauty of piled snowflakes.

To my wonderful and loving parents I owe so much gratitude. You have patiently educated, provided, and cared for me. Thank you for supporting my decision to study physics in Madison.

Finally, to my partner in life, Melissa Erin Gower, thank you. Your ability these past few months to understand, forgive, and love has been superhuman. What a wonderful fate to have my soul brought into your loving care!

Contents

Abstract	i
Acknowledgments	ii
List of Figures	viii
1 Introduction	1
1.1 Overview	1
1.2 Motivation	2
1.3 Magneto-optical trapping	3
1.3.1 Spontaneous force and viscous damping	3
1.3.2 Confinement	4
1.4 Summary of achievements	7
2 Trapping of natural potassium	9
2.1 Introduction	9
2.2 Background	9
2.3 Vapor-loading	13
2.4 Six-level model	15
2.4.1 Populations	17
2.4.2 Forces	18
2.4.3 Loading rates	19
2.5 Apparatus	21
2.6 Results	22
2.6.1 Method	22
2.6.2 Loading measurements	23
2.6.3 Trap temperature	26
2.7 Conclusion	27
3 Ultracold Collisions	29
3.1 Introduction	29
3.2 Background	29
3.3 Measurement technique	31

3.4	Results	34
4	Beam-loaded MOT	38
4.1	Introduction	38
4.2	Atomic beams	38
4.2.1	Angular distribution	38
4.2.2	Velocity distribution	41
4.3	Atomic beam collimation and slowing	41
4.3.1	Introduction	41
4.3.2	Some approaches	42
4.3.3	Direct loading with collimation	44
4.4	Apparatus	44
4.4.1	Overview and Optical system	44
4.4.2	Vacuum chamber	46
4.4.3	Magnetic field coils	46
4.5	Results	50
4.5.1	Loading and effect of collimation	51
4.5.2	Slowing laser	52
4.5.3	Trap lifetime	54
5	Magneto-optical funnel	56
5.1	Introduction	56
5.2	Background	57
5.3	Description	59
5.4	Apparatus	61
5.5	Measurements	66
5.5.1	Pyramidal MOT	66
5.5.2	Pyramidal Funnel	68
5.6	Summary	72
6	Radioactive Isotopes of Potassium	73
6.1	Introduction	73
6.2	Background	74
6.3	Radioactive potassium	79
6.3.1	Hyperfine structure	79
6.3.2	Zeeman structure	81
6.3.3	Trapping of ^{40}K	84
6.4	System description	86
6.4.1	Target	86
6.4.2	Transport	91
6.4.3	Vacuum system	92
6.4.4	Optical system	98

6.5	System efficiency	101
6.5.1	Target and transport yields	101
6.5.2	Pyramid loading rates	103
6.6	Preliminary results	104
7	Conclusions and Outlook	108
A	Stabilized titanium-sapphire laser	111
A.1	Laser cavity	111
A.2	Stabilization	113
A.3	Saturated absorption spectroscopy	116
B	Ultrasensitive detection scheme	118
C	Procedure for coating glass with SC-77 dryfilm coating	122
	Index	133

List of Figures

1.1	Zeeman level splitting in a $J = 0 \rightarrow J = 1$ atom	5
1.2	Three-dimensional magneto-optical trapping scheme	6
2.1	Energy levels and laser tuning for trapping ^{39}K and ^{41}K	11
2.2	Force versus velocity model results for ^{39}K	12
2.3	Definition of levels and laser detuning for six-level model	16
2.4	Vapor-loaded potassium MOT apparatus	21
2.5	Measurements of N , ℓ , n , and Γ versus detuning Δ for ^{39}K	24
2.6	Loading rate versus trap beam diameter and intensity	25
2.7	Trap temperature determination by release and recapture technique	26
3.1	Total collision rate Γ versus trap density n for ^{39}K	32
3.2	Trap loading transient	34
3.3	Collisional rate coefficient β versus detuning Δ for ^{39}K	35
4.1	Geometry of cylindrical channel orifice	39
4.2	Integrated flux fraction versus cone angle	40
4.3	Atomic beam collimation and trapping schematic	45
4.4	Plan of main chamber vacuum system	47
4.5	Magnetic field configuration for beam collimation	49
4.6	Loading rate of ^{39}K into beam-loaded trap	51
4.7	Effect of slowing beam on trap loading rate	53
4.8	Loss rate transient for ^{41}K with no loading	54
5.1	Detail of the pyramidal funnel	60
5.2	Photo of pyramid (top view)	62
5.3	Photo of pyramid (bottom view)	63
5.4	Exploded view showing components of the pyramidal cell	64
5.5	Magnetic field configuration for funnel-loaded trap	65
5.6	CCD camera image of potassium trapped in pyramidal funnel	67
5.7	Schematic of complete radioactive trapping apparatus	69
5.8	Loading rate of ^{39}K into main MOT from vapor-loaded funnel	70
5.9	Main trap loading rate and lifetime versus funnel pressure	71

6.1	Nuclear β -decay scheme for three potassium nuclei	75
6.2	Energies of $^{37-41}\text{K}$ hyperfine levels	78
6.3	Trapping laser tuning schemes for various isotopes of potassium	80
6.4	Table of Landé g -factors for $^{37-41}\text{K}$	82
6.5	Zeeman sublevels of $P_{3/2}$ and $S_{1/2}$ levels of $^{38-41}\text{K}$ for $B = 10\text{ G}$	83
6.6	Loading rate of ^{40}K into effusive beam-loaded trap	85
6.7	Original radioactive oven design of Ames et al. [1965]	87
6.8	Radioactive target schematic	89
6.9	Photo of target flange assembly	90
6.10	Photo of target chamber assembly	93
6.11	Detail drawing of target/funnel vacuum system plan	94
6.12	Gas load analysis schematic	95
6.13	Laser optical table layout	100
6.14	Beta spectrum of ^{38}K	102
A.1	Schematic layout of $\text{Ti:Al}_2\text{O}_3$ cavity	112
A.2	Block diagram of laser locking scheme	114
A.3	Table of saturated absorption transitions in ^{39}K	115
A.4	Saturated absorption spectra of ^{39}K and ^{41}K D_1 transition.	117
A.5	Saturated absorption spectra of ^{39}K and ^{41}K D_2 transition.	117
B.1	Atomic level scheme for ultrasensitive blue photon detection.	120

Chapter 1

Introduction

1.1 Overview

In this dissertation I describe a series of experiments involving the magneto-optical trapping of various potassium isotopes that ultimately culminate in the design and test of an apparatus to create a beam of radioactive potassium that we attempt to trap. This chapter provides a motivation for this experiment, some essential background material on the operation of optical traps, and a brief summary of my accomplishments over the past few years.

In chapter 2, I describe the first magneto-optical trap ever made for the alkali potassium and measurements of the vapor-loaded trap properties. I also discuss some details of the structure of potassium that make it unique among the alkalis. Chapter 3 complements the characterization of a potassium MOT by adding the first measurements of ultracold collisions between potassium atoms.

The following chapters describe our steps toward creating a radioactive beam-loaded trap. In chapter 4, I summarize my experiments with a beam-loaded natural potassium MOT, including optical collimation and slowing of the atomic beam. In chapter 5, I describe a novel atomic funnel that produces a cooled, collimated atomic beam from a potassium vapor cell and how we couple it to load a high-vacuum MOT.

Next I describe the production of a neutral, radioactive beam of potassium atoms using the UW tandem electrostatic accelerator in chapter 6. I discuss the integration of our apparatus and the target, total system efficiency measurements, and our attempts to trap radioactive potassium. Finally, in chapter 7 we summarize our accomplish-

ments to date and outline the exciting experiments planned for the radioactive trap once it is working.

Three appendices give experimental details of our stabilized titanium-sapphire ring laser, an ultra-sensitive detection scheme for detecting trapped atoms, and the dryfilm coating procedure used to create our vapor-cell funnel.

1.2 Motivation

The control and precision measurement of atomic states benefitted in the 1930's from new atomic beam methods, in the 1950's by the development of ultra-high vacuum techniques, and in the 1960's by the invention of the laser. These technologies gave experimental spectroscopists superb control over the internal states of atoms, but measurements were soon limited by the thermal nature of their beams as well as the line-broadening (and shifting) effects of collisions. Now, with a deeper understanding of the mechanical effects of light, the external state of an atom can be controlled, giving us the ability to cool and confine it to temperatures near absolute zero.

Eleven years ago, when the first magneto-optical trap (MOT) for sodium was created by Chu et al. [1986], no one could have predicted the astounding influence it would have on the atomic and optical community. The MOT is rapidly becoming a tool, a standard atomic physics apparatus in many labs, on its way to becoming as ubiquitous as atomic beam experiments have been for decades.

Our unique role for this technique is in an attempt to create a magneto-optical trap for radioactive potassium isotopes. We choose potassium not only because it is an alkali and thus has a relatively simple level structure, but also because its radioactive isotopes ^{37}K and ^{38}K are good candidates to make interesting precision beta-decay measurements.

Currently these types of experiments are limited by poor or unknown sample spin polarization. By using a MOT, we are able to create a dense, spatially confined sample of radioactive atoms that can be fully spin-polarized in an environment that is relatively free from radioactive backgrounds. This gives us the unique ability to measure the angular distribution of the emitted beta particles with high precision. The asymmetry in the angular distribution is a measure of the nature of the weak charged currents, an important test of the standard model of weak interactions. This measurement complements a variety of experiments in weak interaction physics done at large

accelerator facilities like CERN and Fermilab.

Previous methods of measuring the asymmetry are usually limited by poor statistics rather than systematic errors, which usually enter at the 1% level. The decaying sample has low polarization (typically $P = 5\%$) that is usually measured using a γ -ray with a feeble branching ratio (typically $f = 2\%$). However, in our scenario the trap is optically spin polarized to 100% and we can measure it precisely with optical techniques, further reducing the number of events N necessary to achieve good statistics. The statistical error in the asymmetry measurement roughly goes as $(N/f)^{-1/2}/P$; to get 1% statistics with a trapped sample we need less than 10^4 counts, whereas the conventional experiments would require more than 10^8 counts.

1.3 Magneto-optical trapping

In this section I briefly review the mechanics of trapping, describe how the spontaneous light force can be used to slow and cool an atom, and how one can create a spatially confining force by exploiting the internal structure of the atom.

1.3.1 Spontaneous force and viscous damping

Let's begin by considering this simple system: a two-level atom at rest and in its ground state is illuminated by a single beam of resonant, single-frequency laser light propagating to the right (in the $+\hat{i}$ direction). At some point, the atom will absorb a photon from the laser and will be put into its excited state. In the process, it receives a momentum kick to the right of $+\hbar k$.

Soon after, the atom relaxes, re-emitting the absorbed photon either through spontaneous or stimulated emission. If the emission is stimulated by the laser, the photon is ejected with momentum $+\hbar k\hat{i}$ in the same direction as the laser beam and the atom receives no net push. But if the photon is emitted spontaneously, its direction is random and therefore isotropic, on average leaving the atom with some net momentum. Over many cycles of absorbing laser light of momentum $+\hbar k\hat{i}$ and emitting spontaneously in any direction, the emitted photon momenta average to zero and the atom receives a net push from the laser. This is often called the “scattering force” since it results solely from the fact of the atom scattering photons.

A two-level atom illuminated by a single-frequency laser can spontaneously scatter

photons only as fast as its excited-state lifetime τ will allow, a maximum rate of $1/2\tau$. Each photon imparts a velocity $\hbar k/m$ to the atom where m is the atomic mass, giving a maximum acceleration $\hbar k/2m\tau$. For the the D transitions in the alkalis, $\tau \approx 20$ ns, meaning a narrow-band laser can impose an acceleration of over $10^4 g$!

Add to this picture a second laser of equal intensity, but propagating to the left (along the $-\hat{i}$ direction). Let's tune the frequency of both lasers a few linewidths $\Gamma = 1/2\pi\tau$ below the atomic resonance peak. Nestled between these two beams, a stationary atom scatters relatively few photons from either laser because they are not resonant. But say the atom has a velocity $+v\hat{i}$ towards the right: the atomic resonance will be Doppler-shifted into resonance with the leftward-propagating laser so that the atom scatters more photons from the leftward ($-\hat{i}$) propagating beam than from the rightward propagating beam. In other words, the atom scatters more photons and therefore receives a larger “kick” from the laser it is moving towards. This Doppler-induced slowing is proportional to the atomic velocity and takes the form of a viscous damping force.

In 1975, Hänsch and Schawlow proposed this as a method to cool atomic gases. By extending the cooling to three dimensions using a total of six laser beams, each one propagating along a cartesian axis, the group of Chu et al. [1985] were able to create the first “optical molasses” in sodium vapor, cooling the atoms to $240 \mu\text{K}$.

1.3.2 Confinement

This scheme is quite successful in making atoms very cold, but has no mechanism to confine them to a particular region in space. Even very cold atoms, jostled about as they scatter photons, execute a random walk and diffuse out of the intersection of the laser beams, leaving the molasses forever. The lifetime of the atoms in the molasses is about 0.1 s [Chu et al., 1985]. In order to perform experiments that show subtle effects, it is desirable to contain the atoms for a much longer time than this. Somehow a spatially-dependent force must be installed to keep the atoms in place within the laser beams' extent.

Many theoretical proposals for spatial confinement using creative arrangements of laser beams were rapidly published, nearly all of which were proven impossible. The difficulty is analogous to the Earnshaw theorem of electrostatics, which states that a charged particle cannot be trapped by an arrangement of static electric fields. This

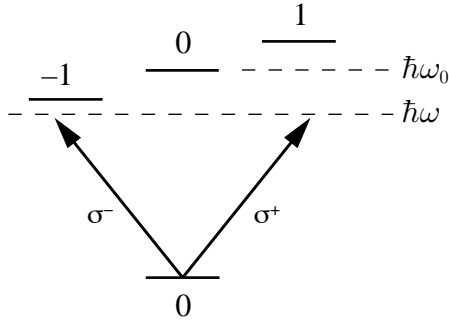


FIGURE 1.1: Diagram showing Zeeman level splitting of a $J = 0 \rightarrow J = 1$ atom in a nonzero magnetic field. Left- and right-circularly polarized laser beams, both at frequency ω , illuminate the atom whose natural resonance is ω_0 . The σ^- polarized beam is shifted into resonance and the σ^+ beam is shifted out of resonance with the atom. The atom therefore scatters more σ^- than σ^+ photons.

is a direct result of $\nabla \cdot \mathbf{E} = 0$ in a source-free region; zero divergence means there is always some “escape route” for the particle.

Ashkin and Gordon in 1983 made a direct analogy to this, now dubbed the “optical Earnshaw theorem,” proving that a particle cannot be trapped by a fixed arrangement of optical fields relying only on the scattering force of light. The scattering force is proportional to the Poynting vector \mathbf{S} of the light, which is divergence-free, and therefore the scattering force too has zero divergence.

The key to overcoming the optical Earnshaw theorem is the realization that atoms do not fall under its stricture because unlike structureless particles, atoms have internal degrees of freedom. Specifically, the force on an atom is $\mathbf{F} = (\sigma/c)\mathbf{S}$, where σ is the cross-section for absorption of light by the atom. This cross-section is not necessarily constant, breaking the direct proportionality between the Poynting vector and the force, allowing us to make $\nabla \cdot \mathbf{F} < 0$, producing a spatially-confining force. For a MOT, that position-dependent force comes from the Zeeman level structure in the atom and is sensitive both to external magnetic fields and to the polarization of the illuminating light.

Returning once again to our one-dimensional scheme with two counterpropagating, red-detuned laser beams, we now add a linearly-varying magnetic field that is zero at the origin: $B \propto bx\hat{i}$. Furthermore, we specify that the two beams have opposite circular polarization. When the atoms are located away from the origin, the Zeeman sublevels of the atom are split by the magnetic field, causing them to preferentially

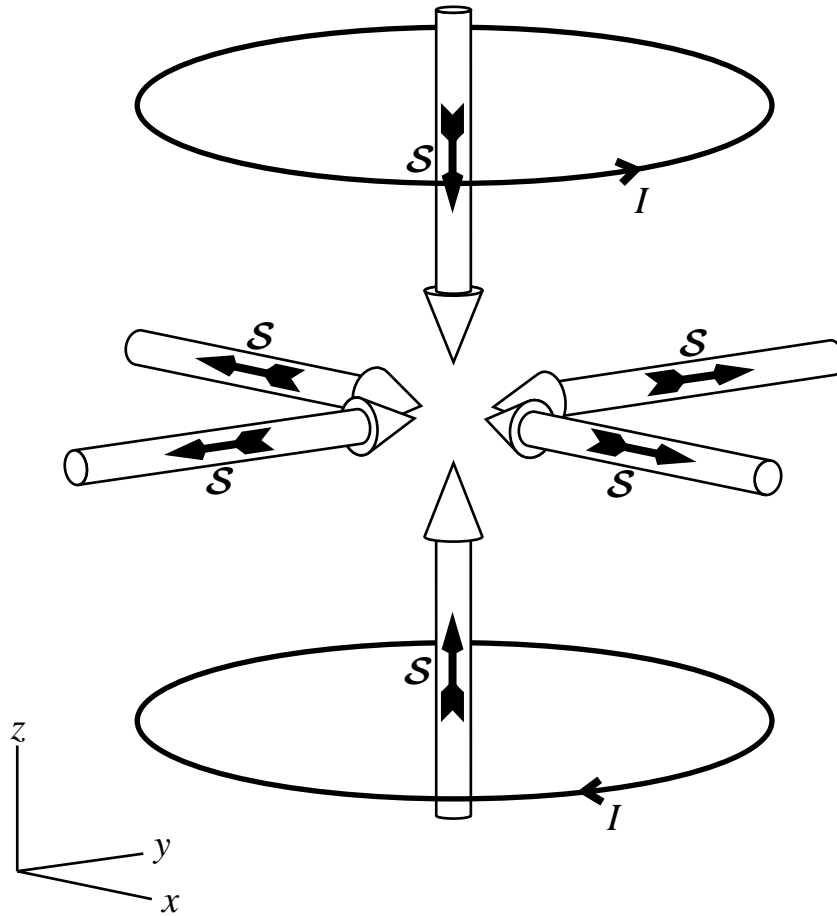


FIGURE 1.2: A three-dimensional magneto-optical trap. The magnetic field coils produce a spherical quadrupole field configuration of the form $\mathbf{B} = (b/2)(-x\hat{i} - y\hat{j} + 2z\hat{k})$ near the origin. The spins \mathcal{S} of the photons from each laser beam are arranged so that the magnetic field will Zeeman shift the atomic energy levels to preferentially scatter photons, pushing the atom toward the origin.

scatter light of one circular polarization over the other. Figure 1.1 illustrates how a two-level atom in a magnetic field, illuminated by red-detuned light ($\hbar\omega$), will scatter more σ^- (in this case) photons than σ^+ photons. By arranging the circular polarization of the light such that its angular momentum opposes the applied magnetic field, the atoms feel a spring-like restoring force that pushes them towards $B = 0$.

In Figure 1.2 we present a schematic three-dimensional MOT. The arrangement of two magnetic field coils with current flowing in opposite directions (commonly referred to as an “anti-Helmholtz” configuration) produces a spherical quadrupole magnetic field. For coils that are large compared to the trap size, the field has the

form $\mathbf{B} = (b/2)(-x\hat{i} - y\hat{j} + 2z\hat{k})$ near the origin, where b is the field gradient measured along the z -direction.

Extending this simple picture from our $J = 0 \rightarrow J = 1$ atom to a real atom is fairly straightforward. The ground state of nearly all isotopes of the alkali atoms (including potassium) are split by the hyperfine interaction with the nucleus, and the excited state has four hyperfine levels (these are illustrated in Figure 2.1 in the next chapter). The details of these complications will be discussed in chapter 2, but the essence is that by adding a second laser frequency we can cause a real atom to act in a manner very similar to our model, and thus form a MOT.

1.4 Summary of achievements

In our first year here, Thad, Dominik, Paul, and I created the first MOT for rubidium-85, in the process building external-cavity grating-stabilized diode lasers and associated drive electronics to stabilize and lock them to a saturated absorption spectrometer. Rapid progress led us to perform the first studies of cold collisions in ^{85}Rb [Hoffmann et al., 1992].

Our interest in the effect of using linearly and elliptically polarized light in a MOT resulted in the vortex-force atom trap [Walker et al., 1992b]. The vortex force allows us to create an inherently [Walker et al., 1992a], not possible in a conventional MOT due to the rapidly varying light polarization across the trap. This spin-polarized trap is useful for studying atomic collisions and for the nuclear beta-decay experiments that are the ultimate aim of this dissertation.

I then began a new line of investigation, heading towards our goal of trapping radioactive potassium. To this end, I narrowed and stabilized an argon-ion pumped ring-cavity $\text{Ti:Al}_2\text{O}_3$ laser to a linewidth of a few megahertz. Using this laser and building another chamber and optical setup, I created the first MOT for potassium, characterizing its operation as a function of many adjustable parameters. Among the characteristic I measured were the loading rate, trap temperature, and ultracold collision rate [Williamson III and Walker, 1995].

I then designed a more complex and flexible XHV (extremely high vacuum, less than 10^{-10} torr) chamber suited for trapping radioactive potassium. In preparation, I studied various configurations for collimating and cooling a feeble effusive beam of natural potassium to efficiently load a MOT, optimizing my apparatus for the three

naturally occurring isotopes of potassium, $^{39-41}\text{K}$. I also developed an ultra-sensitive detection scheme, using an additional diode laser to excite the trapped atoms to produce ultraviolet photons.

I then collaborated with Paul Quin and Paul Voytas to develop a target system capable of producing a radioactive thermal beam of potassium ^{37}K and ^{38}K . However, the short radioactive lifetime of ^{37}K ($\tau_{1/2} = 1.2\text{ s}$) made it difficult to produce a large enough yield for trapping, and the long lifetime of ^{38}K ($\tau_{1/2} = 458\text{ s}$) and high target vacuum system pressure made trapping reasonable amounts of this isotope directly from the effusive target unlikely also.

Inspired by the work of colleagues [Lu et al., 1996; Lee et al., 1996], we designed and built a pyramidal atomic funnel for potassium, capable of operating at poor UHV pressure (10^{-6} torr), that cools and collects room-temperature potassium atoms, then sends them through a low-conductance hole to a low-pressure XHV MOT [Williamson III et al., 1997]. We have successfully integrated the target, funnel, and main MOT to trap stable potassium isotopes, but have been unable to trap radioactive potassium. Data from our stable potassium trap has been used to investigate some possible reasons for our unsuccessful attempts to trap ^{38}K .

Chapter 2

Trapping of natural potassium

2.1 Introduction

In this chapter I discuss the properties of a vapor-cell MOT for potassium. I begin by presenting some background material, illustrating how natural potassium differs from the other alkalis because of its small hyperfine structure (§2.2). Section 2.3 discusses some of the basic statistical mechanics of a vapor-cell MOT and introduces a very simple model of the loading rate. In section 2.4, I derive a simple Einstein rate-equation model for the trap, used to model the operation of the trap and analyze our fluorescence data. Then in sections 2.5 and 2.6 I describe some details of our apparatus and present the measurements I obtained using it, including the loading rate as function of various trap parameters, and the trap temperature. Finally, I conclude by mentioning the work of other researchers that followed our discoveries (§2.7).

2.2 Background

To date a variety of atoms have been stably cooled and confined using magneto-optical traps (MOTs). Since the original demonstration using sodium [Raab et al., 1987], MOTs have been constructed for the alkalis lithium [Lin et al., 1991], rubidium [Walker et al., 1992b], and cesium [Sesko et al., 1989], the alkaline earth atoms magnesium [Sengstock et al., 1993], calcium [Kurosu and Shimizu, 1990], and strontium [Kurosu and Shimizu, 1990], and the metastable states of the rare gases helium [Bardou et al., 1992], neon

[Shimizu et al., 1989], argon [Katori and Shimizu, 1990], krypton [Katori and Shimizu, 1990], and xenon [Walhout et al., 1993]. All these atoms have relatively simple energy-level structures, so that trapping can be accomplished using a small number of laser frequencies. In addition, the wavelengths for the trapping transitions are all in the near ultraviolet to near infrared, where tunable continuous-wave lasers exist with power of at least a few milliwatts.

Notably absent from the above list is the alkali atom potassium, which has a convenient resonance line at 767 nm. Potassium is unique among the alkalis in that the nuclear magnetic moments of its isotopes are comparatively quite small, leading to correspondingly small hyperfine splittings of the optical transitions. As we explain below, this necessitates a different approach to making a MOT for potassium. Although lithium also has small excited-state hyperfine splittings, the structure is inverted compared to the other alkalis, so the trapping is still done by tuning near the $S_{1/2}(F=I+1/2) \rightarrow P_{3/2}(F'=I+3/2)$ transition, as is done for sodium, rubidium, and cesium.

The relevant energy levels for the two most abundant isotopes ^{39}K and ^{41}K , are shown in Figure 2.1. Note that even for ^{39}K , which has the larger hyperfine interaction, the splitting between the $P_{3/2}(F'=3)$ and $(F'=2)$ states is only 21 MHz compared to the natural linewidth of 6.2 MHz. If the trapping laser frequency is chosen to be just below the $4S_{1/2}(F=2) \rightarrow 4P_{3/2}(F'=3)$ transition (the analogous transition for other alkali MOTs), the laser will be detuned to the blue of the $F'=1, 2$ levels, accelerating and heating the atoms. Furthermore, there is strong of the atoms into the $4S_{1/2}(F=1)$ state due to the nearby $4P_{3/2}(F'=2)$ state. Power broadening of the transitions contributes to the reduction of the spectral isolation needed for trapping in the usual manner.

To avoid these problems, we trap potassium using light tuned to the low-frequency side of the entire excited-state hyperfine structure, as shown in Figure 2.1. Two laser frequencies are used, differing by the ground-state hyperfine splitting. Both frequencies provide cooling and trapping forces. This arrangement has the advantage over other MOTs in that the poorly resolved excited-state hyperfine structure creates an intrinsically large capture velocity for the trap. This is illustrated in figure 2.2, which shows the calculated light-induced damping force as a function of velocity, calculated using the rate-equation model described in section 2.4. Clearly the intrinsic capture velocity for the trap exceeds 30 m/s.

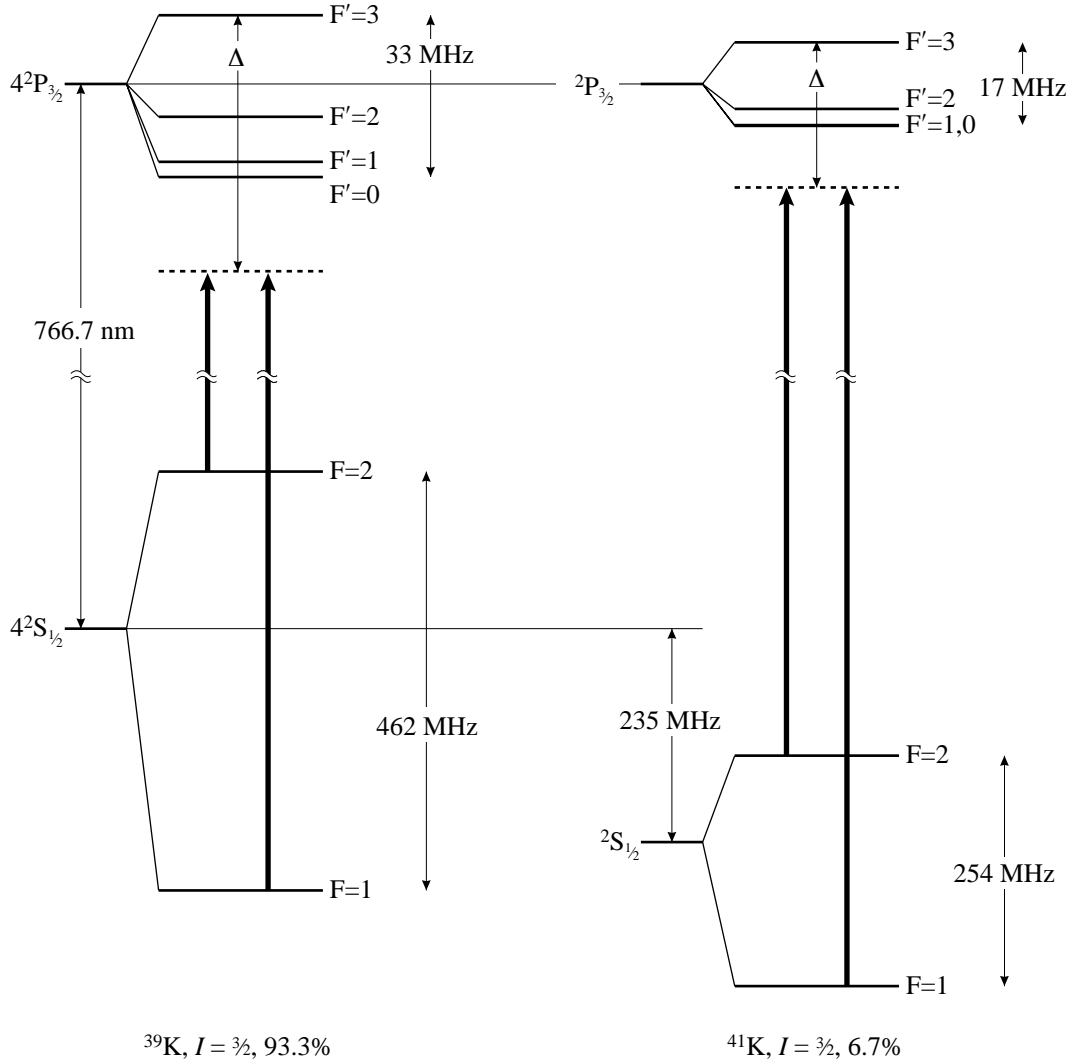


FIGURE 2.1: Hyperfine structure of the $4^2S_{1/2}$ and $4^2P_{3/2}$ states of the two abundant isotopes of potassium. The bold lines indicate the two laser frequencies used for trapping. Note that the detuning Δ is measured from the $4^2S_{1/2}(F=2)$ to $4^2P_{3/2}(F'=3)$ transition. The hyperfine constants for the various states are: ^{39}K , $A(S_{1/2}) = 230.9$ MHz, $A(P_{3/2}) = 6.1$ MHz, $B(P_{3/2}) = 2.8$ MHz; ^{41}K , $A(S_{1/2}) = 127.0$ MHz, $A(P_{3/2}) = 3.4$ MHz, $B(P_{3/2}) = 3.3$ MHz [Arimondo et al., 1977], and the isotope shift is 235.3 MHz [Bendali et al., 1981].

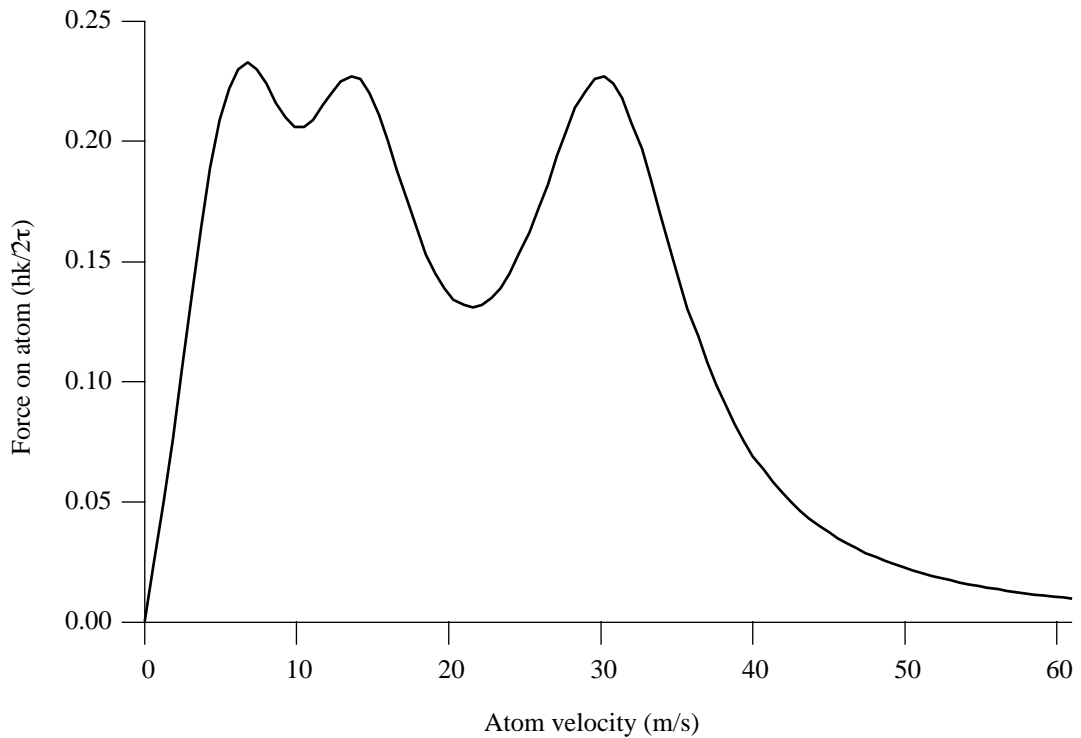


FIGURE 2.2: Plot showing how light exerts force on a moving potassium atom over a wide velocity range, illustrating that the small excited-state hyperfine structure produces a large capture velocity. This is the result of running our model, described in §2.4, for ^{39}K with trap laser intensity $I_{\text{tot}} = 270 \text{ mW/cm}^2$ and detuning $\Delta = -39 \text{ MHz}$.

As an aside, we note that the $P_{1/2}$ states of K have significantly larger hyperfine interactions than the $P_{3/2}$ states, so the levels are well-resolved, suggesting that $P_{1/2}$ states can be used for trapping in a manner analogous to the $P_{3/2}$ “type II” trap originally demonstrated with sodium [Raab et al., 1987]. In fact, Flemming et al. [1997] recently demonstrated a vapor-loaded sodium MOT using the $P_{1/2}$ states. The key to operation of this trap is that the two colors used for trapping need to have opposite polarization, arising from the fact that the both lower levels of the D_1 transition have negative Zeeman shifts. It is quite likely that potassium can be trapped on the D_1 line in the same manner. We will cover some of these considerations in more detail in §6.3 where we discuss the structure of radioactive potassium isotopes.

2.3 Vapor-loading

The easiest means of getting atoms into a trapped state is to load the MOT from a background vapor of alkali atoms. The vapor pressure of most alkalis (including potassium) is controlled either by adjusting the temperature of the cell or by using a valve and reservoir of metal. Happily, the conditions of vacuum required for trapping (a few times 10^{-9} torr) nearly match the room temperature vapor pressure of potassium. Here we outline the basic physics of an alkali vapor and a trap loading from it.

It is interesting to note that measuring the vapor pressure of potassium, as well as many other elements, is a nontrivial task. Even over a limited range of temperature, a look through the literature for vapor pressures of potassium give values that vary by more than a factor of three. Zeng et al. [1985] gives the most accurate and recent values via Faraday rotation measurements (although the empirical functional form comes from Killian [1926])

$$\log_{10} P [\text{torr}] = 8.445 - \frac{4964}{T}, \quad (2.1)$$

most accurate for T from 340 to 380 K.

We determine the vapor pressure in the cell by measuring atomic absorption in the potassium of a frequency-swept, circularly polarized laser beam; this is necessary because we wish to maintain a vapor pressure of potassium that is slightly below the

room temperature equilibrium. Using Beer's law

$$n\sigma l = \log(1 - A), \quad (2.2)$$

where l is the path length, A is the absorbed fraction of light, and σ is the absorption cross section ($2.7 \cdot 10^{-9} \text{ cm}^2$ for potassium and σ^\pm light), we can determine the average vapor pressure of potassium at the trap region in the cell.

A trap operating in such a cell is completely surrounded by this cloud of vapor, but is only able to capture the small fraction of atoms that are moving very slowly, below its "capture velocity" v_c . The capture velocity (v_c) for the trap is a complex function of the laser detuning and intensity, the applied magnetic field gradient, the diameter of the laser beams, and the structure of the atomic levels. Nevertheless, we can make a simple estimate of the capture velocity by assuming a two-level atom illuminated by a laser whose intensity $I_{\text{tot}} \gg I_{\text{sat}}$. Traps typically operate best at a few linewidths Γ below resonance; so, for the sake of argument, say $\Delta = -\Gamma$. This means that the laser will be able to scatter photons from the atoms when they are moving at velocities which keep them within $\pm\Gamma$ of resonance, leading us to

$$v_c \approx 2\lambda\Gamma, \quad (2.3)$$

where λ is the laser wavelength. For potassium, this is roughly 10 m/s.

The speed distribution of a vapor of atoms at temperature T is given by the Maxwell-Boltzmann distribution (Ramsey [1956], for example)

$$f(v) = \frac{4}{\sqrt{\pi}} \frac{v^2}{\alpha^3} e^{-v^2/\alpha^2}, \quad \text{where } \alpha = \sqrt{\frac{2kT}{m}}. \quad (2.4)$$

For room-temperature potassium atoms whose most probable velocity $\alpha = 350 \text{ m/s}$, the fraction of atoms in the thermal speed distribution (equation 2.4) is

$$\eta_v = \int_0^{v_c} f(v) dv = \frac{4}{\sqrt{\pi}} \left[\frac{1}{3} \left(\frac{v_c}{\alpha}\right)^3 - \frac{1}{5} \left(\frac{v_c}{\alpha}\right)^5 + \dots \right] \quad (2.5)$$

For $v_c \ll \alpha$ we can ignore all but the first term, and see that $\eta_{\text{dist}} = 2 \cdot 10^{-5}$. The trap loads from this tiny fraction of atoms that lie in the slow tail of the thermal distribution.

Considering the trapping region to be a sphere of diameter d , and asserting that any atom with $v < v_c$ entering that volume is trapped, the loading rate is [Monroe et al., 1990]

$$\ell_{\text{vap}} = \frac{1}{2} V_{\text{trap}}^{2/3} \frac{v_c^4}{\alpha^3}, \quad (2.6)$$

where V is the trap capture volume and n_{vap} is the atom density in the background vapor, given by the ideal gas law $n [\text{cm}^{-3}] = 9.66 \cdot 10^{18} P[\text{torr}]/T$. We also define a loading rate coefficient $\ell = L/n_{\text{vap}}$, which is dependent only on the parameters of the MOT itself.

2.4 Six-level model

This section describes the rate-equation model we have developed, not only for determining the total excited-state fraction, needed to estimate the number of atoms from our fluorescence detection, but also to calculate the force on the atoms and make predictions about capture efficiency, loading rate, and expected trap performance for radioactive isotopes.

In alkalis with large (many GHz) ground-state hyperfine splittings, like rubidium and cesium, optical pumping is readily overcome with a weak repumping laser, and one can essentially treat the atom as a two-level system, directly calculating the excited-state population via

$$\rho_e = \frac{1}{2} \left(\frac{I_{\text{tot}}/I_s}{1 + I_{\text{tot}}/I_s + 4(\Delta/\Gamma)^2} \right). \quad (2.7)$$

Here Δ is the detuning of the trapping laser from the $S_{1/2}(F=I+1/2) \rightarrow P_{3/2}(F'=I+3/2)$ transition, I_{tot} is the trapping laser intensity incident on the atoms, and I_s is the saturation intensity.

In potassium, however, optical pumping is very strong and it is essential to include the hyperfine structure in such calculations, necessitating the use of a somewhat more complex model. Here we describe a rate-equation model for potassium that has been used extensively in the course of this research that seems to give reasonable results under most of the conditions we have studied.

The six levels consist of two ground states and four excited states, shown in Figure 2.3. The populations of each hyperfine state is allowed to vary, assuming uniform distributions of populations among the Zeeman sublevels of each hyperfine state. In

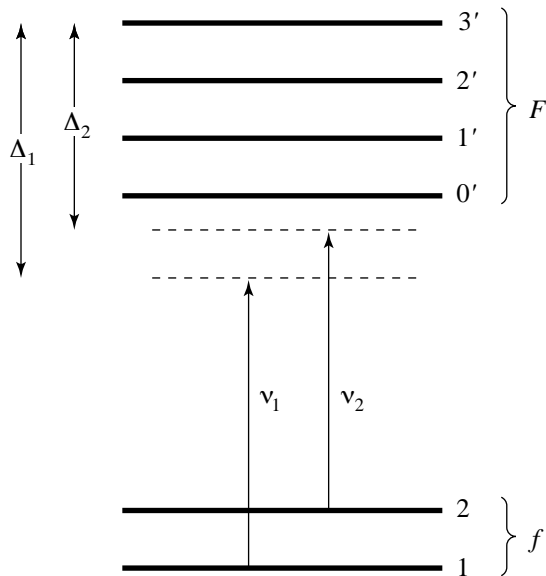


FIGURE 2.3: Definitions of the laser detunings and levels in our model. The numeric labels here correspond to $I = 3/2$, but the model works for any other value of I .

addition, we ignore optical coherences and simply make a rate-equation model for the populations in the various states. Therefore the stimulated emission and absorption rates are calculated using sublevel-averaged oscillator strengths and the population in each hyperfine state is calculated by simply equalizing the excitation and emission rates. Except for the unique characteristics of potassium discussed below, our model is similar to both the model of Lindquist et al. [1992], who also used a rate-equation model to predict loading characteristics of a cesium vapor-loaded MOT, and to the model of Gibble et al. [1992].

The atom is illuminated by two laser frequencies ν_1 and ν_2 , with intensity I_1 and I_2 corresponding to each frequency. In addition, we refer to the detuning Δ , which we define as the amount that either laser frequency is tuned away from the $2 \rightarrow 3'$ transition frequency $\nu_{23'}$. The detuning is typically negative; thus we write $\nu_2 = \nu_{23'} + \Delta_2$. In Figure 2.3, we label the detunings for each frequency individually, Δ_1 and Δ_2 .

As discussed above, all of the odd- A potassium isotopes we consider here ($^{37,39,41}\text{K}$) have $I = 3/2$, giving very small excited-state hyperfine structure, and are trapped with both lasers tuned to the same “virtual level.” Thus $\Delta = \Delta_1 = \Delta_2$ and the difference in the two laser frequencies ν_1 and ν_2 is exactly the ground-state hyperfine

splitting ($\nu_1 - \nu_2 = \nu_{12}$). As the laser frequency is tuned (and Δ changes), both laser frequencies are swept together with the ground-state hyperfine frequency fixed between them. However, to trap the even- A isotopes, with their large nuclear spin, it is necessary to detune the lasers near different levels, and thus $\nu_1 \neq \nu_2$, similar to trapping in sodium or rubidium.*

2.4.1 Populations

The rate equation for the populations of each of the upper-state levels is

$$\dot{p}_F = R_{F1}(p_1 - p_F) + R_{F2}(p_2 - p_F) - \Gamma p_F, \quad (2.8)$$

where p_1 and p_2 are the two lower-state level populations (denoted generally by p_f), R_{Ff} is the excitation rate between levels F and f , and $\tau = 1/2\pi\Gamma$ is the lifetime of the $P_{3/2}$ level. Note that for our potassium trapping paper [Williamson III and Walker, 1995] and most work through 1996 we used $\tau = 25.8$ ns from Wiese and Martin [1980], the best-known value at the time. Recent measurements by Wang et al. [1997] using photoassociative spectroscopy methods have resulted in much higher-precision measurements of the ^{39}K $4p$ state lifetimes. For $P_{3/2}$, they find $\tau = 26.34 \pm .05$ ns, and for $P_{1/2}$, $\tau = 26.69 \pm .05$ ns.

The lower-state populations are given by

$$\dot{p}_f = \sum_F [R_{Ff}(p_F - p_f) + \Gamma_{Ff}p_F], \quad (2.9)$$

where $\Gamma_{Ff} = b_{Ff}\Gamma$ and b_{Ff} is the branching ratio from F to f . Note that uppercase F indicates an upper-state level and lowercase f indicates a lower-state level.

The excitation rates R_{Ff} between upper state F to lower state f are given by

$$R_{Ff} = \frac{c_{Ff}\Gamma_{Ff}}{2} \left(\frac{I_f/I_s}{1 + 4 \left(\frac{\nu_f - \nu_{Ff}}{\Gamma} \right)^2} \right). \quad (2.10)$$

*The computer program used to perform these calculations requests that one specifies the detuning Δ_2 and a ‘‘hyperfine frequency’’ δ_{hyp} , which together determine ν_1 and ν_2 . You can also specify either that the frequency difference between the two lasers remains fixed and $\nu_1 = \nu_{23'} + \delta_{\text{hyp}}$, or that laser ν_1 remains fixed and $\nu_1 = \nu_2 + \delta_{\text{hyp}} = \nu_{23'} + \delta_{\text{hyp}} + \Delta$. Furthermore, the program requests the total power $I_{\text{tot}} = I_1 + I_2$ and a ‘‘color ratio,’’ or $f_{\text{color}} = I_1/(I_1 + I_2)$.

Here I_f and ν_f are the laser intensity and frequency of laser f . The coefficients c_{Ff} are the oscillator strengths, averaged over individual Zeeman levels and over polarizations, and ν_{Ff} are the transition frequencies of the atom between upper state F to lower state f . For potassium, we use a saturation intensity $I_s = 3.6 \text{ mW/cm}^2$, using the same definition as Lindquist et al. [1992].

In steady state, $\dot{p}_F = \dot{p}_f = 0$, so for any excited state level we get

$$p_F = \frac{R_{F1}p_1 + R_{F2}p_2}{R_{F1} + R_{F2} + \Gamma} \quad (2.11)$$

and

$$p_f = \frac{\sum_F (R_{Ff} + \Gamma_{Ff})p_F}{\sum_F R_{Ff}}; \quad (2.12)$$

note that explicitly numbered subscripts always refer to ground state levels.

We can then combine equations 2.11 and 2.12 to get p_2 in terms of p_1 :

$$p_2 = \frac{\sum_F \frac{R_{F2} + \Gamma_{F2}}{R_{F1} + R_{F2} + \Gamma} R_{F1}}{\sum_F \frac{R_{F1} + \Gamma_{F1}}{R_{F1} + R_{F2} + \Gamma} R_{F2}} p_1. \quad (2.13)$$

By assigning an arbitrary value $p_1 = 1$, we calculate p_2 explicitly, then calculate all four p_F using equation 2.11 again. We can then sum the results of this procedure for all six levels to give a normalization factor

$$\sum_f p_f + \sum_F p_F, \quad (2.14)$$

which we divide into all the p_f and p_F to get properly normalized populations. Now we can get the total excited-state population fraction by simply summing the normalized p_F :

$$\rho_e = \sum_F p_F. \quad (2.15)$$

2.4.2 Forces

With the excited-state fraction secured, we can now calculate the force on an atom moving in the trap by allowing for Doppler shifts of the resonance frequencies. Since

the trapping lasers come from six directions, there is a different Doppler shift for each direction, but for simplicity we have constrained the atoms to have velocity along only one direction so that only two of the beams have Doppler shifts. We explicitly put in the Doppler shifts due to the atom's motion, but this will change the normalization of the populations. The excitation rates from four of the beams will be calculated as in equation 2.10, however, the two that are Doppler shifted become

$$R_{Ff}^{\pm} = \frac{c_{Ff}\Gamma}{12} \left(\frac{I_f/I_s}{1 + 4[(\nu_f \pm kv - \nu_{Ff})/\Gamma]^2} \right), \quad (2.16)$$

where kv is the Doppler shift due to the velocity v of the moving atom ($\lambda = 1/k$ is the transition wavelength, 766.7 nm for D_2 in potassium).

The total excitation rate is then

$$R'_{Ff} = \frac{2}{3}R_{Ff} + R_{Ff}^+ + R_{Ff}^- \quad (2.17)$$

and the normalization procedure is very similar to that described in §2.4.1.

We can calculate the spontaneous force on the atom due to the counterpropagating beams from the difference in rates

$$F = \sum_f \sum_F (R_{Ff}^+ - R_{Ff}^-)(p_f - p_F). \quad (2.18)$$

A number of assumptions are inherent in this approach, in particular that we can ignore velocity-dependent dipole forces that may be quite large at high intensity. Furthermore we have similarly not included magnetic field effects in our model since we found little effect of the magnetic field on the loading rates.

2.4.3 Loading rates

We can now use the force calculated in equation 2.18 to find the distance z_{stop} needed to stop an atom of a particular velocity v_c . By asserting that the atom must stop within a volume defined by the diameter of the laser beams, we can treat this velocity v_c as the capture velocity and therefore predict loading rates using equation 2.6.

Beginning with Newton's second law and a derivative trick

$$F = ma = m \frac{dv}{dt} = mv \frac{dv}{dz}, \quad (2.19)$$

and defining the velocity and force in terms of unitless variables u and f

$$F = \hbar k \Gamma f(u) \quad \text{and} \quad u = \frac{kv}{\Gamma}, \quad (2.20)$$

equation 2.19 above becomes

$$mu \frac{du}{dz} = \frac{\hbar k^3}{\Gamma} f(u), \quad (2.21)$$

which we can rearrange and integrate to find

$$z_{\text{stop}} = \int_0^{v_c} \frac{u du}{f(u)}. \quad (2.22)$$

Using equation 2.18 for $f(u)$ and integrating numerically (by Simpson's rule) we now have the stopping distance $z_{\text{stop}}(v_c)$ as a function of velocity for any set of trap parameters (choice of atom, detuning Δ , intensity I_{tot} , and color ratio).

For low intensity trapping beams, the stopping distance can be interpreted as the diameter of the laser beams, but at high intensities, a gaussian beam still exerts considerable force beyond its waist $w=d/2$, defined as the point where the beam intensity drops by $1/e^2$. For high intensity beams, as were used in most of the work in this chapter, we use an effective waist that occurs further outside the beam profile, determined from where the excited-state fraction corresponding to that intensity is reduced by $1/e^2$ of the excited-state fraction at the peak of the beam. Symbolically,

$$w_{\text{eff}} = \frac{w}{\sqrt{2}} \sqrt{\log \frac{I_{\text{tot}}}{I(\rho_{e0}/e^2)}}, \quad (2.23)$$

where $\rho_{e0} = \rho(I_{\text{tot}})$ is the excited state fraction at the center of the beam, and $I(\rho)$ is the intensity required to produce an excited-state population ρ . Using this effective waist as the stopping distance and the equations of Monroe et al. [1990], we can make a good estimate of the loading rate coefficient. We will illustrate the effectiveness of this model later in section 2.6, Results.

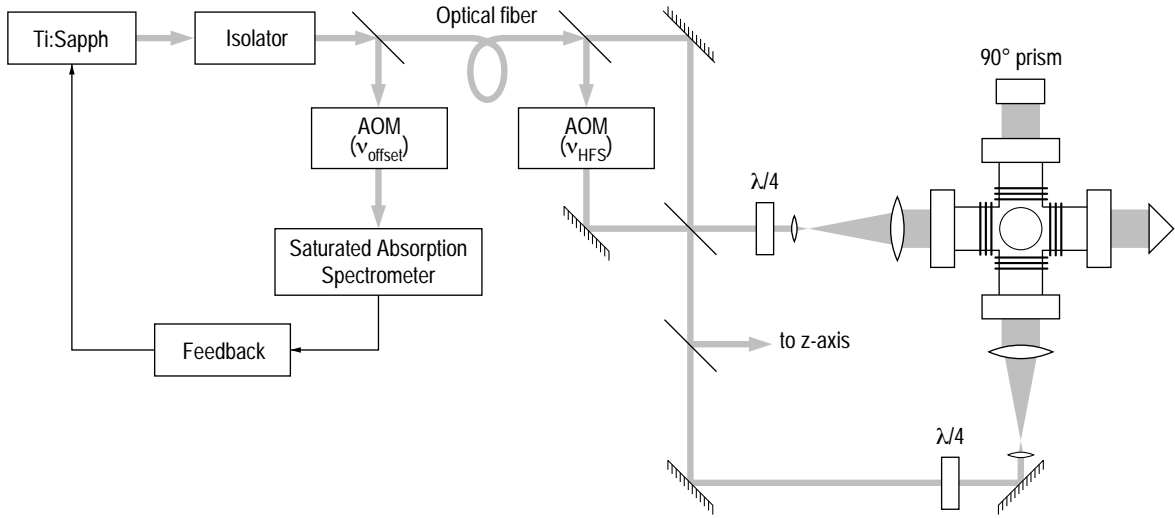


FIGURE 2.4: Apparatus used for vapor-loaded potassium MOT.

2.5 Apparatus

A simplified schematic of our apparatus appears in Figure 2.4. The laser light is provided by a stabilized argon-ion pumped ring Ti:sapphire laser, purged with dry nitrogen to eliminate the destabilizing effects of O_2 , which has a well-known absorption feature near 766.7 nm [Nguyen et al., 1994]. The laser system used throughout the experiments described in this dissertation is described at length in Appendix A.

We always lock the laser to a transition in the most abundant potassium isotope, ^{39}K . In our first potassium trap, we locked the laser directly to the side of a saturated absorption peak. Though simple, this makes adjusting the laser detuning inconvenient, and for less abundant or radioactive isotopes, it is not possible to make an absorption cell filled with the same isotope that is trapped. By adding another acousto-optic modulator (AOM ν_{offset} in Figure 2.4) between the laser and saturated absorption spectrometer, we can tune the laser to any isotope we please and still lock it to the more common ^{39}K . A detailed schematic of the optics used in this locking scheme appears in chapter 6, Figure 6.13.

The laser is thus tuned to the $S_{1/2}(F=2) \rightarrow P_{3/2}$ transition in the desired isotope by offset-locking to the ^{39}K $S_{1/2}(F=2) \rightarrow P_{3/2}$ saturation spectroscopy peak. Because the excited-state hyperfine structure is unresolved, this leads to a 2–3 MHz uncertainty in the detuning Δ .

Part of the light is sent to a second A-O modulator (AOM ν_{HFS} in Figure 2.4),

whose frequency is fixed to the ground-state hyperfine splitting, providing the necessary $S_{1/2}(F=1) \rightarrow P_{3/2}$ light. The output beam from the AOM and the unmodulated beam are adjusted to have equal power, then combined and sent through the trapping chamber. Right-angle prisms, with axes mounted orthogonally to minimize effects of diffraction from their apexes, are used to retroreflect the large beams. With this precaution, the use of prisms rather than waveplates and mirrors does not significantly degrade the operation of the trap (using prisms for all three axes, the number of atoms is reduced by only about 20%). This simplifies the apparatus by eliminating the need for a large mirror and waveplate for each beam.

The trapping chamber is a stainless-steel, ion-pumped vacuum system, containing a room-temperature potassium vapor at a pressure of 3×10^{-9} torr (potassium density $1 \times 10^8 \text{ cm}^{-3}$). Magnetic field gradient and shim coils are wrapped directly around the outside of the chamber. Shim coils are necessary to counteract the intensity imbalance induced by the uncoated windows of the chamber and by the retroreflecting prisms. A photodetector measures the fluorescence of the atoms as they are loaded from the vapor, and a video camera is used to determine the size of the trapped atom cloud. From these measurements we also deduce the density.

2.6 Results

Here we present our measurements of the trap loading rate as a function of many trapping parameters and our measurements of the trap temperature. In chapter 3 we discuss in detail our observations of ultracold collisions in potassium.

2.6.1 Method

Most of the measurements we do involve collecting the photons from the trapped atoms. This entails collection optics, usually a single positive lens, a silicon photodiode, and a current-to-voltage converter, which is of our design. The photodiode current is related to the number of trapped atoms by

$$N_{\text{atoms}} = \frac{V\tau}{g_{\text{I-V}}g_{\text{PD}}\eta_{\Omega}\eta_{\text{opt}}E_{\gamma}\rho_e}, \quad (2.24)$$

where

τ is the excited-state lifetime of the atom,
 E_γ is the photon energy ($2.6 \cdot 10^{-19}$ J),
 ρ_e is the excited-state fraction (see §2.4.1),
 V is the measured output voltage of the converter,
 g_{I-V} is the current-to-voltage converter gain (typically 10^7 – 10^9 V/A),
 g_{PD} is the photodiode conversion efficiency (0.47 A/W for the Hamamatsu S2387 silicon detector), and
 η_{opt} is the optical efficiency, taking into account reflective losses and filters.

Finally, η_Ω is the solid angle collection fraction, given by

$$\eta_\Omega = \frac{1}{16} \left(\frac{d}{s} \right)^2, \quad (2.25)$$

valid when $d \ll s$, where d is the limiting aperture diameter and s is the object-aperture distance.

The number of atoms in the trap is given by a balance of the loading rate and losses of atoms from the trap

$$\frac{dN(t)}{dt} = L - \Gamma N. \quad (2.26)$$

Here $N(t)$ is the total number of trapped atoms as a function of time t and Γ is the total loss rate of atoms from the trap. We will detail trap loss mechanisms in chapter 3.

In the following sections, we will focus on trap loading rates as a function of various trapping parameters, deduced by measuring the number of atoms as a function of time as the atoms load into an empty trap.

2.6.2 Loading measurements

We have characterized the operation of both the ^{39}K and ^{41}K traps as a function of the detuning Δ , beam diameter d , and intensity I_{tot} . Here, I_{tot} refers to the sum of the laser intensities from each of the six beams and both laser frequencies. In figure 2.5 we show how the number of atoms, loading rate coefficient, density, and loss rate depend on Δ . The ^{39}K data, represented by solid symbols, were taken at $I_{tot} = 220 \text{ mW/cm}^2$ and $d = 1.2 \text{ cm}$; the ^{41}K data, represented by open symbols, were taken at $I_{tot} = 470 \text{ mW/cm}^2$ and $d = 0.6 \text{ cm}$. Both data sets were taken with

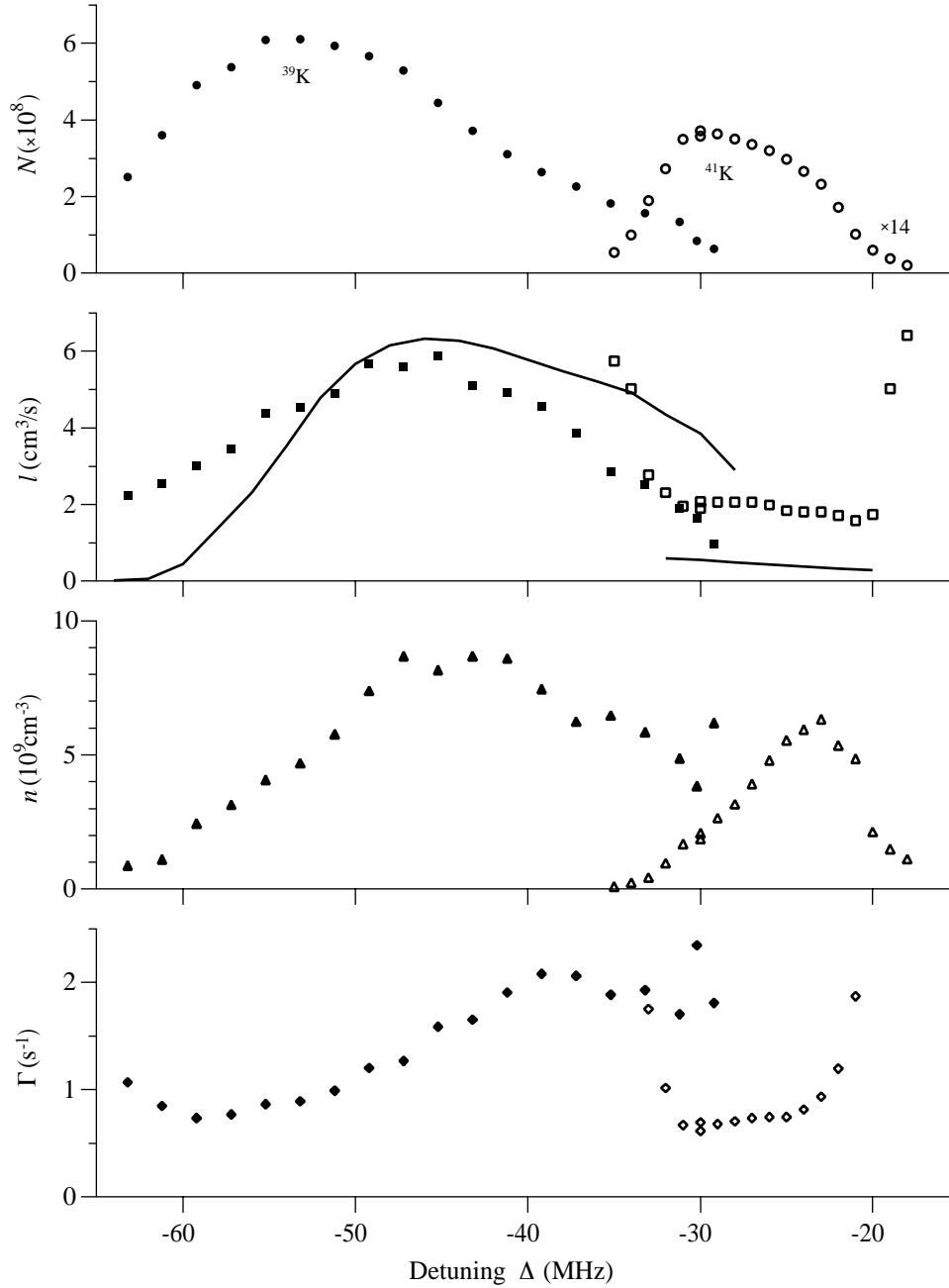


FIGURE 2.5: (a) number of trapped atoms N , (b) loading rate coefficient ℓ , (c) trapped atom density n , and (d) loss rate Γ , all as functions of the trap laser detuning Δ . Filled symbols represent ^{39}K , while open symbols represent ^{41}K . The ^{39}K data was taken with $I_{\text{tot}} = 220 \text{ mW}/\text{cm}^2$, $d = 1.2 \text{ cm}$, and the ^{41}K data was taken with $I_{\text{tot}} = 470 \text{ mW}/\text{cm}^2$, $d = 0.6 \text{ cm}$. The ^{41}K data in (a) has been scaled by 13.9, the isotopic abundance ratio. The solid lines in (b) are the results of our simple loading-rate model, scaled by multiplying by a factor of 1.5. Operation of the trap was marginal at very large and very small detunings, giving large uncertainties in Γ .

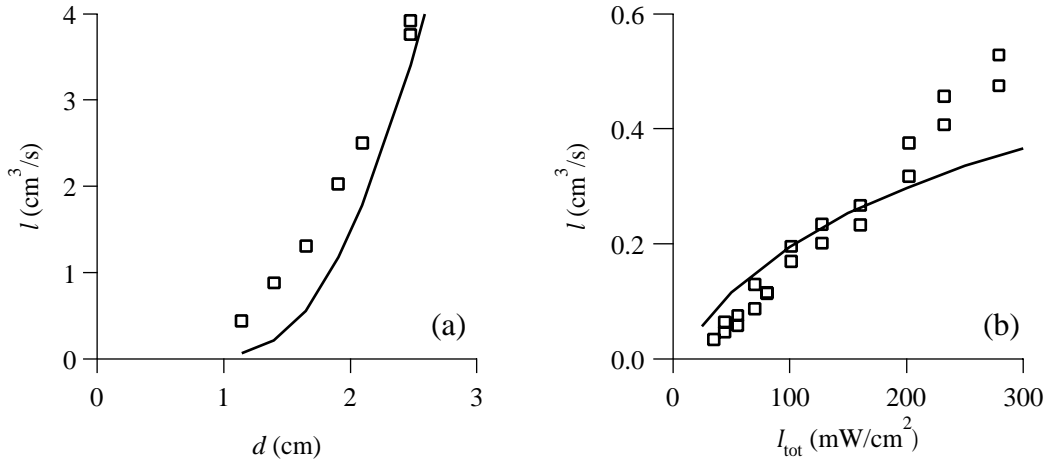


FIGURE 2.6: Loading rate coefficient ℓ as a function of (a) beam diameter d and of (b) intensity I_{tot} , for a magnetic-field gradient of 16 G/cm, using ^{41}K . In (a) $I_{\text{tot}} = 20 \text{ mW}/\text{cm}^2$ and $\Delta = -32 \text{ MHz}$; (b) $d = 0.6 \text{ cm}$ and $\Delta = -21 \text{ MHz}$. The simple loading-rate model results shown in both cases (solid lines) have been scaled by multiplying by a factor of 1.5.

a magnetic field gradient of 16 G/cm, while the bias field was adjusted slightly (less than a gauss) each time Δ was changed to keep the trap centered in the beams. The magnetic field gradient could be changed on the order of 50% up or down without materially affecting trap operation.

Although the ^{39}K and ^{41}K data were taken under rather different trapping conditions, we can still compare them qualitatively. When we scale the number of atoms by the isotopic ratio, we get similar results for both. The differences in the loading rate coefficients and in density are likely due to the fact that the ^{41}K trap used smaller, more intense beams. The difference in the loss rates between the two isotopes will be discussed in the next chapter.

We have also measured ℓ as a function of d and I_{tot} , shown in figure 2.6. The model results, which have been scaled by a multiplicative factor of 1.5 to give a good fit to Figure 2.6a, follow the data rather well as d is changed (2.6a), but diverge at high I_{tot} (2.6b). This may be attributable to the neglect of dipole forces; nevertheless, the simple model is useful and has predictive power in the regime in which traps are normally operated. In addition, we have plotted the model results as a function of Δ in Figure 2.5b, where it has been scaled as before. Over a wide range of parameters, it is clear that the model is good to within a factor of three. We note that the unscaled Lindquist et al. [1992] model for a cesium MOT also predicted smaller numbers of

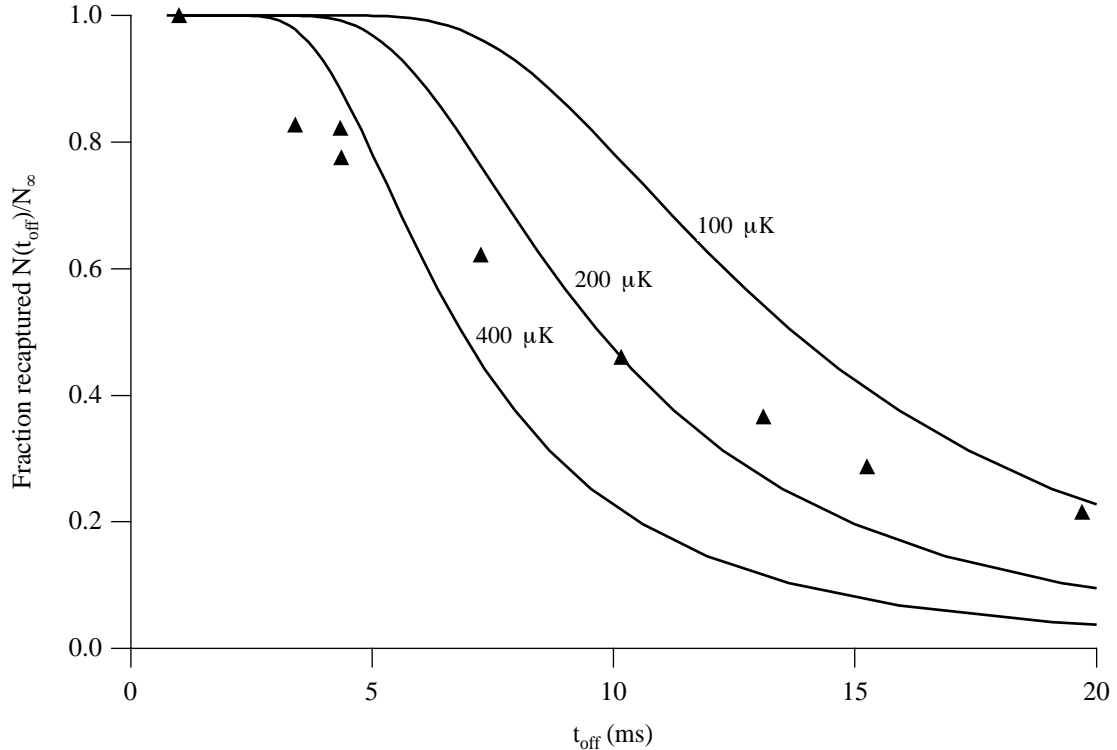


FIGURE 2.7: Trap temperature as determined by release and recapture technique, showing measured data (triangles) and predicted curves for three different trap temperatures.

atoms than were observed. In order to illustrate the ability of the model to predict trends, they scaled their results by a factor of 3.3.

2.6.3 Trap temperature

The trap temperature was estimated using a release and recapture distribution of the atoms into a spatial distribution. After some period of time t_{off} , the trap is turned back on and the remaining atoms are recaptured. By varying t_{off} and measuring the fraction of atoms recaptured, we can roughly determine the trap temperature.

Now we discuss the model we used for this measurement. We begin by assuming that the trapped atoms have a Maxwell-Boltzmann distribution, given in equation 2.4 (except now T is replaced by T_{trap} , the trapped atom temperature). We assume that the initial radius r of the trapped atom ball is negligible compared to the radius R of the recapture volume defined by the laser beam diameter. We also assume that any atoms remaining within the capture radius R are retrapped.

We must now understand how the number of atoms in the recapture sphere changes with time. To do this, we map velocity into space by simply rewriting $f(v)$ as a function of distance r and parametrically as a function of time t , namely

$$f(v) = f(r;t) = \frac{4}{\sqrt{\pi}\alpha^3} \frac{r^2}{t^2} e^{-r^2/\alpha^2 t^2}, \quad v = \frac{r}{t}. \quad (2.27)$$

From this distribution, we can calculate that the number of atoms in a shell of radius R is

$$N(t) = \int_0^R N_\infty f(r;t) dv = \frac{4N_\infty}{\sqrt{\pi}\alpha^3 t^3} \int_0^R r^2 e^{-r^2/\alpha^2 t^2} dr. \quad (2.28)$$

Integrating this by parts, we arrive at

$$N(t_{\text{off}})/N_\infty = \text{erf } \xi - \frac{2}{\sqrt{\pi}} \xi e^{-\xi^2}, \quad \text{where } \xi = \sqrt{\frac{m}{2kT_{\text{trap}}}} \frac{R}{t_{\text{off}}}. \quad (2.29)$$

We plot our data for a ^{41}K MOT with parameters $I_{\text{tot}} = 530 \text{ mW/cm}^2$, $R = 0.3 \text{ cm}$, and detuning $\Delta = -21 \text{ MHz}$, as well as equation 2.29 for three trap temperatures in Figure 2.7. From this we can deduce a trap temperature of approximately $200 \mu\text{K}$. Although this temperature is similar to that found in MOTs for other alkalis, it is below the temperature expected for Doppler cooling of a few millikelvin under our conditions (high intensity and large detuning). As is true for other alkali MOTs, our temperature is likely lower because of the effect of polarization-gradient, or Sisyphus, cooling also present in the trap.

2.7 Conclusion

We have emphasized in this chapter the different issues involved in studying potassium atoms in a MOT. With the exception of the roles of the poorly resolved excited-state hyperfine structure, we find that the trap behaves in most respects quite similarly to the other alkalis.

Since our first potassium MOT, many groups have followed in building potassium MOTs of their own. In Connecticut, the group of Phil Gould and Bill Stwalley are studying potassium via photoassociative spectroscopy [Wang et al., 1996a,b, 1997], in Brazil, Vanderlei Bagnato's group created a double-species trap with potassium and sodium [Santos et al., 1995], and in Canada, Otto Häusser's group at TRIUMF have

created a MOT for radioactive potassium ^{37}K and $^{38}\text{K}^m$ [Behr et al., 1997].

Chapter 3

Ultracold Collisions

3.1 Introduction

To date, a number of studies have been made of excited-state collisions of atoms in magneto-optical traps (see Walker and Feng [1993] for a recent review). These collisions are of interest due to the sensitivity of the collision dynamics to weak, long-range interactions, the similarity of collision and spontaneous emission times, and the capabilities of precision molecular spectroscopy approaching a few cm^{-1} of the dissociation limit. All these features should in principle be present in ultracold collisions of potassium atoms.

In this chapter we describe our measurements of the collision rates for both abundant isotopes of potassium using only the trapping lasers to induce collisions. In the following sections we give a brief summary of how we can observe collisions in a trap (§3.2), followed by a description of our measurement technique (§3.3). Finally, we present our measurements of the collision rate coefficient for both isotopes (§3.4).

3.2 Background

As discussed briefly in section 2.6.1, the number of atoms in the trap, whether it is loaded from a background vapor or from a beam, results from a balance of loading into and loss out of the trap

$$\frac{dN}{dt} = L - \Gamma N, \tag{3.1}$$

where n is the trapped atom density, L is the loading rate in atom/s, and Γ is the total loss rate in s^{-1} .

Our first measurements of β were done in a vapor-loaded potassium cell, as described earlier in §2.3. The loading rate of a trap in an alkali vapor is just $L = \ell n_A$, where ℓ is the generalized loading rate coefficient in cm^3/s , and n_A is the alkali vapor density.

The coefficient Γ contains contributions from two sources:

$$\Gamma = \gamma + \beta \frac{\int n^2 dV}{\int n dV}, \quad N = \int n dV \quad (3.2)$$

The coefficient γ is the rate due to collisions with untrapped potassium atoms and hot background atoms, and β is the ultracold collisional rate coefficient. Note that the ultracold loss rate depends upon the distribution of atoms in the trap; since we work in the radiation-trapping limited regime, [Walker et al., 1990] the trap density is approximately constant and we can consider the density n to be constant, thus

$$\Gamma = \gamma + n\beta \quad (3.3)$$

We refer to Γ as the *total* trap-loss rate, losses due both to hot- and cold-atom collisions. By measuring the total trap-loss rate Γ and independently varying the trap density n we can determine the values for both γ and β .

By measuring the number of atoms in the trap as a function of time and under various conditions, we can isolate each of the parameters above. In our potassium trapping paper [Williamson III and Walker, 1995], we made the first measurements of β in K.

An approximate solution to 3.1, appropriate when $\beta n \ll \gamma$ is

$$N(t) = N_\infty (1 - e^{-\Gamma t}), \quad N_\infty = \frac{L}{\Gamma}; \quad (3.4)$$

where N_∞ is the number of atoms loaded into the trap as $t \rightarrow \infty$, i.e, a fully-loaded trap. Note that this limit is nearly always the case for a vapor-loaded trap; that is, the background vapor pressure is the dominant limit on the maximum number of trapped atoms N_∞ .

3.3 Measurement technique

We can readily measure N , the total number of atoms in the trap by simply collecting the fluorescence from the trapped atoms and calculating the excited-state fraction ρ_e (equation 2.24), but measuring the density is a bit trickier. The trouble is that the trap density n is not constant throughout the trap volume, nor is it directly proportional to the total number N of trapped atoms. As the trap loads from empty, the density profile changes due to radiation trapping; at high trap density, the photons scattered by the atoms do not necessarily escape, but are re-absorbed by adjacent atoms. This produces an effective repulsive potential between the atoms, changing their distribution and ultimately limiting the density of atoms that can be trapped (which is the motivation for a variety of other types of traps which do not suffer this limit, including the far-off resonance trap [Miller et al., 1993] and the dark-SPOT trap [Ketterle et al., 1993; Townsend et al., 1996]).

In our previous collisions experiments in rubidium [Hoffmann et al., 1992], we had the luxury (but complexity) of a second “catalysis” laser, which allowed us to induce collisions between the atoms while keeping the trapping conditions constant. With this technique, we could hold the number N and therefore density distribution $n(r)$ constant while increasing the collision rate by tuning the catalysis laser frequency. However, at that time diode lasers were not readily available below 770 nm and thus we developed a technique for observing cold collisions using only the trap laser.*

In order to separate the cold collision rate coefficient β from the total loss rate Γ , we need an independent means of varying the trap density n (see equation 3.3). We do this by changing the magnetic field gradient dB/dz , which changes the trap spring constant as well as the trapped atom density n . We measure the total loss rate Γ via equation 3.1 by measuring the number of trapped atoms N . By plotting Γ versus n , as in Figure 3.1, we see that the y -intercept gives γ and the slope, β .

We also need to measure the density of the trapped atoms n , which we do by imaging the ball of atoms onto a CCD video camera. The two-dimensional image from the video camera is a column integral of the fluorescence emitted from the three-dimensional distribution of atoms along the direction perpendicular to the image plane. Furthermore, if we assume a spherically symmetric distribution, all the information we need is contained in a single scan-line of the CCD image that passes through the

*Since that time, we have built stabilized, external-cavity diode lasers working at 767 nm.

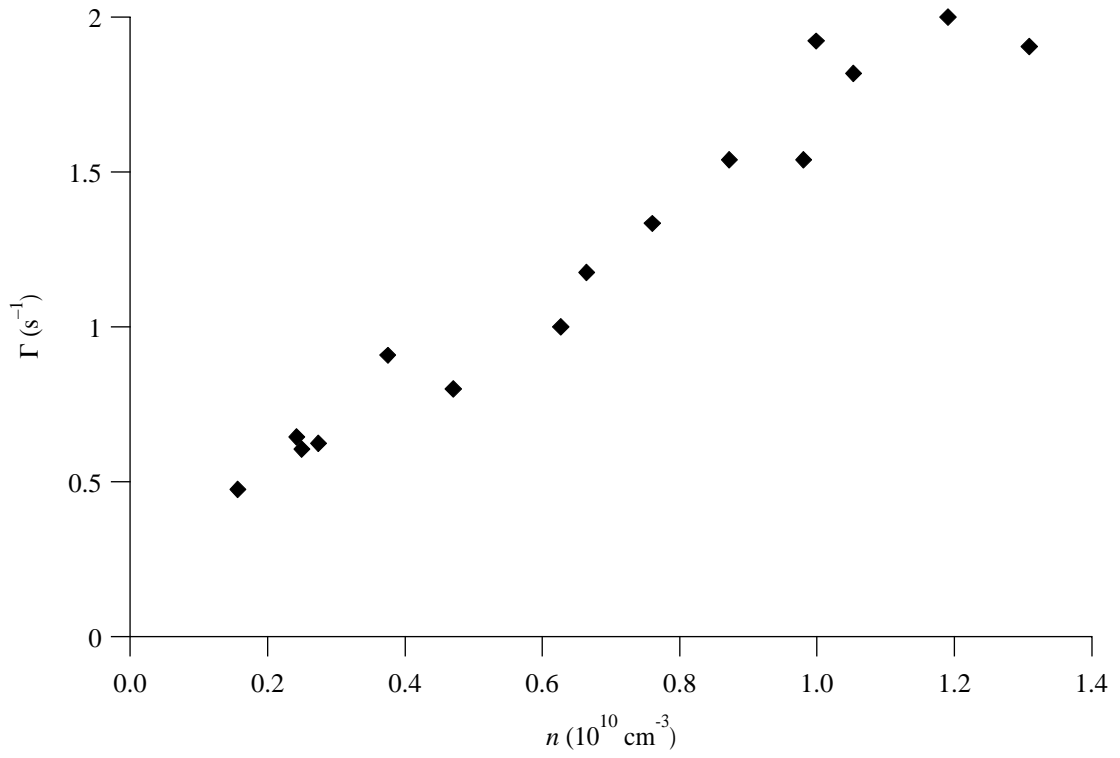


FIGURE 3.1: Dependence of the total collision rate Γ on trap density n for ^{39}K . The detuning $\Delta = -39 \text{ MHz}$ and total trap laser intensity $I_{\text{tot}} = 250 \text{ mW/cm}^2$.

center of the trap, which we “grab” using a digital oscilloscope.

Let’s consider two limiting cases for the spatial density distribution of atoms. First, a “hard sphere” of uniform density n_0 and radius R , with a step-function distribution

$$n(r) = n_0 \begin{cases} 1 & \text{if } r \leq r_0 \\ 0 & \text{if } r > r_0, \end{cases} \quad (3.5)$$

which is what we expect in the extreme radiation-trapping limit. The column integral through the center of this distribution is just the equation for a circle

$$j(x) = 2n_0\sqrt{R^2 - x^2}, \quad (3.6)$$

where x is the distance along the central scan line $j(x)$ that we observe on the oscilloscope. From this we can readily determine the full-width at half-maximum (FWHM), $2a = \sqrt{3}R$. From this we calculate a simple-minded volume $V_{\text{FWHM}} = (4/3)\pi a^3$, and a density $n_s = N/V$. But this volume is smaller than the correct volume $(4/3)\pi R^3$ by a factor $3\sqrt{3}/8$. Thus we determine the correct density from the simple-minded volume

$$n_0 = 0.65 \frac{N}{V_{\text{FWHM}}}. \quad (3.7)$$

Now consider the other limiting case, a gaussian distribution

$$n(r) = n_0 e^{-r^2/\sigma^2}, \quad (3.8)$$

which is most correct for a nearly empty trap, not radiation-trapping limited. (Note that between these two limits, the density is best represented by a Fermi function.) We readily find that the FWHM for a z -integrated cross section of this distribution is just $2a = 2\sqrt{\log 2}\sigma$, and we again measure a simple minded-density N/V_{FWHM} based on this. But the peak density n_0 is given by integrating this distribution

$$N = \int_0^\infty n(r)dV = \pi^{3/2}n_0\sigma^3, \quad (3.9)$$

then substituting the FWHM $2a$, we find

$$n_0 = \frac{4(\log 2)^{3/2}}{3\sqrt{\pi}} \frac{N}{V_{\text{FWHM}}} = 0.43 \frac{N}{V_{\text{FWHM}}} \quad (3.10)$$

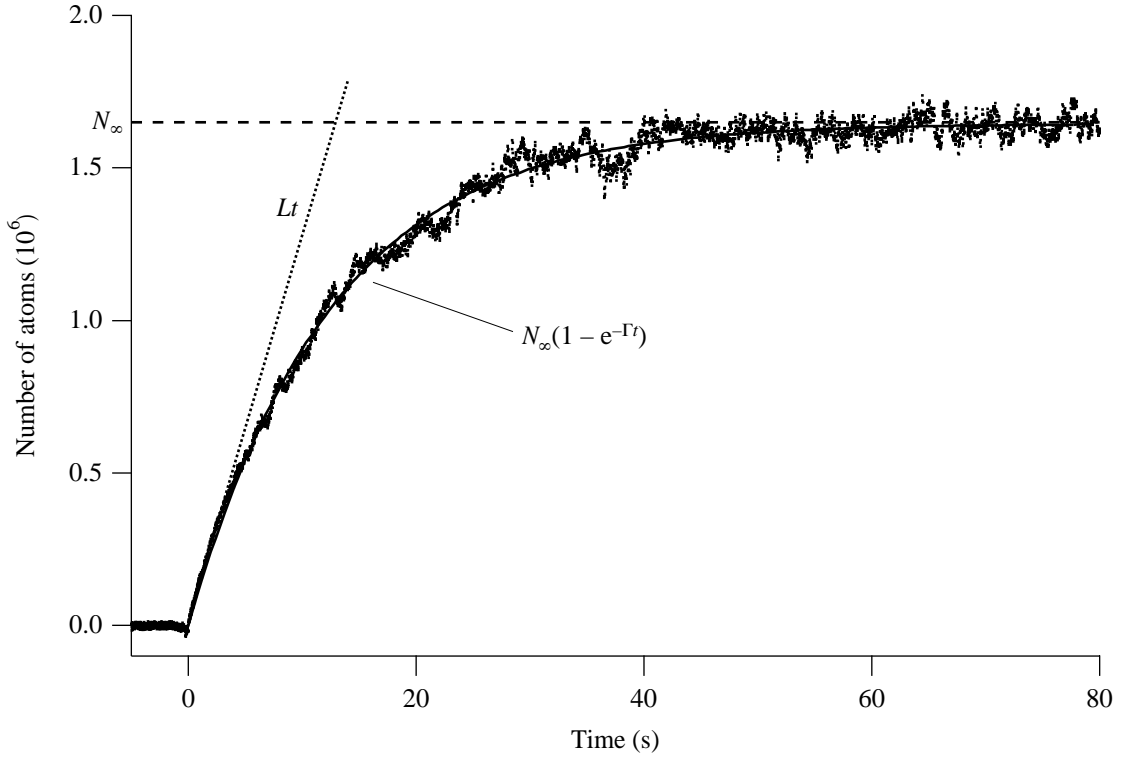


FIGURE 3.2: Example trap loading transient; the solid line is fit to data, dotted line is loss-less loading rate Lt , and dashed line is the equilibrium number of atoms N_∞ .

Of course, our distribution falls somewhere between the above two limits, and for the measurements presented here we split the difference and use $n_0 = 0.5N/V_{\text{FWHM}}$. Although this may seem somewhat arbitrary, there are a variety of other error contributions in determining n_0 , including non-spherical trap shape and errors in determining N .

3.4 Results

As explained above, we determine the loss rate Γ directly by measuring the number of atoms loaded into the trap over time. A sample transient is shown in Figure 3.2, showing a fit to equation 3.4 and solutions in the limit of $t \rightarrow 0$ and $t \rightarrow \infty$. Two processes are known to contribute to these rates. First, collisions with hot background atoms (mostly K atoms in this experiment) can eject the atoms from the trap at a rate γ . This process is weakly dependent on the trap depth, and therefore γ is likely to be insensitive to the detuning of the lasers from resonance. Second, excited-state

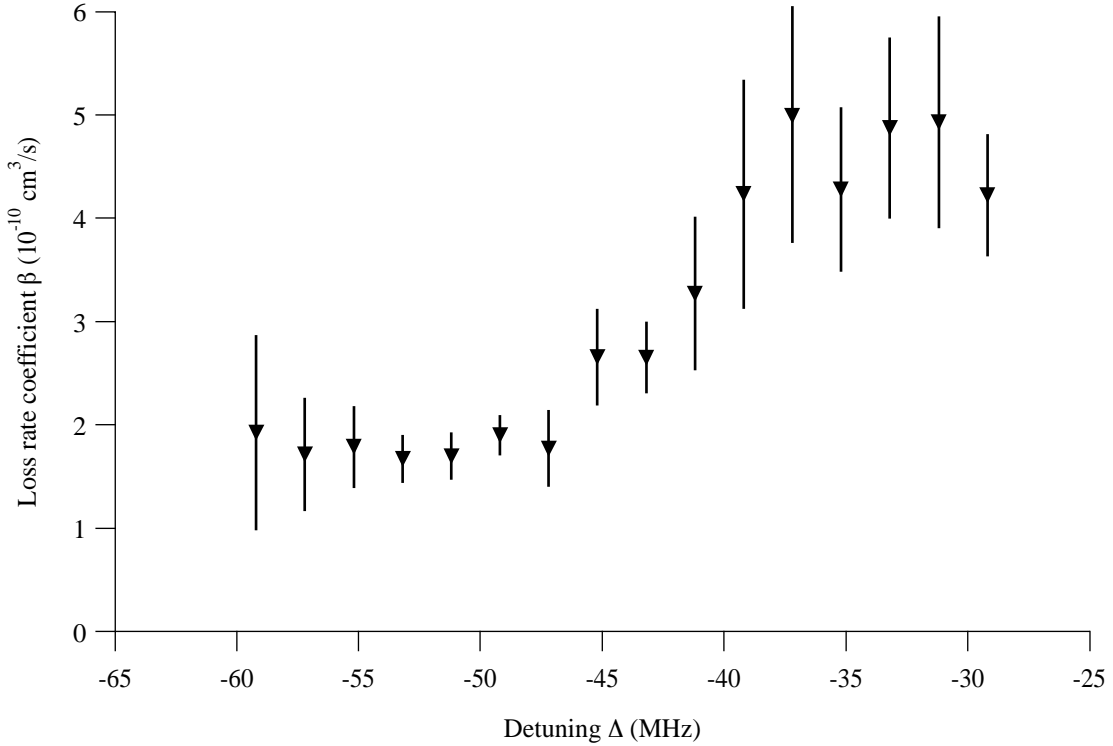


FIGURE 3.3: Dependence of the collisional rate coefficient β as a function of detuning Δ , for ^{39}K at intensity $I_{\text{tot}} = 220 \text{ mW/cm}^2$.

collisions between the trapped atoms can also result in loss of atoms from the trap, with rate βn . The loss rate due to this process should display a strong frequency dependence since the rate depends both on density n as well as the collisional rate coefficient β . The frequency dependence of β arises from a number of effects, the most important being spontaneous emission during the collisions and modification of the dynamics by hyperfine interactions [Walker and Pritchard, 1994]. Figure 2.5d shows the dependence of the loss rate on detuning for ^{39}K . This strongly frequency-dependent rate suggests that ultracold collisions are important in the trap.

To extract the ultracold collision rates from the data we fix Δ and study the dependence of the loss rates on n , which is varied by changing the magnetic field gradient. Typical data are shown in figure 3.1. The slope of the data gives the collisional rate coefficient β . Furthermore, we find that the intercept γ varies only slightly with Δ , consistent with the interpretation that the intercept is due to collisions with untrapped room-temperature K atoms. We find that $\gamma \approx 0.3 \text{ s}^{-1}$.

Figure 3.3 shows the dependence of β on Δ . We find a small variation, roughly a

factor of 2.5 in β over the detuning range studied. This is not too surprising, since the range is quite limited compared to “catalysis” laser experiments where the detuning is varied up to 1 GHz. The absolute rates we measure are comparable to results for the other alkalis [Monroe et al., 1990]. Thus the detuning dependence of the loss-rate shown in Figure 2.5d arises mostly from the variation of n with Δ . The error bars in Figure 3.3 reflect observed fluctuations in measurements of n and Γ , however there may be systematics that change the vertical axis scale.

For ^{41}K the situation is quite different. Even at high intensities, we find only a slight dependence of the loss rates on detuning, except under extreme conditions of detuning and (small) magnetic field gradients, where the operation of the trap is marginal. We find no density-dependent effect at the level of our sensitivity, which gives an upper limit on β for ^{41}K of $\beta < 9 \times 10^{-11} \text{cm}^3/\text{s}$ at $220 \text{mW}/\text{cm}^2$, a factor of 3–5 lower than for ^{39}K . Of course, these results are not directly comparable due to the different hyperfine structures and detunings.

The principal uncertainty in the ultracold collision rates is the determination of the density n . Here the principal issues are the difficulty in determining the precise density distribution owing to the often asymmetrical shapes of the atom clouds and the uncertainty in the excited-state fraction. We estimate an overall uncertainty for the collisional loss rate coefficient β of about a factor of two, based on the reproducibility of the measurements for different cloud shapes and different excited-state fractions.

These ultracold collision measurements provide new insight into the structure of potassium. Our measurement of the cold collision rate for ^{39}K and placement of an upper bound on the rate for ^{41}K show a striking difference between the two isotopes. This is not unexpected, as large isotope effects have been observed in the collisional loss rates for rubidium [Feng et al., 1993], and in the radiative escape rates for lithium [Ritchie, 1994]. These differences can be attributed either to the dynamics of the collision or to different energy-transfer probabilities. In rubidium, the hyperfine structure of the two isotopes is quite different, so the likely culprit is collision dynamics.

However, in potassium, the hyperfine structure of both ^{39}K and ^{41}K is very small and we detune the trapping (and collision-inducing) laser below the entire upper-state manifold: therefore we do not expect the collision dynamics to be different, pointing to a difference in the energy-transfer mechanisms. The two effects that contribute to energy-transfer are fine-structure changing collisions and radiative redistribution. Radiative redistribution is unlikely to be affected by isotopic differences, but Dulieu

et al. [1994] has observed that fine-structure changing collisions are sensitive to small mass differences. We therefore suspect that the different cold collision rates we observe between the ^{39}K and ^{41}K are due to the sensitivity of fine-structure changing collision dynamics to isotopic differences.

Chapter 4

Beam-loaded MOT

4.1 Introduction

Here we address the concerns that arise in loading a trap from an atomic beam source rather than from a background alkali vapor. The experiment described here sets the stage for loading a MOT with radioactive atoms created on-line, created by bombarding a target with high-energy particles. Such a source of atoms has the characteristics of an effusive beam, and in fitting with our eventual goal of making a radioactive trap, we present our efforts to efficiently collect atoms from a feeble, beam-like source.

We start this chapter by introducing the characteristics of a beam source, both spatially and kinematically, in section 4.2. Next we survey a few of the many techniques people have devised to create a collimated beam (§4.3), then motivate our simple but efficient direct-loading method. In section 4.4 we detail our apparatus and some important considerations relevant to its design. We present our measurements and use them to derive a trap capture velocity (§4.5), and determine the vacuum-limited trap lifetime.

4.2 Atomic beams

4.2.1 Angular distribution

The simplest atomic beam is an effusive source emanating from a thin-walled orifice. The spatial distribution of the atoms from a circular orifice of radius r with a density

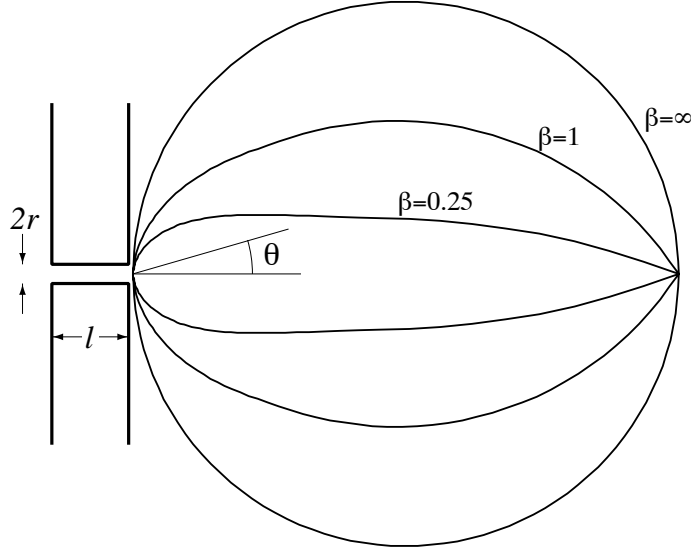


FIGURE 4.1: Cylindrical channel geometry and plot of normalized angular flux distribution $q(\theta)$ for $\beta = 0.25, 1, \infty$.

of atoms n_{vap} behind it is well-known [Ramsey, 1956] to be

$$\frac{dq}{d\Omega} = q_0 \cos \theta, \quad q_0 = \frac{\sqrt{\pi}}{2} n_{\text{vap}} \alpha r^2, \quad (4.1)$$

where θ is the angle normal to the orifice plane (see Figure 4.1), q_0 is the total flux emerging from the hole, and α is the most probable thermal velocity in the vapor behind the hole, given in equation 2.4. However for our geometry, because we desire a somewhat feeble beam and thus r must be very small, we do not satisfy the requirement that the thickness of the channel $l \ll 2r$. We must use a somewhat more complicated formulation to account for this [Scoles, 1988].

The geometry of this situation is displayed in Figure 4.1, and the parameter $\beta = 2r/l$, so that as $\beta \rightarrow \infty$ we approach a thin-walled orifice. The total flux $q = wq_0$ through such a channel is reduced by a factor w below the flux q_0 from a thin orifice. The factor w is given by Scoles [1988] as

$$w = 1 + \frac{2}{3}(1 - 2\alpha)(\beta - \sqrt{1 + \beta^2}) + \frac{2}{3}(1 + \alpha)(1 - \sqrt{1 + \beta^2})\beta^{-2}, \quad (4.2)$$

where

$$\alpha = \frac{1}{2} - \frac{1}{3\beta^2} \left[\frac{1 - 2\beta^3 + (2\beta^2 - 1)\sqrt{1 + \beta^2}}{\sqrt{1 + \beta^2} - \beta^2 \sinh^{-1}(1/\beta)} \right]. \quad (4.3)$$

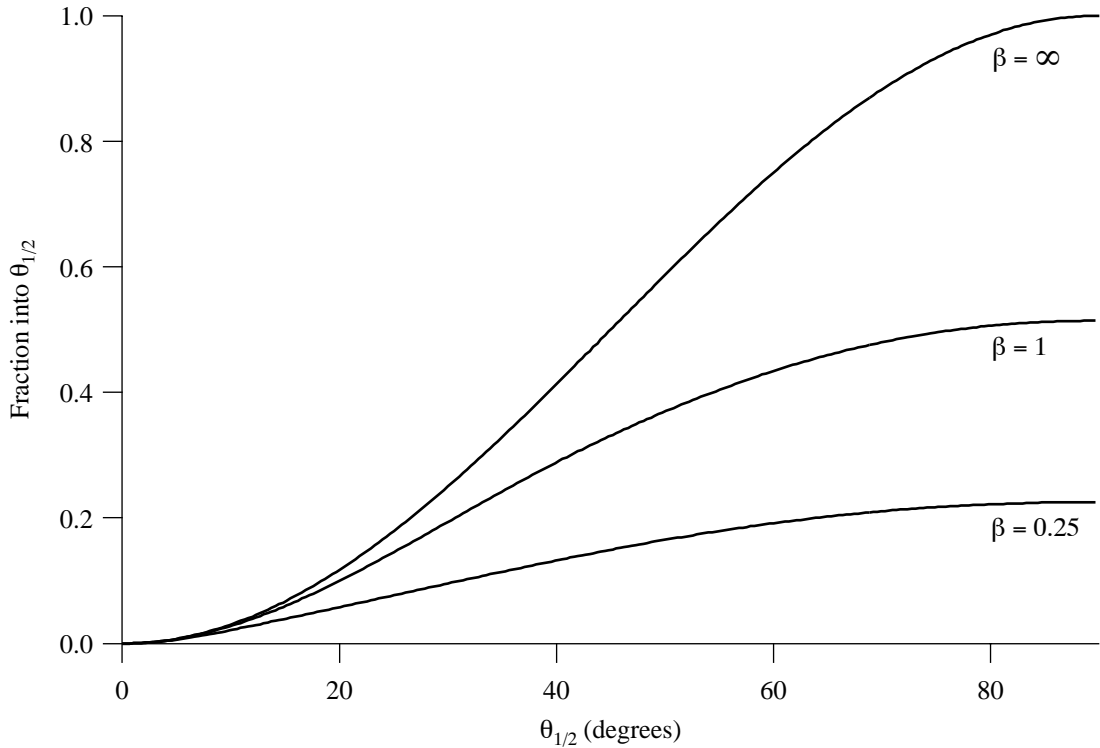


FIGURE 4.2: Fraction of total beam flux emitted through a cylindrical channel into a cone of $\theta_{1/2}$. Shown is η_{Ω} calculated for channel dimensions of $\beta = 0.25$, 1, and ∞ ; note that the as the channel grows in length, the total flux emitted drops.

The angular distribution is of course somewhat narrower than a pure cosine distribution, as shown graphically in Figure 4.1, and given by the equally nasty expression

$$q(\theta) = \frac{n_{\text{vap}}\alpha r^2}{2\sqrt{\pi}} \quad (4.4)$$

$$\times \begin{cases} \alpha \cos \theta + \frac{2}{\pi} \cos \theta \left\{ (1 - \alpha)R(\delta) + \frac{2}{3\delta}(1 - 2\alpha) \left[1 - (1 - \delta^2)^{3/2} \right] \right\} & \text{if } \delta < 1 \\ \alpha \cos \theta + \frac{4}{3\pi\delta}(1 - 2\alpha) \cos \theta & \text{if } \delta \geq 1, \end{cases}$$

where $\delta = \tan \theta / \beta$ and $R(\delta) = \cos^{-1} \delta - \delta \sqrt{1 - \delta^2}$.

For our geometry using a standard 0.080" thick solid conflat gasket drilled with a 0.5 mm hole, thus $\beta = 0.25$, giving a total flux reduction $w = 0.23$ over a thin-walled channel, and a distribution shown in Figure 4.1. For a room-temperature potassium source at 25°C, and using the vapor pressure formula (2.1), we get a total

flux $q_0 = 3.6 \cdot 10^{-9} \text{ s}^{-1}$. By integrating,

$$\eta_\Omega = \frac{1}{q_0} \int_0^{\theta_{1/2}} q(\theta) d\Omega, \quad (4.5)$$

we find what fraction of the total number of atoms emerging from the oven enter a cone of half-angle $\theta_{1/2}$. A graph of this integrated form for various values of β is displayed in Figure 4.2

4.2.2 Velocity distribution

The velocity distribution of atoms in an atomic beam differs from those in a closed volume of gas, due to the fact that the probability of exiting the volume of gas and leaving the orifice is proportional to v . Thus the distribution in the beam is just v times the Maxwell-Boltzmann distribution, properly normalized:

$$f(v) = 2 \frac{v^3}{\alpha^4} e^{-v^2/\alpha^2}. \quad (4.6)$$

This also means that the dependence of the capture fraction on the trap capture velocity v_c is even stronger than the vapor case and is given by

$$\eta_v = \int_0^{v_c} f(v) dv = \frac{1}{2} \left(\frac{v_c}{\alpha} \right)^4 - \frac{1}{3} \left(\frac{v_c}{\alpha} \right)^6 + \dots \quad (4.7)$$

The fraction of a room-temperature potassium beam with speeds below 10 m/s is only $3 \cdot 10^{-7}$, a factor of 60 less than for a vapor (see equation 2.5). This further emphasizes the need for high capture efficiency for a beam loaded trap.

4.3 Atomic beam collimation and slowing

4.3.1 Introduction

In chapter 1 we discuss how the spontaneous force in a MOT can be very efficient at slowing and stopping atoms whose velocity is within the ‘‘Doppler limit’’, that is, $v_{\text{atom}} < 2\lambda\Gamma$. We have already discussed (chapter 2) how an optical trap’s inherent capture velocity can be increased by using large diameter beams, high laser power, and natural enhancement due to hyperfine structure details. These factors can give

us inherent trap capture velocities a few times greater than $2\lambda\Gamma$, but this is still a tiny fraction of a room-temperature source’s average thermal velocity. In some cases, like metastable He*, the source can be cooled thermally to improve the distribution, but for alkalis with very low vapor pressures even at room temperature, this is not possible.

To efficiently couple an atomic beam source to a MOT, we must efficiently couple the broad velocity distribution of a beam can be matched to the narrow one of the trap. Small changes in the atomic velocity profile can produce large changes in the loading rate, since at low velocity the distribution goes as v^4 . Furthermore, the angular distribution of a typical atomic beam, as discussed above in §4.2, is rather broad, and either collimation of the beam, or close proximity to the trapping capture volume can produce improvements roughly as the beam-to-trap distance squared.

Some mechanical means of collimation can reduce the angular distribution, such as using a long, narrow channel, but this suffers from a severe reduction in the flux as the channel length grows. Glass capillary arrays,* consisting of small capillary tubes roughly $10\ \mu\text{m}$ diameter by $100\ \mu\text{m}$ long, arrayed together by the thousands to form a plate 5-10 millimeters in overall diameter, have been used to provide significant collimation.

The beam produced from a “typical” radioactive target is hot (typically 1000°C), has a broad angular distribution, and produces plenty of undesirable gas. Since the particular scheme to produce the radioactive potassium had not yet been designed, we tested our ideas using a simple effusive source of natural potassium.

4.3.2 Some approaches

A wide variety of schemes have been developed to collimate and slow thermal atomic beams using laser light. The essence of this problem is keeping the laser light and atom in resonance over a large range of velocities, and to do so in a manner which brings the atoms to near-zero velocity in a reasonable amount of space and time. Approaches to slowing and cooling fall roughly into two categories; alter the laser light to interact with the atoms, or alter the atoms to interact with the light. Some techniques alter both light and atom (like the MOT), and some techniques provide only slowing or only transverse cooling. This section is a very brief survey of some of these methods.

*Galileo Electro-Optics

One of the earliest techniques, barely predating the MOT itself, is chirped cooling [Ertmer et al., 1985; Watts and Wieman, 1986]. Here a circularly polarized laser is sent opposite the atomic beam direction and its frequency is swept from many linewidths below resonance to near resonance. As the laser is swept towards resonance, the atoms in a particular velocity class are brought to rest. Though simple to implement, this technique has poor efficiency because it has a low duty cycle: most of the time the laser is out of resonance with most of the atoms. This method also suffers from the fact that this technique stops the atoms at a definite point in *time* rather than a definite place in *space*.

Sheehy et al. [1989] improved this technique by combining it with collimation using transverse optical molasses, wherein resonant laser light running perpendicular to the atomic beam axis provides cooling to reduce the divergence of the outgoing beam. At the suggestion of Hoffnagle [1988] other groups (for example, Zhu et al. [1991]; Bradley et al. [1992]; Chan and Bhaskar [1995]) have purposely broadened the spectral profile of the slowing laser in addition to sweeping it, further increasing the velocity acceptance.

Still in the category of altering the light to fit the atom is isotropic slowing [Ketterle et al., 1992]. Here, an atomic beam passes through a tube whose insides are coated with a special material that has high diffuse reflectivity. Red-detuned laser light is injected laterally into the reflective tube and bounces throughout the inside, forming a “gas” of near-resonant photons. The diffuse reflector distributes the photon momentum vectors nearly isotropically. This changes the angle between the photon and atomic momentum vectors, varying the effective Doppler shift and making the light resonant with a broader atomic velocity class.

Another quite popular technique is the Zeeman-tuned slower [Barrett et al., 1991]. Here the atomic beam travels down a long, tapered solenoid with a circularly-polarized counterpropagating laser beam tuned just below resonance. The tapered coil creates a changing axial magnetic field that is large when the atoms enter and falls to nearly zero as the atoms exit. The magnetic field splits the Zeeman levels of the atom, shifting them out of resonance with the laser light. However, the atoms is shifted back into resonance by the Doppler effect, and the result is that atoms are continuously slowed as they travel down the solenoid and are brought to near-rest near the end. A long slower (roughly 1 m) can capture a good fraction of the velocity distribution ($> 10\%$), but the beam must be well-collimated to overcome solid angle losses.

4.3.3 Direct loading with collimation

Based on its simplicity and expected competitive results with substantially more complicated techniques, we opted to load the MOT directly, very close to the effusive atomic beam exit, in conjunction with transverse collimation of the beam. The argument for this is as follows: Although a Zeeman slower of length z can slow nearly the entire Maxwell-Boltzmann distribution (roughly, the maximum slowed velocity $v \propto z^{1/2}$), the flux leaving the slower falls off as z^{-2} . Since the capture fraction goes as v^4 , and the total loading rate is the product of these two factors, the effects roughly cancel one another. Without an additional, highly efficient collimation stage before the Zeeman slower, longitudinal slowing techniques suffer from severe solid angle losses that compete with the large gains in capture velocity.

By placing the trap very close to the atomic beam and by collimating it with a 2-D MOT, we expect to capture nearly 100% of the angular distribution. The high natural capture velocity of potassium, as discussed in chapter 2 gives us the ability to accept a large fraction of the velocity distribution as well, making it competitive with other, more difficult to implement techniques.

4.4 Apparatus

4.4.1 Overview and Optical system

The scheme we use is shown in Figure 4.3. Our laser system consists of a stabilized Ti:Al₂O₃ laser offset-locked to the atomic transition and described in detail in Appendix A. The two frequencies are launched along an optical fiber and sent to the trapping chamber, described below. The light is divided among trapping, transverse collimation, and longitudinal slowing. The oven consists of a small chamber containing an ampoule of potassium metal, separated from the main chamber by a solid conflat gasket with a small hole drilled in it (previously described in §4.2.1).

Viewports in the chamber arranged around the oven orifice provide optical access for four transverse cooling beams, which originate from a single, recirculated beam. The beam is retroreflected using a right-angle prism, as was done for the vapor-loaded MOT in chapter 2. Larger viewports provide access for six large trapping beams, again derived by recirculating a single beam and retroreflecting it, this time using a large quarter-wave plate and mirror to ensure good beam quality.

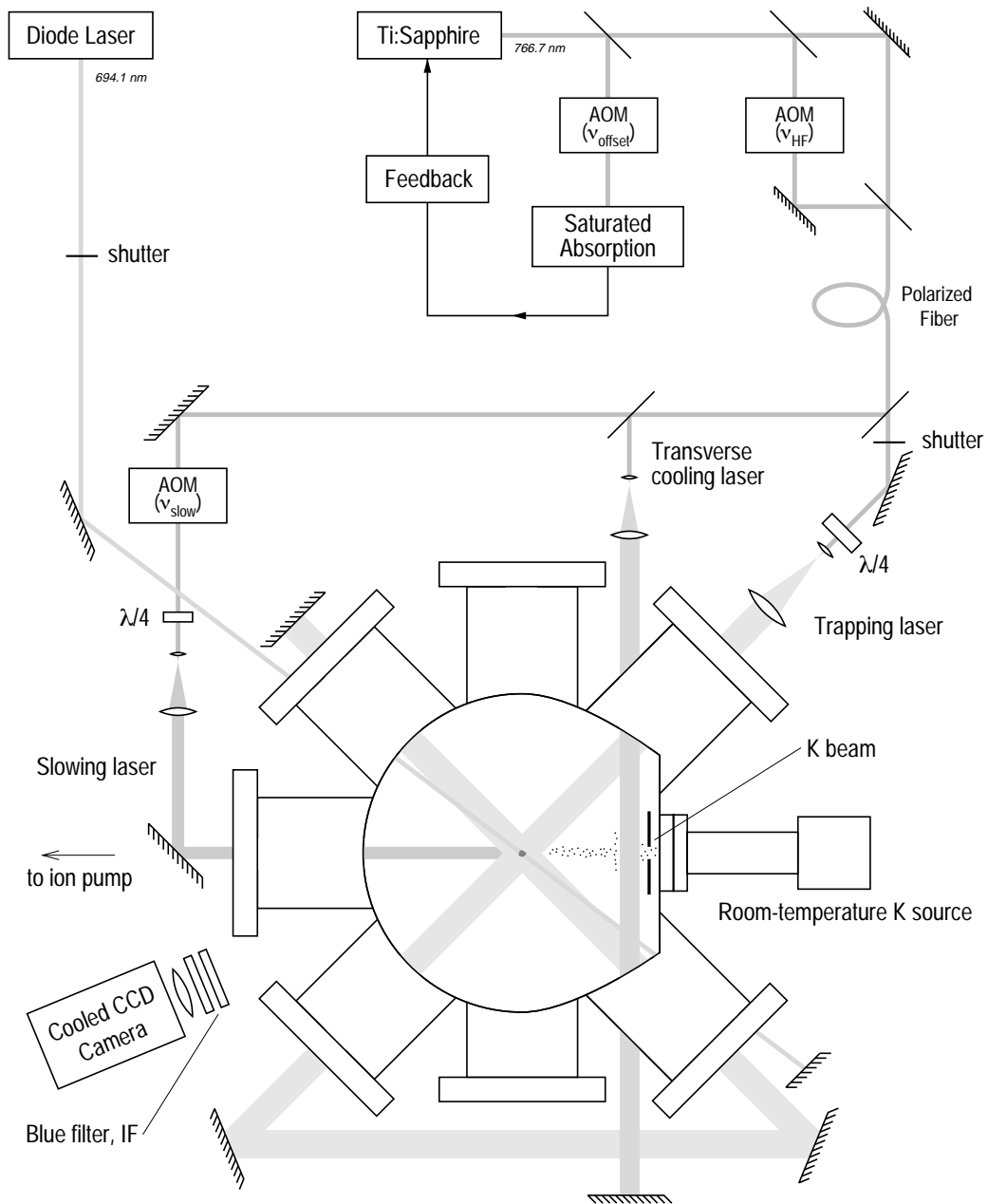


FIGURE 4.3: A schematic of our beam-loaded configuration. The Ti:Sapphire laser light is offset-locked to the ^{39}K $S_{1/2}(F=2)$ to $P_{3/2}$ transition using one AOM (ν_{offset}). Another AOM (ν_{HF}), provides light for the $S_{1/2}(F=1)$ to $P_{3/2}$ transition. The two colors are combined in a polarization-preserving fiber and emerge on a second optical table holding the chamber and trapping optics. The diode laser provide 694 nm light for the $4P_{3/2}$ to $6S_{1/2}$ transition, which produces cascade 404 nm photons that are detected by the cooled CCD camera.

For the slowing experiments, some of the transverse cooling light was sent through a tunable 40 MHz AOM and a telescope, then sent through a port opposite the oven, counterpropagating the atomic beam to provide slowing.

4.4.2 Vacuum chamber

A variety of considerations affected the design of our main trapping chamber, including being flexible enough to adapt to future changes in the experiment design. We list some of these concerns here:

- Good optical access for large trapping beams (load rate goes as the square of beam diameter), for collimation beams near the beam entrance, for fluorescence detection, and for sending optical pumping and probe beams through the trap.
- High pumping speed for long trap lifetime and to overcome gas load from target.
- Ability to insert or mount equipment into vacuum without interfering with optics or detectors. Among these things are a β detector, recoil-ion detector, and possibly small, low-inductance bias magnetic field coils.
- A large chamber reduces background due to stray radioactives stuck to the walls.

In Figure 4.4 we show a bird’s eye view of the chamber. It is roughed out through the all-metal bakeable (AMB) valve to an oil-free utility turbomolecular pump, and vacuum is maintained via a 150 l/s differential ion pump and a “Varian mini Ti-ball” titanium sublimation pump (TSP) with an effective speed of 500-1000 l/s (depending on gas species). The potassium atomic beam enters from the right via a small hole in a copper gasket. The chamber has nine large diameter viewports used for trapping and slowing laser beams, and eight smaller ports, four of which are used to collimate the atomic beam, and four are left for oblique viewing and other accessories. A detailed consideration of gas loads and pumping speeds which account for this chamber design is left to §6.4.3.

4.4.3 Magnetic field coils

Because of the large size of the chamber and the problems of placing equipment inside the chamber, we use a large pair of water-cooled magnetic field coils mounted to

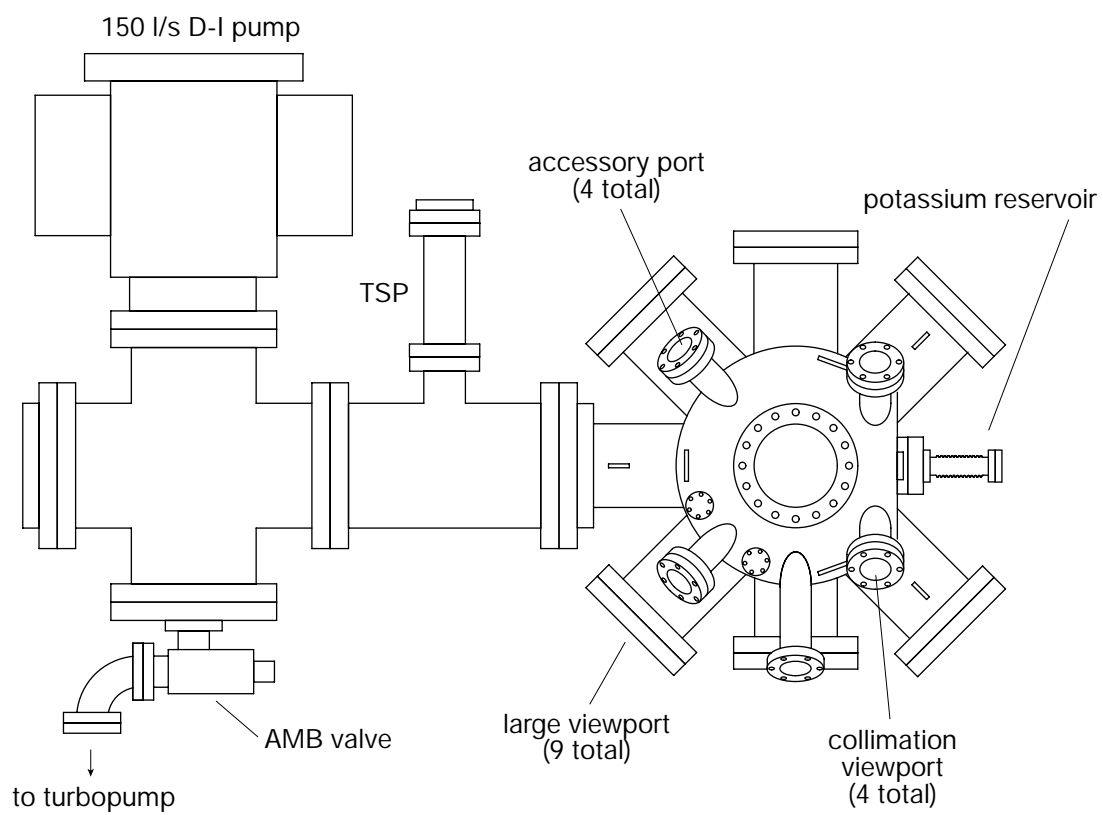


FIGURE 4.4: Simplified overhead view of main chamber ultra-high vacuum system, used for the experiments described in this and the following chapters.

the top and bottom of the chamber. Each coil has 50 turns of 6.35 mm wide by 2.54 mm thick strip wire, wound 5 turns wide and 10 layers deep. When mounted to the chamber, the coils provide a gradient of $dB_z/dz = 0.42I \text{ G/cm}$, where I is the current flowing through both coils in amperes. An analysis by Murgatroyd and Bernard [1983] regarding optimal configurations of anti-Helmholtz coils was helpful; they explain that the classic Helmholtz “coil radius equals distance between coils” configuration is optimal only when the size and position of the coils are unconstrained.

To keep them as compact as possible, each coil was wound on a removable mandrel and each layer bonded with high-temperature (400°C), high thermal conductivity, low electrical conductivity epoxy,[†] then wound with a final single layer of 3/8" copper tubing for cooling. After the epoxy is cured, the entire coil was wound helically with kapton tape to prevent bits of epoxy from flaking off.

The coils are then securely taped to a circular yoke bearing three tabs, which mount to brackets with matching tabs on the chamber via vibration-damping grommets.[‡] The flanges over which the coils are mounted have split conflat-style receiver rings (two C-shaped pieces), allowing the inside diameter of the coils to be somewhat smaller (12.5 cm). When mounted, the inside surface of the coils are separated by 15.2 cm.

Taken alone, these anti-Helmholtz coils produce a single point with $B = 0$, where the main trap lasers intersect to form the trap. But for effective collimation, we must create another $B = 0$ region where the collimating beams intersect. This is done by adding a second, smaller coil (or “bucking” coil) with a field opposing the main anti-Helmholtz coils. This coil is a rectangle 15 cm by 8.4 cm, having 80 turns of 14 gauge wire, with its plane centered 13.3 cm from the trap.

An additional, larger main trap shim coil is placed opposite the bucking coil to correct the shift in the main trap field zero caused by the bucking coil. These coils are a rectangle 36.8 cm by 28.6 cm, centered 8.3 cm from the trap, and has 20 turns of 14 gauge wire.

We have calculated the total field of the four coils carefully in order to adjust the current flowing through each. Figure 4.5 shows the magnetic field coil configuration, showing the relative locations of the main anti-Helmholtz coils, bucking coil and shim

[†]Stycast 2762FT and catalyst 17, from Grace Specialty Polymers. The epoxy cures at high temperature to a stone-like consistency.

[‡]Isodamp C-1002, an engineered thermoplastic made by E-A-R Specialty Composites, available as “PVC grommets” through McMaster-Carr Supply Company. According to the manufacturer, the plastic composite is designed “to turn vibrations into heat.”

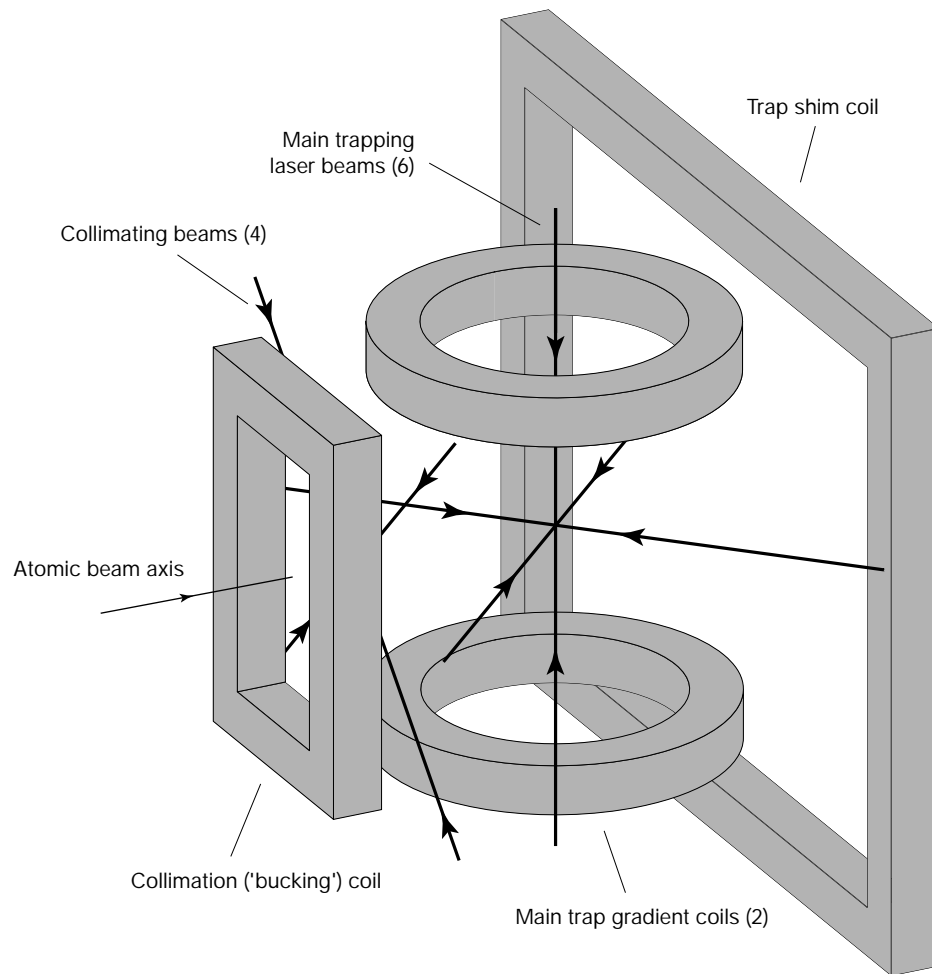


FIGURE 4.5: Beam collimation magnetic field configuration.

coils, the axes along which the trap and collimation beams travel, and the atomic beam axis.

4.5 Results

Using the configuration described above, we have measured loading rates of the trap from an effusive beam as a function of detuning, both collimated and uncollimated. We have also measured the enhancement of the loading rate by adding a detuned, counterpropagating slowing beam. These loadings rates represent the optimum operation we were able to achieve given the limitations presented by the geometry of the chamber, available laser power, and magnetic field configuration.

To begin, we optimized the operation of the trap alone by adjusting the alignment, collimation, and diameter of the main trapping beams. In our previous vapor MOT configuration we used a separate retroreflected beam for each axis (see Figure 2.4), which is reasonably easy to align. Here, to utilize our laser power more efficiently, we send a single, large-diameter beam through all three orthogonal axes. Refer again to Figure 4.3, which shows how we do this for two of the three axes. The results is three beams propagating in the $+x$, $+y$, and $-z$ directions; by adding a waveplate and retroreflector, we generate the beam for the $-x$, $-y$, and $+z$ directions.[§]

Especially good beam alignment and retroreflection were necessary to make the trap work efficiently; with some practice this has become an easy task, aided in part by the large diameter of the beams. Despite the fact that every port window is antireflection coated and the mirrors are high-reflectivity dielectric stacks[¶], after passing through or reflecting from 35 surfaces with roughly 0.1% loss each, there is a small overall loss of power. We counter the effect of this by slightly focusing the beam emerging from the telescope; this adjustment and the alignment of the retroreflecting mirror act as final adjustments in optimizing the trap. The beam diameter ($2w_o = 3.4$ cm) was chosen to approximately fill the 3" aperture of the mirrors without suffering significant diffraction.

Adjustments to the atomic beam collimation followed a similar routine. The beam was located as closely as the oven hole as possible (beam axis 2.8 cm from the oven

[§]Note that because the magnetic field direction points out along the z direction (see §1.3.2) but in upon the $x - y$ plane, the beam must be reflected an even number of times in the $x - y$ plane and an odd number of times in going from the x - or y -direction to the z -direction.

[¶]Melles Griot, Irvine, Ca.

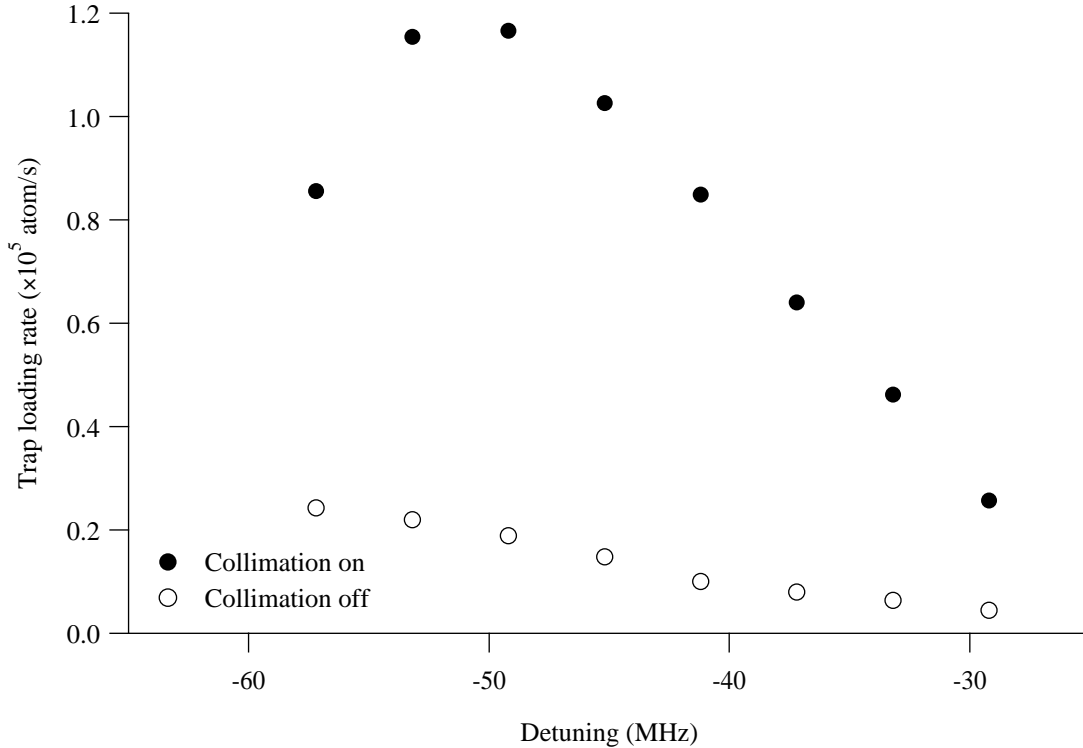


FIGURE 4.6: Loading rate of ^{39}K into beam-loaded trap. Atomic beam flux $Q_0 = 2.2 \cdot 10^9 \text{ s}^{-1}$, with bucking and shimming magnetic fields along z -axis. Trap $dB/dz = 11 \text{ G/cm}$, collimation $dB/dz = \sim 3 \text{ G/cm}$, trap $I_{\text{tot}} = 180 \text{ mW/cm}^2$ ($w_0 = 1.7 \text{ cm}$), and collimation $I_{\text{tot}} = 460 \text{ mW/cm}^2$ ($w_0 = 0.85 \text{ cm}$).

orifice surface), and had a waist diameter $2w_0 = 1.7 \text{ cm}$. A variety of polarizations and magnetic field values (bias and gradient) were also tried. Optimal collimation operation occurred when the magnetic field was zero but provided a moderate gradient of about 3 G/cm and for nearly perfect circular polarization, all consistent with the conditions for a two-dimensional MOT.

4.5.1 Loading and effect of collimation

The loading rate as a function of detuning for our fully optimized configuration, both collimated and uncollimated, is shown in Figure 4.6. Note that collimation loading rate turns over at about $\Delta = -55 \text{ MHz}$ while the uncollimated rate is still rising. This may be attributed to the collimation having a smaller capture velocity, probably due to the smaller diameter beams. The peak of the collimated loading rate is about

eight times the peak of the uncollimated rate, and represents $5 \cdot 10^{-5}$ of the total flux effusing from the source.

From our knowledge of the angular beam distribution (§4.2.1) and the trapping and collimating beam diameters, we can make an estimate of the trap capture velocity v_c . With a trap diameter of 3.4 cm, 13.6 cm from the oven hole, we get a half-angle $\theta_{1/2} = 7.1^\circ$. From equation 4.5 (plotted in Figure 4.2) we get the total amount of flux from our $\beta = 0.25$ channel into that half-angle, 1.2%. Since the total loading rate is the product of the velocity capture fraction and the solid angle fraction

$$\eta_{\text{tot}} = \eta_v \eta_\Omega \quad (4.8)$$

we can use the peak uncollimated loading rate ($L = 25,000 \text{ s}^{-1}$) from Figure 4.6 to determine that $\eta_v = 9 \cdot 10^{-4}$. From the formula for η_v , equation 4.7 we find a capture velocity $v_c = 72 \text{ m/s}$, large for the alkalis, but not unreasonable for potassium.

Continuing further, we can use these measurements to determine the effective solid angle that the collimating beams send into the trap region. Using the velocity capture fraction η_v we determined from the uncollimated data and the total capture fraction with collimation on, we find $\eta_\Omega = 6\%$ for the collimation, which corresponds to $\theta_{1/2} = 20^\circ$.

4.5.2 Slowing laser

We also added a weak slowing laser beam of approximately 7 mW/cm^2 and observed the loading rate roughly double; see Figure 4.7 for our data. From the graph inset we show that intensities much beyond saturation do not materially improve the loading rate.

We tried a variety of slowing beam diameters and even detuned it slightly from the trap frequency by using a separate AOM. In general, it was difficult to effectively optimize the slowing beam because of its strong effect on the operation of the trap at high intensities. Other configurations, including focusing the beam onto the effusive oven hole and sending a collimated beam at an angle to avoid the trap was tried. The improvement is clear, but was not overwhelming enough for us to incorporate it as part of our final design.

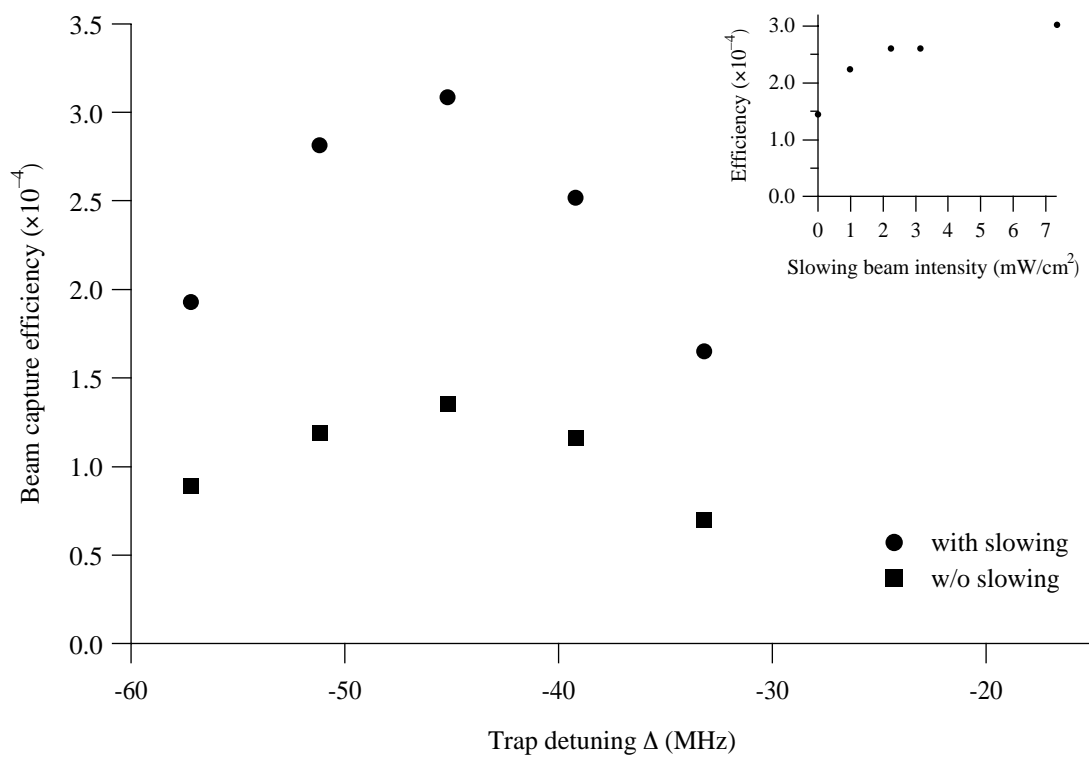


FIGURE 4.7: Effect of slowing beam on trap loading rate.

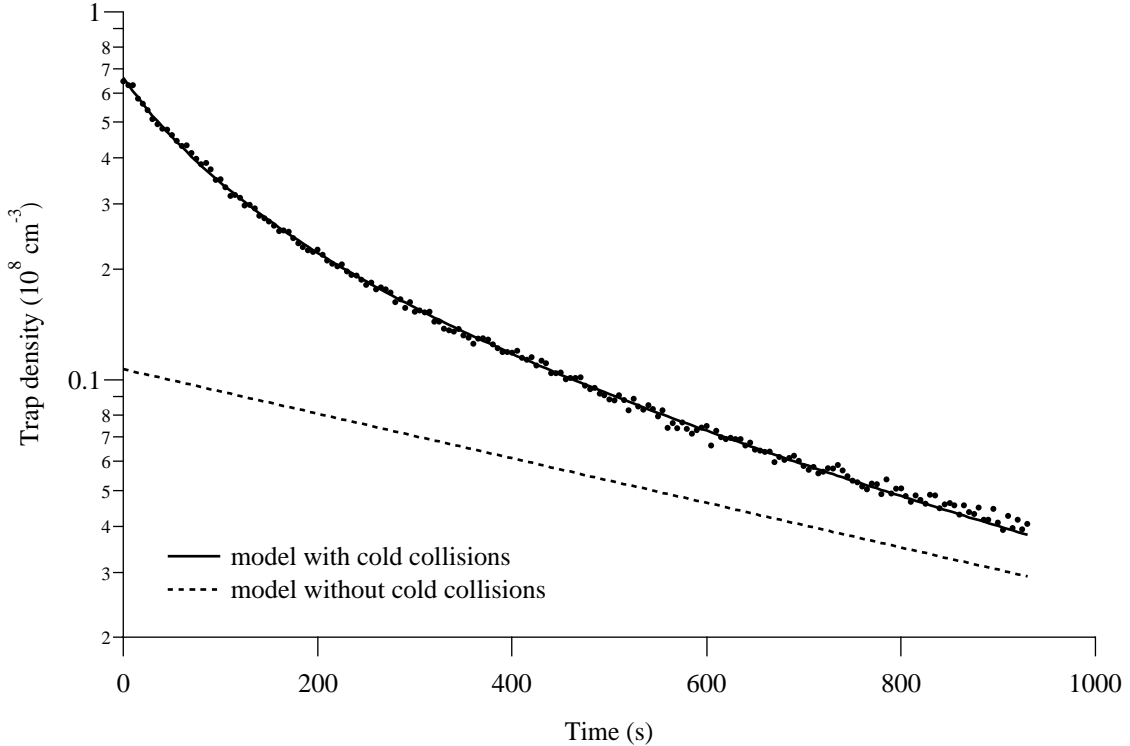


FIGURE 4.8: Loss rate transient for ^{41}K , loading off, $\Delta = -30.5$ MHz, $I_{\text{tot}} = 300$ mW/cm 2 , $dB/dz = 10.5$ G/cm. For both model fits (including and not including cold collisions), the loss rate due to hot background atoms $\alpha = 0.00139$ s $^{-1}$. For the model including cold collisions, $n_0 = 6.7 \cdot 10^7$ cm $^{-3}$, $\beta = 1.1 \cdot 10^{-10}$ cm 3 /s; for the model without, $\beta = 0$, $n_0 = 1.1 \cdot 10^7$ cm $^{-3}$. Thus the dotted line represents hot background atoms collisions, and the difference between the dotted and solid lines is the contribution from ultracold collisions only.

4.5.3 Trap lifetime

By loading the trap from an atomic beam rather than a background vapor, we can reduce the background pressure to an arbitrarily low pressure while still maintaining a useful loading rate. Although loading from a beam reduces the loading rate considerably over the room-temperature vapor case, the huge increase in trap lifetime possible at low pressures more than counters this effect.

As we lower the background vapor pressure we also reduce γ , such that βn is comparable in magnitude. But we also have the luxury of being able to turn off the

loading term ($L = 0$), allowing us to rearrange equation 3.1 as

$$\frac{-dn}{\gamma n + \beta n^2} = dt \quad (4.9)$$

which we can integrate and solve to get

$$n(t) = \left[\left(\frac{1}{n_0} + \frac{\beta}{\gamma} \right) e^{\gamma t} - \frac{\beta}{\gamma} \right]^{-1}, \quad (4.10)$$

where $n_0 = n(0)$, the initial density. Here we work in a different regime than in chapter 3, in that the trap is nearly empty and the density n is varying. Note that it is tempting to avoid this messy fitting by simply plotting \dot{n}/n against n , but the additional noise in \dot{n} resulting from numerically differentiating the noisy loading rate data $n(t)$ produces more error in γ than does this technique.

So we fit our loss rate data to equation 4.10, leaving n_0 , γ , and β as free parameters. In Figure 4.8 we clearly see the effects of trap-loss collisions as well as measure an extremely long background-pressure limited lifetime of 720s. It is obvious from this plot that at short times (and higher trap densities), the loss rate is dominated by β , whereas after a long time, the loss rate is dominated by γ . Also plotted in this figure are the results of this model with $\beta = 0$, the curvature of the data showing clearly how cold collisions drastically shorten the trap lifetime at high densities. As the trap empties and the density falls, cold collisions are less dominant and the trap loss rate approaches a simple exponential, shown by the dotted line.

Chapter 5

Magneto-optical funnel

5.1 Introduction

In order to study radioactive isotopes with moderate lifetimes (tens to hundreds of seconds), we need to trap them in a chamber with as low a pressure as possible to minimize background gas collisions thereby extending dwell time in the trap. However, the target region where the radioactive atoms are made (described in chapter 6) has an inherently high gas load and limited pumping speed, making it necessary to transport the radioactive atoms from the target to a region of low pressure where they can be trapped and other experiments performed.

It is of equal importance to load the trap with high efficiency from the production region. In fact, this problem also has interest among those doing Bose-Einstein condensation [Jin et al., 1997; Bradley et al., 1997; Andrews et al., 1997], where long trap lifetimes and a large sample of atoms are necessary for efficient evaporative cooling.

In this chapter we describe the design of a magneto-optical funnel that produces a collimated source of cold atoms from a vapor cell. We begin with some background material, describing a few of the past techniques for producing a cold, collimated beam of atoms (§5.2). We describe our unique funnel design in section 5.3 and give details of the overall apparatus in section 5.4. Our observations on the operation of the funnel operating as a MOT and of using the funnel to load a UHV MOT, separated from the funnel by a low-conductance region with additional pumping are given in section 5.5.

5.2 Background

Two popular methods for loading a MOT are direct capture from an atomic vapor, [Monroe et al., 1990] and using a thermal atomic beam and Zeeman slower [Barrett et al., 1991]. Both methods introduce a large number of uncaptured atoms into the chamber, raising the pressure, depositing untrapped atoms on the chamber walls, or both. For experiments involving radioactive isotopes, the untrapped atoms are a potential source of background when studying nuclear decay processes. Furthermore, to produce cold, dense samples by evaporative cooling in a magnetic trap loaded from a MOT, pressure in the low UHV range is necessary for lifetimes of tens or hundreds of seconds. One way to optimally load a UHV MOT from a source of higher pressure is to load the MOT from a low-velocity, collimated beam of atoms that passes through a low-conductance hole or tube. The slow atomic beam can be efficiently captured by the MOT while presenting a minimal gas load or radioactive background in the low-pressure chamber.

Several methods have been used to efficiently transfer slow atoms into a MOT. Gibble et al. [1995] used two traps, and transferred the atoms from the first to the second using moving optical molasses, requiring lasers (or modulators) additional to those used for trapping. Wieman and coworkers transferred cold atoms between two traps using a separate “push beam” to knock the atoms out of the first trap and send them along to the second. But because the atoms are heated during transport, a long sextupole magnet along the entire transport region was required to confine the atoms in the transverse direction during transport [Myatt et al., 1996].

A simpler alternative method is to use an “atomic funnel” that produces a slow, collimated atomic beam. A number of promising funnels and funnel-related devices [Riis et al., 1990; Nellessen et al., 1990; Yu et al., 1994; Swanson et al., 1996; Lu et al., 1996] have been demonstrated, and were carefully considered before we converged on our design.

The device of Nellessen et al. [1990] used an atomic beam and an optical deflector to separate the atoms of slow longitudinal velocity from the fast atoms, then uses a 2-D MOT to provide transverse cooling and compression. However, this is inefficient because it wastes the majority of the atoms, which are in the fast part of the thermal Maxwell-Boltzmann distribution. Yu et al. [1994] used a similar 2-D MOT arrangement to produce a highly compressed beam, but instead of deflecting the slow atoms from

the main beam, adds a counterpropagating longitudinal chirped slowing laser. This uses more of the atoms, but the chirped slowing is still somewhat inefficient, and this arrangement does not quite satisfy our requirements.

The funnels of Riis et al. [1990] and Swanson et al. [1996] are quite similar. They create a 2-D MOT loaded at an oblique angle by a slowed atomic beam. Both funnels have *in vacuo* hairpin magnetic field wires to provide the required quadrupole magnetic field. Both use separate moving optical molasses beams to control the longitudinal velocity of the outgoing cold beam, requiring significant optical complexity and multiple laser frequencies to operate, as well as having components *in vacuo*.

The LVIS (Low-Velocity Intense Source) of Lu et al. [1996] has superb efficiency and output beam characteristics and a geometry which is promising for collection of our radioactive beam. It consists of a standard 6-beam MOT, but with one small difference: along one axis, the beam is retroreflected by a waveplate/mirror* side with a small hole drilled in the center, allowing the central portion of the beam to emerge rather than be retroreflected. Atoms are collected as in a normal vapor-cell MOT, but are pushed out of the cell by the unbalanced beam. This is a very nice design, but still has the optical complexity of a full MOT.

We have designed a funnel (based on the pyramidal-mirror MOT of Lee et al. [1996]) that cools in three dimensions, loads from a vapor, and is efficiently coupled to a UHV MOT. This funnel combines the good features of the LVIS with optical simplicity.

We have to fulfill a variety of requirements:

- In order to keep the radioactive atoms from instantly reacting and sticking to the chamber walls, we must coat the surfaces with dryfilm. This allows the atoms to bounce on surface and accumulate in the cell.
- For maximum number of bounces, the area of coated wall surface must be large compared to any uncoated surface or ports in the cell.
- A capture volume large compared with the volume of the cell, i.e., a maximal fraction of the cell must be filled by light.
- The cooled beam exit must present a minimal gas load to the vacuum system.
- The cell must interface with the radioactive beam, as well as be sufficiently pumped through this port.

*a quarter-wave plate with a hole drilled down the middle and coated on one side with with gold

5.3 Description

The heart of our funnel system is a four-sided hollow pyramidal mirror whose sides form a 90° included angle, with a small hole drilled at the apex, shown schematically in Figure 5.1. A single, large-diameter circularly-polarized beam is incident axially, illuminating the entire pyramid. Each mirror segment reflects a quadrant of the beam toward the axis, and the segment on the opposite side reflects it a second time, sending it back toward the original beam direction.

Each of these reflections approximately reverses the helicity of the light (whose sense is shown by small black arrows in Figure 5.1). When combined with an appropriate spherical quadrupole magnetic field (grey arrows in inset of Figure 5.1), the angular momentum carried by the light produces the correct MOT forces [Walker, 1994]. These forces are present everywhere inside the pyramid except along the central cylindrical region, where there is no retroreflected light due to the hole in the pyramid apex.

Atoms entering the funnel are slowed, cooled, and pushed towards the axis, where they are pushed out of the pyramid by unbalanced radiation pressure. As they leave the funnel, they continue to be accelerated by the narrow light beam exiting the pyramid. Eventually the acceleration is reduced as the atoms Doppler-shift out of resonance by a few linewidths. The result is a slow, collimated atomic beam whose velocity is matched to the MOT capture range.

Note that in their first paper, Lee et al. [1996] made a MOT with both a four-sided pyramid and an axicon (hollow cone). Based on their results and on some simple calculations we performed using a simple damped harmonic oscillator model of the capture mechanism (using damping and spring constants from our six level rate equation model, §2.4), it appeared that an axicon geometry had inferior loading characteristics due to the fact that the light field provides no damping of the atomic motion in the $\hat{\phi}$ direction. More recently however, the same group [Kim et al., 1997] has created an axicon trap using higher quality mirrors than previously and determined that the loading rate of the axicon trap and pyramid trap are roughly equivalent.

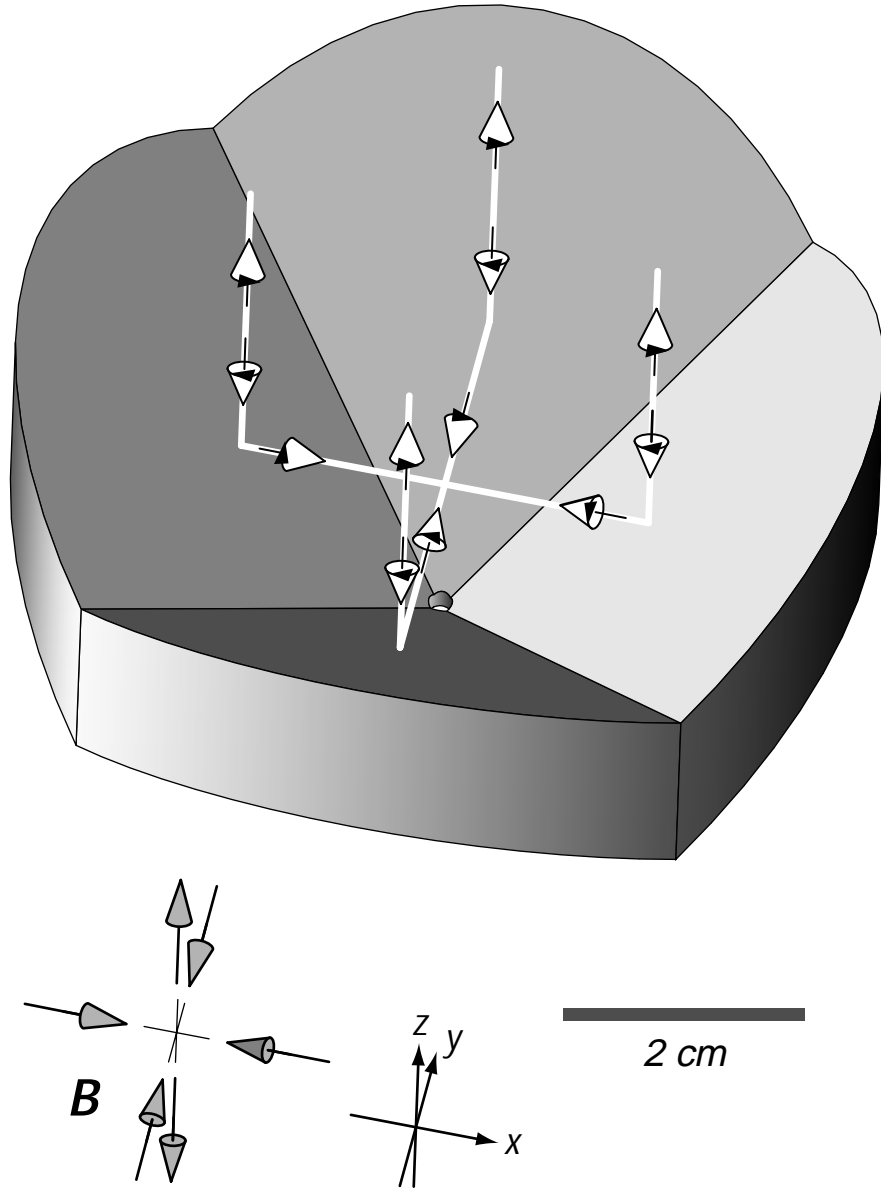


FIGURE 5.1: Detail of the pyramidal funnel. The funnel is illuminated from above by a single large diameter σ^+ polarized laser beam. The beam is reflected by each quadrant of the mirror towards the axis, then reflects from the opposite quadrant back along the original propagation direction. Each reflection reverses the helicity of the light, which in combination with a spherical quadrupole magnetic field (indicated in the inset with grey arrows), creates the correct forces for trapping. Note the small hole at the apex of the pyramid where the atoms and laser light escape.

5.4 Apparatus

The funnel is comprised of four identical OFHC copper pieces, formed to make a right hollow pyramid inside and a cylinder outside (7 cm in diameter), with a 1 mm hole of conductance ~ 0.05 l/s through the apex. The surfaces of the mirrors were highly polished, gold electroplated,[†] and evaporatively coated with SiO₂.[‡] The silicon dioxide coating both protects the gold from the corrosive effects of the alkali and provides a surface for the dryfilm coating (discussed in Appendix C) to attach itself to. Figure 5.2 is a picture of the pyramid from the top, or mirror side, showing the pyramidal hollow and polished mirror surfaces.

The four pieces were carefully machined by our local shop before being polished using traditional mirror polishing methods using pitch. Each of the non-mirror mating surfaces are relieved with a shallow groove down the center of each surface so that the pieces will register kinematically and accurately, as well as provide a relief path to prevent virtual leaks inside the vacuum system that the pyramid is placed in. The four pieces are held together with vented cap screw bolts; this holds them together as shown in Figure 5.3.

The pyramid is attached to a solid Conflat copper gasket with holes drilled to accommodate mounting bolts and the emerging atomic/laser beam. The pyramid is mounted in a custom vacuum cell, shown in Figure 5.4. One end of the vacuum cell has a glass-to-metal seal with an uncoated pyrex window to let in laser light. The other end is a 4-5/8" conflat port to which the pyramid and copper gasket are mounted. Finally, a small port enters the side of the cell at an angle of 60° to the symmetry axis to allow introduction of atoms and pumping of the cell.

In addition, for the experiments with radioactive atoms described in chapter 6, we added a pyrex glass liner and glass tube, constructed to closely fit the inner shape of the chamber/pyramid combination. The liner and tube are approximately 0.1 in thick.[§] To ensure a good fit and check tolerances, we created a mock-up of the glass liner made of aluminum, using a lathe and Dremel tool. When assembled, the glass tube, liner, window, and SiO₂ coated mirrors form a nearly contiguous surface which

[†]More specifically, the plating consists of a thin gold layer for good adhesion to the copper, a thick layer of rhodium as a diffusion barrier (copper and gold have a high diffusion coefficient even at room temperature, which over time can reduce the reflectivity of the gold), and then a final layer of gold that forms the optical surface.

[‡]by Rocky Mountain Instruments, Inc.

[§]Beste Sci-Glass, Grafton, Wisconsin

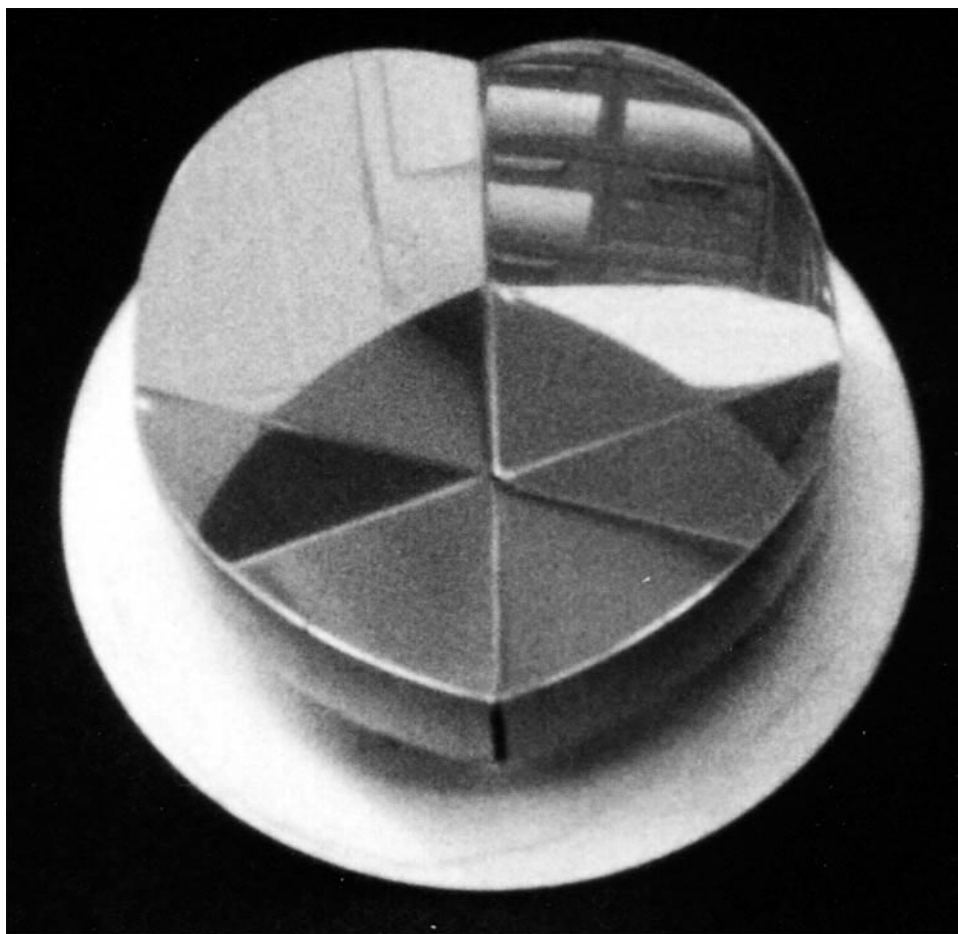


FIGURE 5.2: Top view photo of pyramid, mounted to a solid conflat gasket.

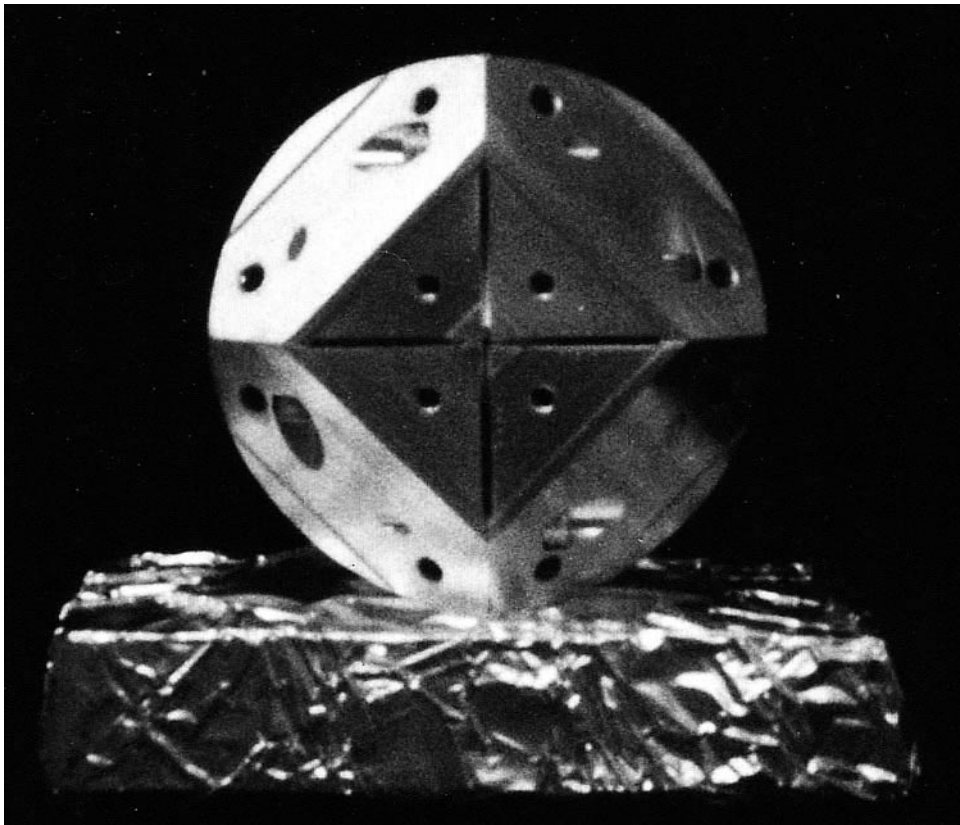


FIGURE 5.3: Bottom view photo of pyramid, showing how it is assembled.

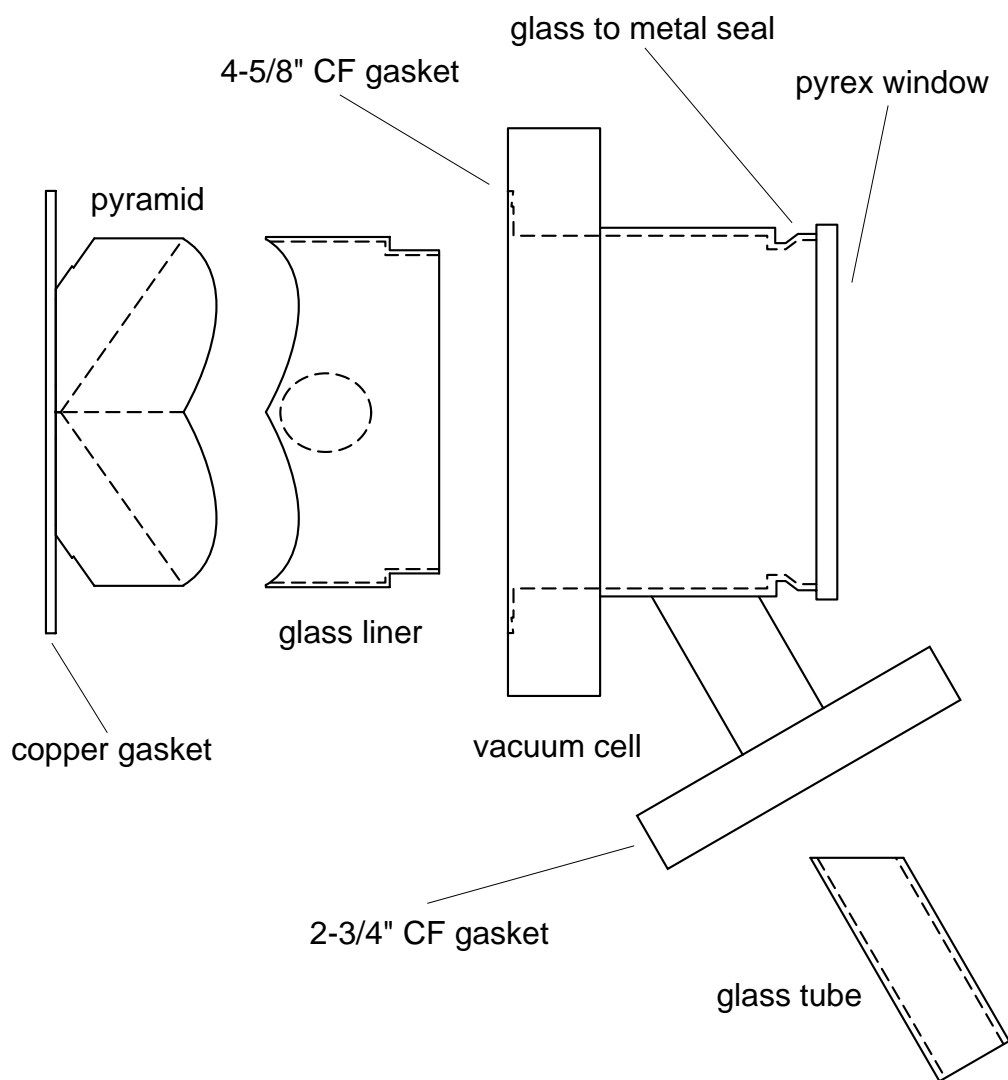


FIGURE 5.4: Exploded view of the pyramid, crown-shaped glass liner, glass tube, and vacuum cell (shown approximately 60% full scale).

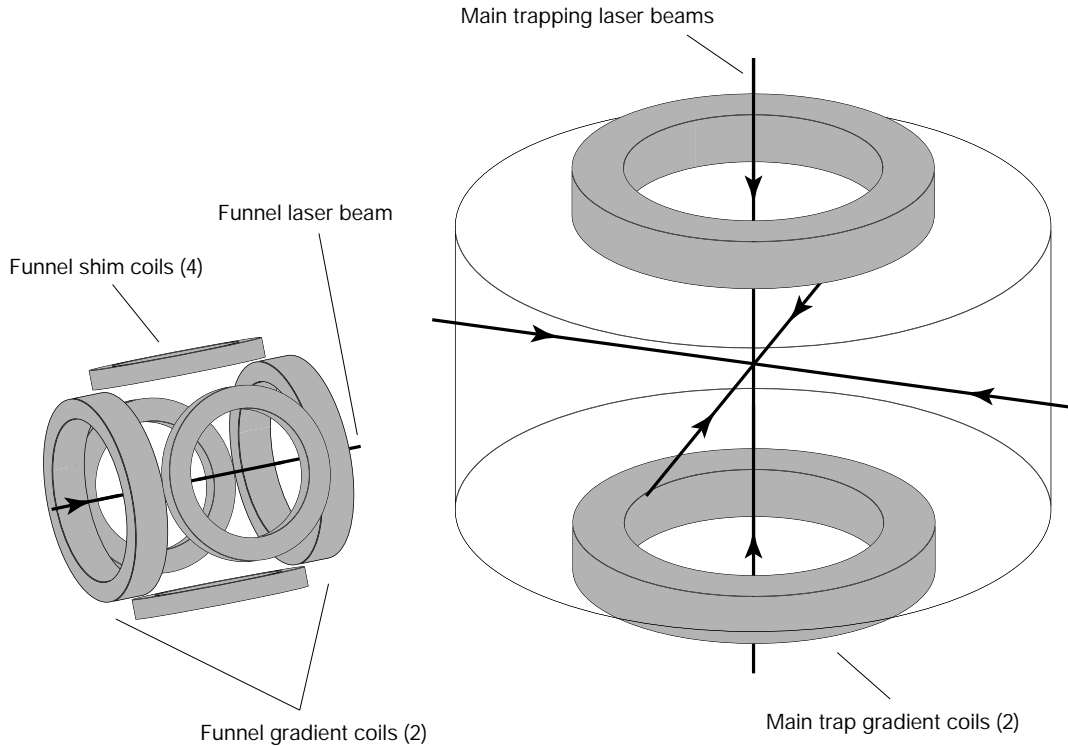


FIGURE 5.5: Funnel-loaded trap magnetic field configuration.

can be dryfilm coated. Based on the ratio of the surface area of the cell to the area of the angled inlet port, atoms entering the cell should average more than 80 bounces before leaving.

Due to the tight space limits imposed by the final experiment (with large chamber and radioactive target), six custom-designed magnetic-field coils were used, all wound on aluminum forms. One pair of coils is mounted axially on the chamber to provide the magnetic field gradient; this axis corresponds to the z -axis of Figure 5.1. Each coil consists of 25 turns of 12 gauge high-temperature magnet wire[¶]. The coil forms have an inside diameter 8.4 cm and possess a channel 1.2 cm wide. For a typical center-to-center distance (measured from the center of the windings only) between coils of 10.6 cm, the applied gradient is $dB_z/dz = 0.62I$ G/cm, where I is in amperes. Magnetic field bias (shim) in the z -axis is provided by an adjustable electronic current shunt, which reduces the amount of current flowing in one of the two anti-Helmholtz coils. Figure 5.5 shows the configuration of magnetic field coils used for the funnel-loaded MOT, showing the six coils surrounding the funnel, and the main trap anti-

[¶]Belden heavy armored poly-thermaleze.

Helmholtz coils.

The other four coils, all identical in shape, provide field shimming in the x - and y -directions, and consist of 60 turns of 20 gauge wire, wound on an aluminum form of inside diameter 7.14 cm with a 0.71 cm wide channel. These four coil frames are screwed together with small angle brackets to form a square, as shown in Figure 5.5. They are mounted around the pyramid vacuum chamber and held using standard optical posts and holders. Each pair provides a uniform shim field of 2.86 G/A.

The laser system is precisely the same as used in the previous beam-loaded experiments (see §4.4). The two colors of light are combined in a fiber, emerge, and is collimated by a microscope objective. The roughly 1.5 mm collimated pencil beam is sent towards the axis of the pyramid, circularly polarized, and is expanded by a telescope consisting of a high-quality 40 \times microscope objective and $f = 120.8$ mm, 100 mm diameter lens, producing a gaussian beam of waist $w_0 = 3$ cm.

5.5 Measurements

5.5.1 Pyramidal MOT

For the initial proof-of-concept experiment, creating a regular MOT using the funnel mirrors, the cell was neither glass-lined nor coated with dryfilm. In addition, our first mirror was not SiO₂ coated, and the surface reflectivity degraded over the course of a few weeks due to exposure to a vapor of 10⁻⁹–10⁻⁸ torr of potassium. The initial test system consisted of an ion pump and potassium reservoir attached to the small angled arm, and the pyramid outlet was blanked off with a viewport.

We demonstrated the ability to trap roughly $4 \cdot 10^7$ atoms at a pressure of 10⁻⁸ torr. Figure 5.6 shows a typical ball of potassium atoms in the funnel MOT; note the two additional images flanking the trap caused by multiple reflections from the pyramid mirrors. As usual, we estimate the number of atoms by measuring the fluorescence of the trapped atoms, and use our six-level model to calculate the excited-state fraction ρ_e .

To find ρ_e , we also need to know the total intensity at the trap. Consider the coordinate system shown in Figure 5.1 with its origin located at the apex of the

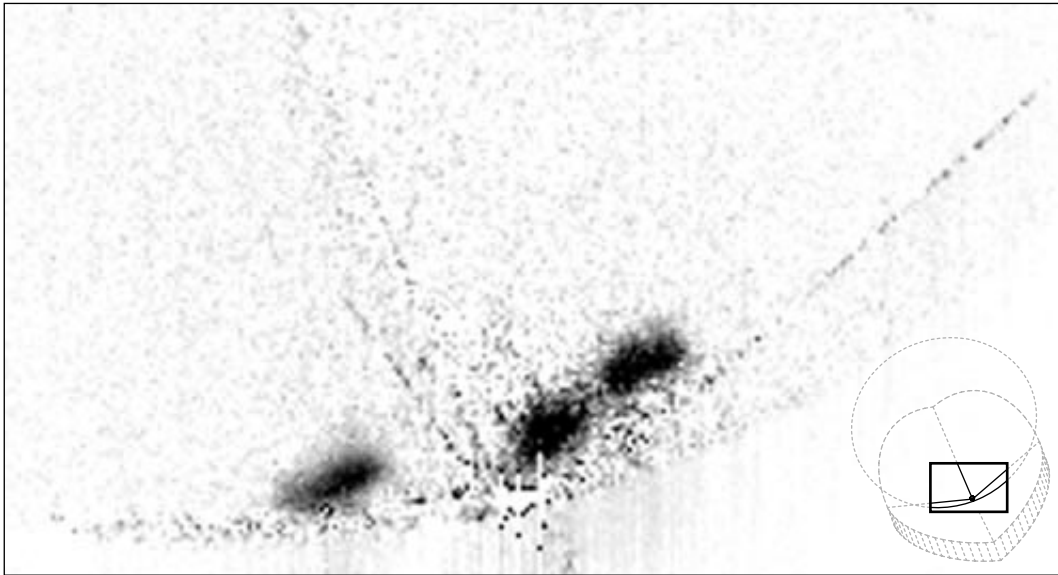


FIGURE 5.6: CCD camera image of potassium trapped in pyramidal funnel with substantial scattered light background from the mirror subtracted. (The inset in lower right corner shows relative location of image in the funnel.) The middle blob is the actual ball of atoms, flanked on either side by images produced the by the pyramidal mirrors. To create a trap, the pushing beam has been retroreflected with a mirror and quarter-wave plate, and the magnetic field has been biased slightly along the axis to make the ball of atoms more visible. The number of atoms here is approximately $1.3 \cdot 10^7$.

pyramid. For a trap at location (x, y, z) , a gaussian beam

$$I(x, y) = I_0 e^{-2(x^2+y^2)/w_0^2} \quad (5.1)$$

propagating along $-z$, and mirrors of reflectivity R , the intensities of the each beam will be

$$I_{\pm x} = RI_0 e^{-2(y^2+z^2)/w_0^2} \quad (5.2)$$

$$I_{\pm y} = RI_0 e^{-2(x^2+z^2)/w_0^2} \quad (5.3)$$

$$I_{-z} = I_0 e^{-2(x^2+y^2)/w_0^2} \quad (5.4)$$

$$I_{+z} = R^2 I_0 e^{-2(x^2+y^2)/w_0^2}, \quad (5.5)$$

assuming the apex hole is vanishingly small. The total intensity on-axis ($x = y = 0$) simplifies to

$$I_{\text{tot}} = I_0 \left(1 + R^2 + 4Re^{-2z^2/w_0^2} \right), \quad (5.6)$$

which is what we use to calculate ρ_e . For our first set of mirrors, which were seriously damaged by the plating company^{||}, $R \approx 85\%$, reduced mostly by light scattered from the heavily scratched surface. Later, for the transfer efficiency experiment, we used re-polished mirrors which have $R \approx 96\%$, nearly the maximum for gold at 770 nm.

From these experiments we learned some rough characteristics of the operation of a pyramid trap. It operates for detunings, intensities, and magnetic field gradients quite similar to those of a conventional six-beam MOT, but appears to very sensitive to the DC magnetic field shim. We also learned that the uncoated gold surface is a very effective pump for the alkali atoms we introduced, making it difficult to estimate the effective vapor pressure near the trapping region and thus the overall trapping efficiency.

5.5.2 Pyramidal Funnel

We next connected our funnel and the XHV MOT chamber that was described in chapter 4. The integrated apparatus is shown in Figure 5.7. Potassium atoms that exit the funnel travel through a differentially pumped region and a 0.5 cm diameter orifice to a MOT operated at a pressure of $\sim 10^{-11}$ torr (trap lifetime, 150 s). The

^{||}Acteron Corporation.

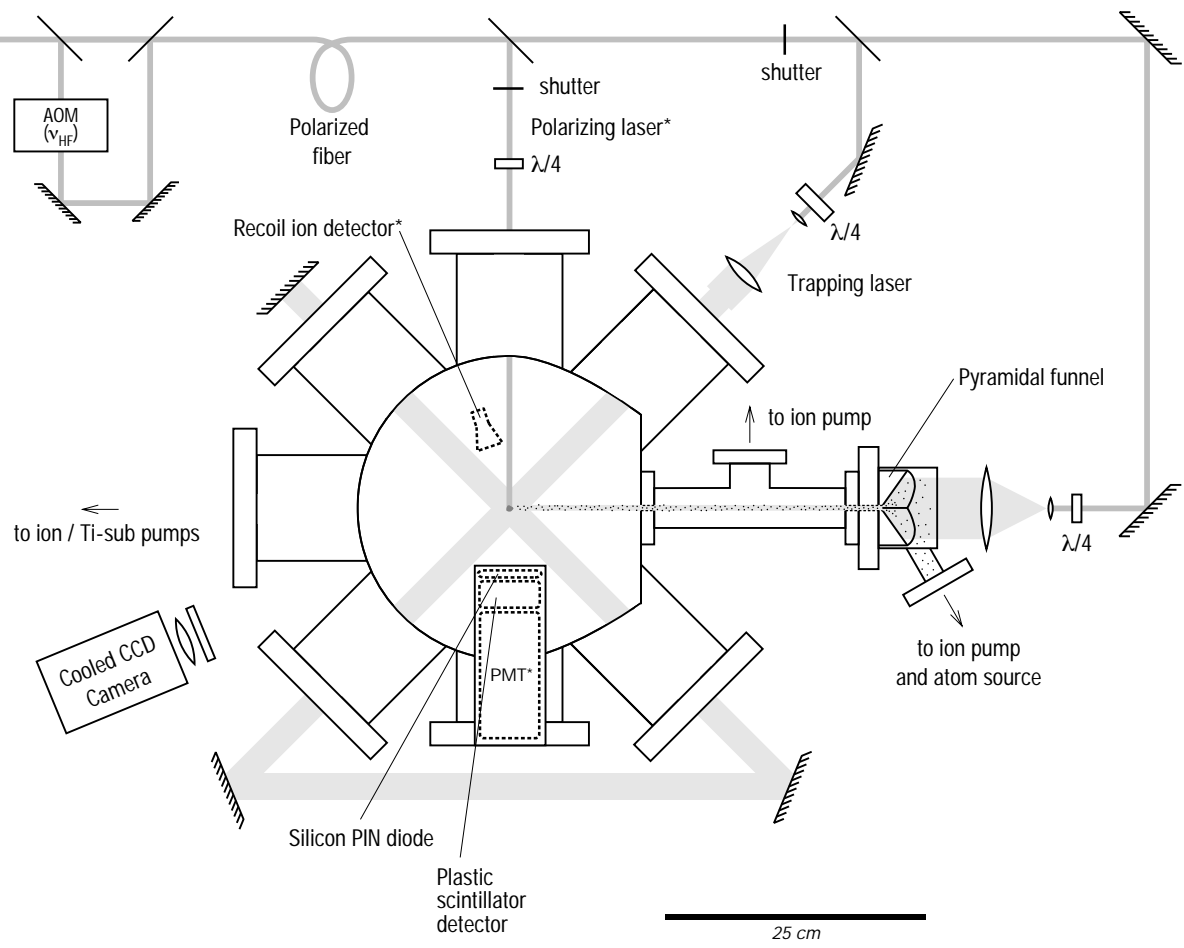


FIGURE 5.7: A schematic of our apparatus. The Ti:Al₂O₃ laser light, tuned to the desired potassium isotope ($A = 37-41$) is offset-locked to the ^{39}K $S_{1/2}$ ($F = 1$) to $P_{3/2}$ transition using one A-O modulator (ν_{offset}). Another A-O modulator (ν_{HF}), provides light for the $S_{1/2}$ ($F = 1$) to $P_{3/2}$ transition in the trapped isotope. The two colors are combined in a polarization-preserving fiber and emerge on a second optical table near the accelerator which holds the vacuum chamber and trapping optics. Half of the emerging laser power is sent to the main trap and half to the pyramidal funnel. A small vapor pressure (sub room-temperature) of potassium is present in the funnel. The laser light cools and slows the atoms, pushing them towards the vertex of the funnel where they are finally pushed out the hole in the base of the funnel. The atoms then travel to the other chamber where they are finally trapped in a conventional MOT. *To be added (see chapter 7).

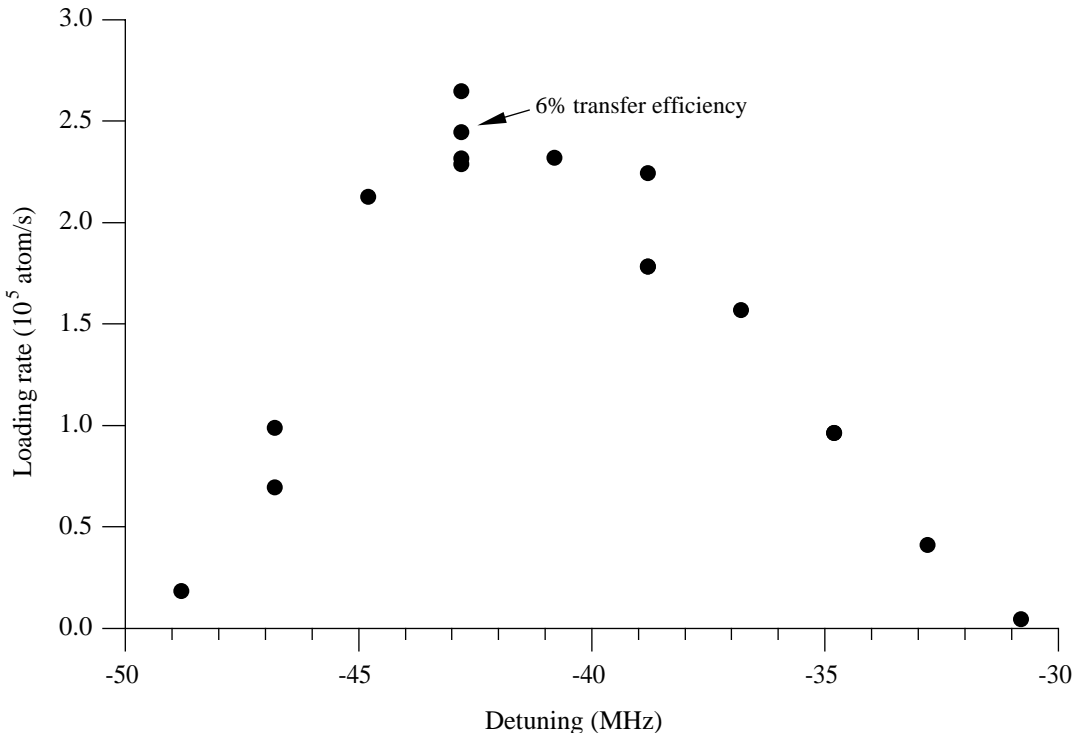


FIGURE 5.8: Loading rate of ^{39}K atoms into the MOT from a room-temperature vapor-loaded funnel. The efficiency, the ratio of the main MOT loading rate over the funnel loading rate (hole plugged) is about 6% peak. For these initial experiments, the funnel loads from a room-temperature reservoir of potassium (described in more detail in the text).

transport distance from funnel apex to MOT is 35 cm. We load the funnel from a room-temperature reservoir of potassium metal through a 15 cm long, 1.7 cm diameter stainless steel tube.

Both the funnel and MOT are operated using the same $\text{Ti:Al}_2\text{O}_3$ laser and AOM, with detuning Δ ; here Δ is the detuning from the $P_{3/2} F' = 3$ level of ^{39}K [Williamson III and Walker, 1995]. We have found that the trap/funnel combination works over the same detuning range of a MOT alone, and we found best operation at approximately $\Delta = -43$ MHz, as shown in Figure 5.8. The main MOT was operated at a total intensity (all six beams) of $I_{\text{tot}} = 90 \text{ mW/cm}^2$ (beam waist $w_0 = 2.8$ cm), with $dB/dz = 5 \text{ G/cm}$, and the funnel was operated from a single beam of $I_0 = 13 \text{ mW/cm}^2$ ($w_0 = 3$ cm), $dB/dz = 4 \text{ G/cm}$. The magnetic field of the funnel was carefully shimmed, and optimum operation resulted for $B = 0$ right near the apex.

The pyramid, operating as a trap, is known to have a loading efficiency comparable

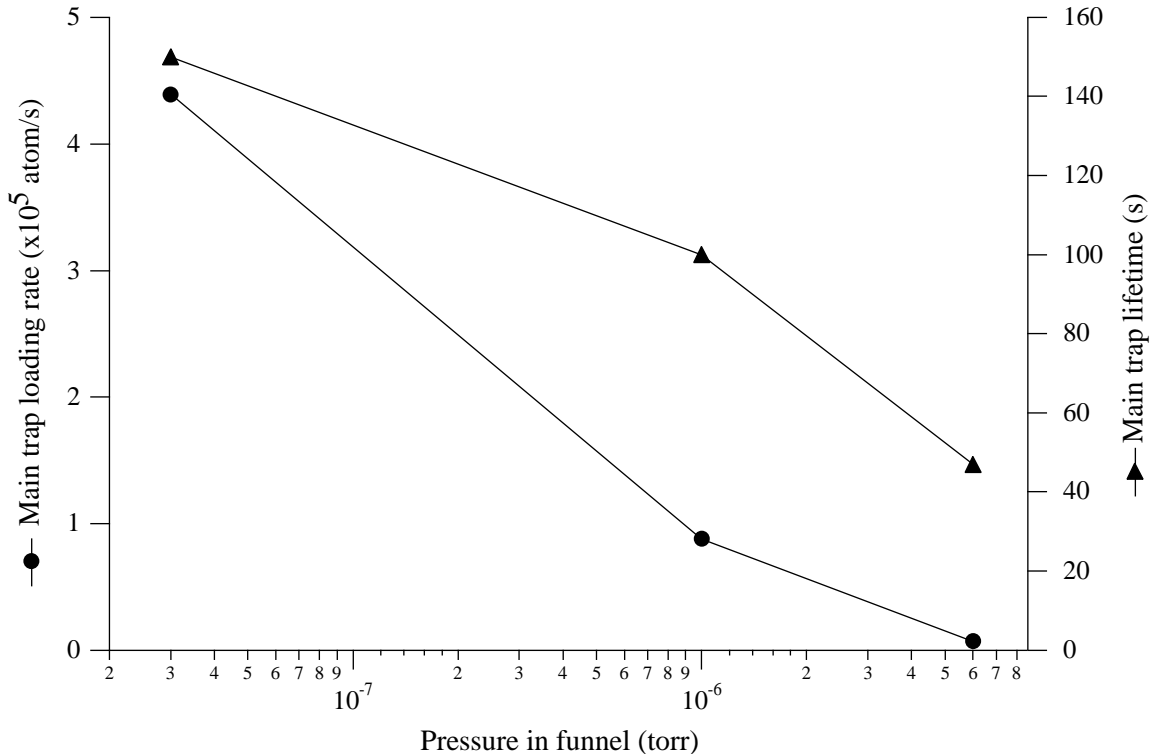


FIGURE 5.9: Main trap loading rate and lifetime at various funnel pressures. The main trap is loaded from the funnel, whose pressure is raised by deliberately introducing H_2 . Note that the main trap still has a substantial loading rate and a long lifetime even for 10^{-6} torr H_2 in the funnel.

to a standard MOT [Lee et al., 1996; Kim et al., 1997]. A key issue in determining the usefulness of this scheme is the efficiency of transferring atoms from the funnel to the MOT. We determine this by comparing the loading rate of atoms into the MOT to the loading rate of atoms into the funnel. These rates were deduced by measuring the fluorescence from the trapped atoms over time as the atoms loaded into an empty trap.

To determine the loading rate into the funnel, we make the funnel into a MOT by retroreflecting the laser beam emerging from the hole in the funnel apex using a mirror and quarter-wave plate at the other end of the large vacuum chamber. It is also necessary to shim the magnetic field slightly until a uniform ball of atoms forms in the funnel. Then operating the system as a funnel/trap combination, we measure the loading rate into the main trap, and the ratio of the two rates gives the transfer efficiency, which peaked at 6%, as shown in Figure 5.8.

A essential property of the funnel is the ability to operate at a high background pressure, much higher than a MOT can tolerate. The number of atoms a MOT can accumulate is inversely proportional to the density of the background gas. At pressures of $> 10^{-8}$ torr, the number of atoms one can trap falls off sharply, as the pressure-limited trap loss rate $\gamma > 1 \text{ s}^{-1}$. Since the funnel ejects the atoms once they are cool, the relevant time constant is the damping time required to cool the atoms from the capture velocity v_c to typical MOT velocities. This time is typically a few milliseconds, which roughly corresponds to 10^{-6} torr.

The low conductance of the apex hole allows a large pressure drop to the MOT chamber. We successfully ran the funnel at pressures of 10^{-6} torr H_2 (instead of our usual $\sim 10^{-9}$ torr) while only reducing the loading rate by a factor of five; at $6 \cdot 10^{-6}$ torr the loading rate dropped an additional factor of ten. At these high pressures the main MOT lifetime was reduced by only a factor of two. These data are summarized in Figure 5.9.

5.6 Summary

We have demonstrated the transfer of potassium atoms from a magneto-optical funnel (a hollow pyramidal mirror) through a 0.05 l/s conductance hole and into a conventional magneto-optical trap (MOT) 35 cm away, with an efficiency of approximately six percent; this technique should be useful for any experiment requiring high loading rates with minimal contamination from hot untrapped atoms. We suspect the transfer efficiency is limited mostly by imperfections in the mirror construction.

In the next chapter we will discuss the extension of this simple scheme by implementing the wall coating techniques for vapor cell loading. Dryfilm coated cell total capture efficiencies approaching 10% have been demonstrated [Stephens et al., 1994], and by improving the quality of the mirrors used, it should in principle be possible to load atoms from a thermal vapor into a MOT with an efficiency approaching unity. Loading rates corresponding to direct capture from an atomic vapor of 10^{-7} torr should be possible in a $< 10^{-10}$ torr UHV MOT.

Chapter 6

Radioactive Isotopes of Potassium

6.1 Introduction

The two-stage, efficient system we have thus far described, consisting of a magneto-optical trap loaded from a magneto-optical funnel, is potentially an ideal laboratory in which to perform precision beta-decay experiments. The sample of atoms is spatially confined, free from perturbing interactions, and well-isolated from sources of radioactive background. Furthermore, the nuclei can be readily and completely spin-polarized by optically pumping the electronic states. This allows us to make a high-precision measurement of the asymmetry in the distribution of decaying beta particles. This measurement provides a precision test of the Standard Model; specifically it sets a limit on the mass of the right-handed vector boson*. With large, well-known sample polarization and precision limited only by systematic errors, we expect to make a measurement of the asymmetry parameter A in ^{38}K to better than 1%, which is both competitive with current experiments and approaches the level of known recoil and higher-order corrections in this nucleus.

Currently there are five other groups trapping or attempting to trap radioactive isotopes, all with the intention of performing low-energy tests of the Standard Model. The group at Berkeley has trapped ^{21}Na [Lu et al., 1994] with the intention of performing β -asymmetry measurements; Stony Brook's group has trapped ^{79}Rb [Gwinner et al., 1994] and ^{210}Fr [Simsarian et al., 1996a,b; Zhao et al., 1997] with the long-term intention of performing atomic parity-non-conservation experiments; a collaboration

*A recent review of symmetry tests and weak interactions appears in Deutsch and Quin [1995].

between LBNL and JILA has trapped ^{221}Fr [Lu et al., 1997]; the large collaboration at TRIUMF has trapped ^{37}K and $^{38}\text{K}^m$ [Behr et al., 1997]; and a collaboration between Los Alamos National Labs and LBNL is attempting to trap radioactive cesium.

This chapter begins by presenting some background material on beta-asymmetry measurements (§6.2). We then describe some of the unique features which distinguish the atomic structure of the radioactive isotopes of potassium from the naturally occurring ones (§6.3), as well as our observations of ^{40}K in the beam-loaded trap described in chapter 4. Then we discuss our design for creating radioactive ^{37}K and ^{38}K with the tandem accelerator, including a description of the target (§6.4.1), transport system (§6.4.2), vacuum system (§6.4.3), and optics (§6.4.4). Finally, in section 6.5 we analyze the overall efficiency of the system, from target to trap, and discuss the results we obtained in our tests with ^{39}K and ^{40}K .

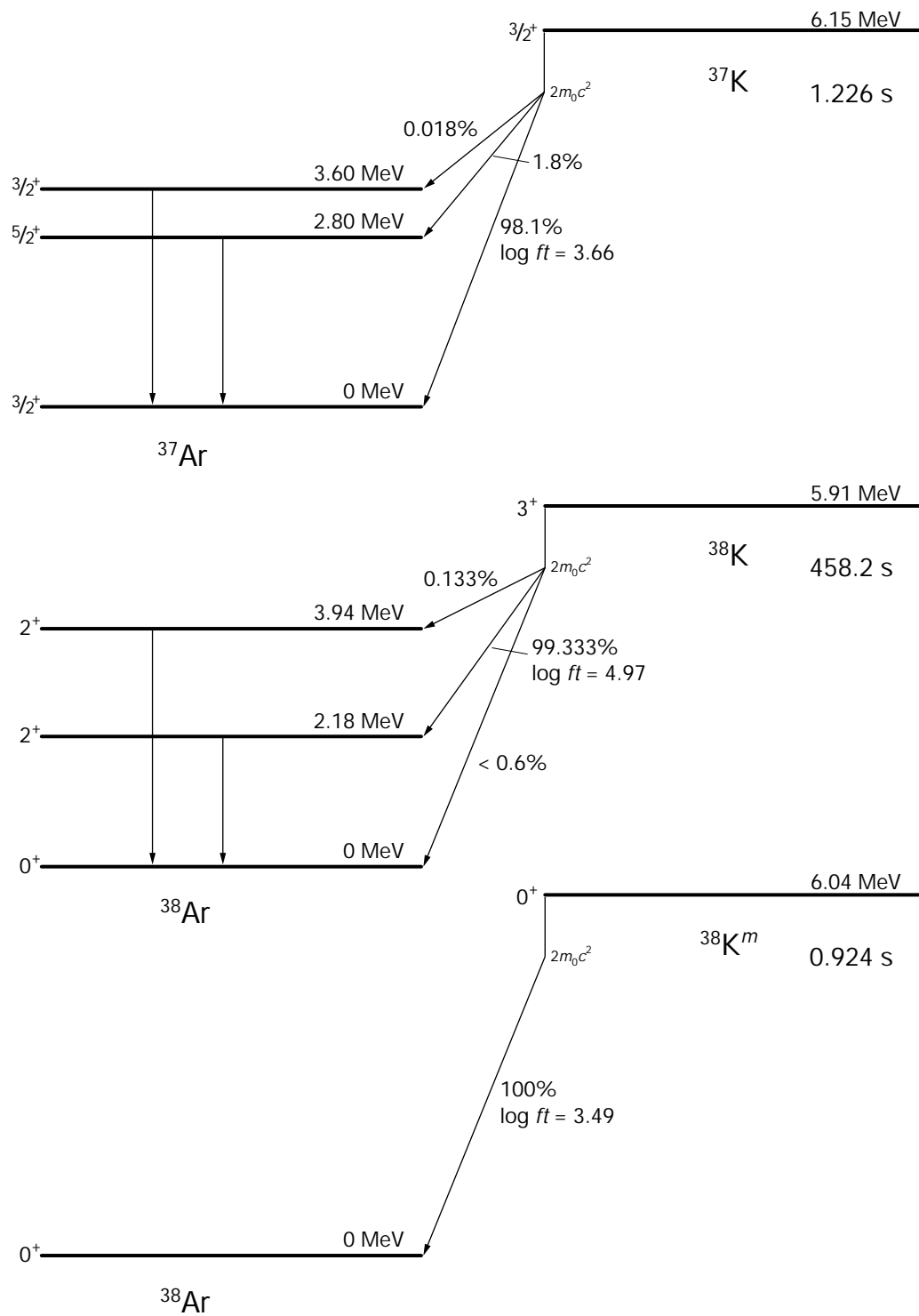
6.2 Background

The Standard Model of weak interactions, now a cornerstone of modern particle physics, has been tested extensively at high energies using large accelerators that make measurements on bare nucleons directly accessible. However, on the low-energy end, within the confines of the atomic nucleus, we can also perform valuable tests of the standard model by making precision beta-decay measurements [Commins and Bucksbaum, 1983; Holstein, 1989]. One example is that the comparative half-lives (or ft values) of superallowed, pure Fermi transitions ($I^\pi = 0^+ \rightarrow 0^+$) can be used to determine the Cabbibo quark mixing angle θ_C , because these transitions contain no contributions from axial vector currents. Similarly, asymmetry measurements in the decay of mirror nuclei, which are mixed Fermi/Gamov-Teller transitions, used in combination with ft values, can detect deviations from the Standard Model.

For the experiment at hand, we are interested in the beta decay of ^{37}K and ^{38}K , shown in Figure 6.1. Note that ^{37}K , a mirror nucleus with $I^\pi = 3/2^+ \rightarrow 3/2^+$, decays almost completely to the ground state, while ^{38}K decays to an excited state with an associated γ -ray.

The form of the angular distribution of the decaying betas is given by simple dynamics as

$$W(\theta) = W_0 \left(1 + \frac{v}{c} PA \cos \theta \right), \quad (6.1)$$

FIGURE 6.1: Nuclear β -decay scheme for three potassium nuclei.

where v is the β velocity, P is the polarization of the nuclear spin, and A is the asymmetry parameter. By measuring the distribution W , the β energy (v), and the polarization P , we can determine the asymmetry parameter A .

Our prime candidate nuclear process is $^{38}\text{K}(I = 3^+) \rightarrow ^{38}\text{Ar}(I = 2^+)$, which is a pure Gamov-Teller transition. In the “manifest left-right symmetric” formulation, deviations from the Standard Model predictions are explicitly characterized in terms of vector boson masses. The expression for the β -asymmetry parameter is modified from the Standard Model prediction by

$$A = A_{\text{SM}} \left[1 - 2 \left(\frac{m_L}{m_R} \right)^4 \right], \quad (6.2)$$

where A_{SM} is the asymmetry parameter predicted by the standard model with no right-handed vector bosons, and m_L and m_R are the left- and right-handed vector boson masses. In other words, if the Standard Model is entirely correct, we expect to see no deviation of A from A_{SM} . Note that for this decay A_{SM} happens to be exactly 1 because it is a pure Gamov-Teller transition with $\Delta I = 1$.

The decay of ^{37}K is also quite interesting in that it is a mirror decay, making it a superallowed transition. Measurements of its asymmetry parameter test the conserved vector current hypothesis, but because it is a mixed decay (containing both vector and axial vector matrix elements) this also requires some other parameter be measured with high precision, usually the ft value. The fact that the decay of ^{37}K is a mirror transition is appealing because recoil-order effects cancel exactly, whereas in ^{38}K , they are small but nonzero (current theory estimates places the corrections at 0.25%).[†] Currently our target yields (discussed in §6.5.1) give us the option only of trapping ^{38}K , however we suspect that some modifications may give us access to usable amounts of ^{37}K as well.

To determine the improvement over conventional beta-decay experiments that our technique should be able to achieve, we refer again to the distribution in equation 6.1. The product $(v/c)PA \cos \theta$ is our *observed* asymmetry, which we call \mathcal{A} , and is usually contains an average over the β spectrum and some finite detector solid angle. If we measure the number of betas emitted parallel and antiparallel to the nuclear polarization direction, the average beta energy, and the spin polarization, we measure it

[†]Personal communication, P. A. Quin.

as

$$\mathcal{A} = \langle \beta \rangle P A \langle \cos \theta \rangle = \frac{N_+ - N_-}{N_+ + N_-}. \quad (6.3)$$

The signal-to-noise ratio in \mathcal{A} , limited by statistics, is given by [Voytas, 1993]

$$\frac{\mathcal{A}}{\sigma_{\mathcal{A}}} = \sqrt{\frac{\mathcal{A}^2}{1 - \mathcal{A}^2} N}, \quad (6.4)$$

where $N = N_+ + N_-$.

Combining this result to get the total uncertainty in the asymmetry parameter A , we find

$$\frac{\sigma_A}{A} = \sqrt{\frac{1 - \mathcal{A}^2}{\mathcal{A}^2 N} + \sum_{\xi} \left(\frac{\sigma_{\xi}}{\xi} \right)^2} \quad (6.5)$$

where σ_{ξ} represents systematic errors in $\xi = \langle \beta \rangle, \langle \cos \theta \rangle, \text{ or } P$. For our experiment using ^{38}K , with roughly 1% detector solid angle and a β energy endpoint of 2.7 MeV, and nearly 100% polarization, the first term under the root is roughly $0.6/N$. For a “typical” nuclear experiment with $P \approx 5\%$, that term is $400/N$. Thus our experiment is limited only by systematics, and expect to achieve our desired precision of 1% with only about 6000 total events; the equivalent traditional approach would require $4 \cdot 10^6$ events. With roughly 10 000 atoms in the trap we should have a detected β event rate of nearly 1 Hz, and a precision measurement could be completed in only a few hours’ worth of counting.

A similar analysis applies to ^{37}K , but because of the higher β endpoint energy, $\langle \beta \rangle$ is larger, and the first term in equation 6.5 is about $0.1/N$. Furthermore, in traditional experiments the nuclear polarization would have to be analyzed using the weak 2% γ branch, requiring roughly fifty times the number of events. Thus to get 1% statistics in A for ^{37}K with our approach would take ~ 1000 events; conventional methods would require $2 \cdot 10^8$ events! We easily reach the limit imposed by systematic errors, not possible with traditional approaches to asymmetry measurements.

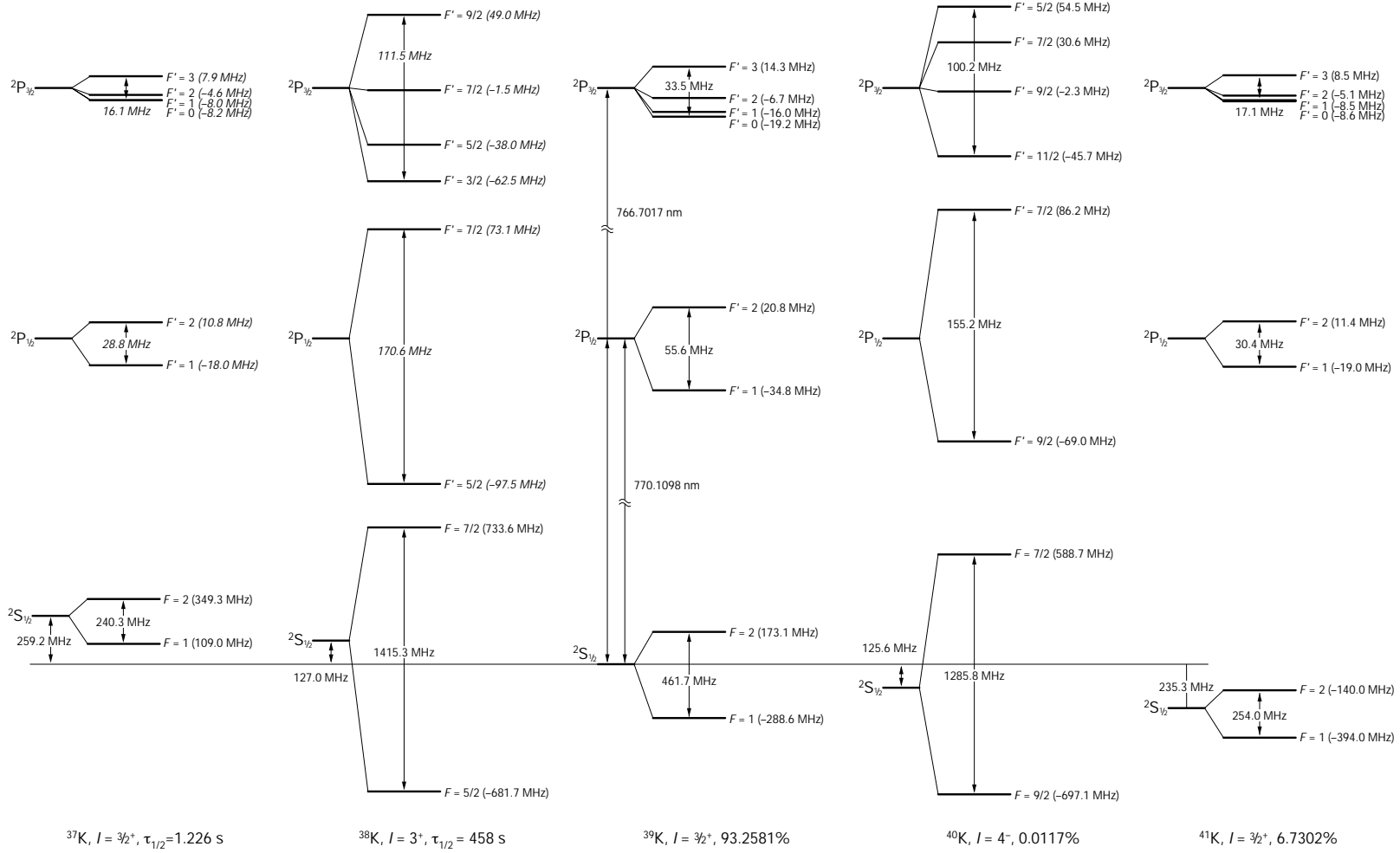


FIGURE 6.2: Energies of $^{37-41}\text{K}$ hyperfine levels in the $4^2S_{1/2}$, $4^2P_{1/2}$, and $4^2P_{3/2}$ terms. Adapted from Arimondo et al. [1977]; Bendali et al. [1981]; Touchard et al. [1982]; Besch et al. [1968]. Italicized values have not been measured and are inferred from the other isotopes and in the $P_{3/2}$ terms we assume $B = 3.7$ MHz.

6.3 Radioactive potassium

6.3.1 Hyperfine structure

In the previous section we briefly discussed how the nuclear properties and decay schemes (Figure 6.1) influence the nuclear measurements we wish to perform. But we also must be able to optically trap the radioactive isotopes. A variety of factors influence the “trappability,” or efficiency with which one can capture and confine a particular alkali species. Of course the excited-state lifetime and saturation intensity are of primary importance, but there is only a little variation in these across the alkalis, and none between isotopes. Even the oscillator strengths don’t vary much from isotope to isotope. But the size of the hyperfine structure, as evidenced in Figure 6.2, varies greatly between the isotopes because of their different nuclear spins and moments and can have a profound effect on the trapping properties.

Figure 6.2 shows the hyperfine structure of the five potassium isotopes we are interesting in trapping. Isotopes $^{39-41}\text{K}$ are all naturally occurring, ^{39}K and ^{41}K are stable and abundant (93.3% and 6.7%, respectively), and ^{40}K is radioactive with a half-life of $1.28 \cdot 10^9$ years and abundance 0.01% (we will discuss trapping of ^{40}K in §6.3.3). Potassium-37 and -38, as we have discussed above, are the isotopes we will create with our accelerator and target system, and are interesting for precision β -decay measurements.

Note that in this figure we have not included the hyperfine structure of $^{38}\text{K}^m$, a metastable nuclear state with a 0.9 s lifetime. It has no hyperfine structure due to having $I = 0$, and is also an interesting atom for studying the weak interaction (see the nuclear decay diagram in Figure 6.1). However, we will not discuss this atom in any detail within the scope of this dissertation. The group at TRIUMF has magneto-optically trapped this isotope, as well as ^{37}K , to perform $\beta - \nu$ correlation experiments, also of interest in studying the weak interaction [Behr et al., 1997].

Noting the patterns evident in Figure 6.2, we see that the odd- A isotopes $^{37,39,41}\text{K}$ with $I = 3/2^+$ have nearly identical excited-state hyperfine structure, with very closely spaced excited-state levels. Recall from chapter 2 that we trap the natural isotopes ^{39}K and ^{41}K by detuning both trapping laser frequencies below the entire hyperfine structure. As discussed in §2.2 and evidenced by Figure 2.2, the upper levels act together as a whole to enhance the capture velocity range. The natural linewidth of 6.2 MHz combined with considerable power-broadening when $I \gg I_s$ merges the

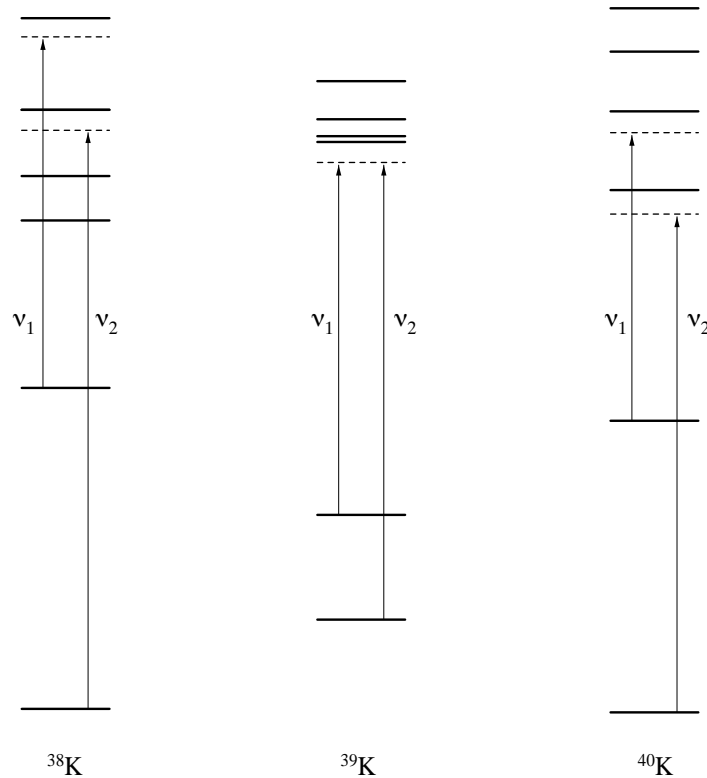


FIGURE 6.3: Three different laser tuning schemes used for trapping $^{37-41}\text{K}$, showing only the two $S_{1/2}$ and four $P_{3/2}$ levels. In the center, the scheme for ^{39}K (also used for ^{41}K and ^{37}K) detunes both lasers to the same “virtual level” below the entire hyperfine structure, as described in §2.2. On the left is ^{38}K tuned as in a sodium “Type I” trap with each laser tuned to its own level.

oscillator strengths of the upper levels so they act together as one broad line.

Potassium-41 and -37, with slightly smaller structure than ^{39}K , have somewhat smaller capture velocities. Our loading rate measurements of ^{41}K in both the beam and vapor-loaded systems act as an ideal testing ground for determining the efficiency of the system for ^{37}K .

On the other hand, the even- A isotopes ^{38}K and ^{40}K , with large nuclear spins of 3^+ and 4^- respectively, show well-spaced excited-state hyperfine levels. Their wide spacing cannot be overcome even with severe power-broadening, and thus we must trap these isotopes in a slightly different fashion. In fact, ^{40}K is highly unusual, having “inverted” hyperfine structure because of its negative dipole and quadrupole moments. Lithium, too, has inverted hyperfine structure, but is tiny and unresolved, having much different trapping characteristics [Lin et al., 1991].

In Figure 6.3 we show the tuning scheme used or proposed for three of our five isotopes; diagrams for ^{37}K and ^{41}K are not explicitly shown since the scheme we use is identical to ^{39}K . In the center we show the scheme used for ^{39}K , and on the right we show the scheme used to trap ^{40}K . Each laser is tuned near a separate level, and detuned a few linewidths away. Unlike trapping rubidium or cesium, both lasers are detuned and have roughly equal amounts of power. In rubidium or cesium, with large, well-resolved hyperfine levels, a single laser provides the trapping force, and a small amount of light is used to optically pump the atom, removing its dark state. We will discuss the trapping of ^{40}K later in §6.3.3.

On the left in Figure 6.3 we show one proposed detuning for ^{38}K ; this is just one possible scheme, since we have yet to trap this isotope. As we will discuss in the next section, there are other possibilities that may work better. The scheme shown in this figure corresponds to the way a sodium “type I” MOT is constructed [Raab et al., 1987]. The hyperfine spacings are nearly identical to sodium, so this scheme seems the most likely to work. As in sodium and the odd- A potassium isotopes, we share the laser power roughly evenly between both colors. One problem with using this detuning scheme, however, is that atoms traveling at high velocities will see blue-detuned light from the $1 \rightarrow 1'$ transition, heating the atoms and placing a hard limit on the capture velocity. In the next section we will describe one possible means of overcoming this limitation.

6.3.2 Zeeman structure

By only considering the hyperfine structure, we overlook the important interaction between the light polarization and Zeeman levels that is responsible for the confining force. Without this, we would not be able to produce a trap.

The shift of the Zeeman sublevels of an alkali atom in a magnetic field is given by the well-known formula

$$\Delta E_Z = g_F \mu_B J_z B m_F. \quad (6.6)$$

In Figure 6.4 we tabulate the Landé g -factors needed for the the three nuclear spins of our five isotopes, and in Figure 6.5 we show the splittings given by equation 6.6 for $^{38-41}\text{K}$. Here we plot the location of each m_F level for the $S_{1/2}$ and $P_{3/2}$ levels at a static magnetic field of $B = 10\text{ G}$. The “slope” formed by each set of sublevels is of course given by the g -factor, and provides a graphical guide to understanding the

I	J	F	g_F
$\frac{3}{2}$	$\frac{1}{2}$	1	-1/2
		2	+1/2
	$\frac{3}{2}$	0	—
		1, 2, 3	+2/3
3	$\frac{1}{2}$	5/2	-2/7
		7/2	+2/7
	$\frac{3}{2}$	3/2	-4/5
		5/2	+4/105
		7/2	+20/63
		9/2	+4/9
4	$\frac{1}{2}$	7/2	-1/9
		9/2	+1/9
	$\frac{3}{2}$	5/2	-4/7
		7/2	-4/189
		9/2	+68/297
		11/2	+4/11

FIGURE 6.4: Table of Landé g -factors for $^{37-41}\text{K}$, used to calculate levels in Figure 6.2

interaction of light polarization and level splittings, as we shall see. The second-order Zeeman effect, which has a strong effect on the locations of the outermost m_F levels in order to avoid crossing with adjacent levels, has been ignored here. Despite this, this picture still acts as an instructive guide to understanding MOT operation.

The difference in the g -factors between pairs of levels (or, graphically, looking carefully at the slopes in Figure 6.5) gives a rough idea of the strength of the MOT confining force. Consider illuminating ^{39}K with σ^+ light, driving transitions with $m'_F = m_F + 1$. In the MOT at a particular magnetic field (e.g., 10 G as in Figure 6.5), this puts a force on the atom proportional to $\zeta = m'_F g'_F - m_F g_F$. If $\zeta > 0$ this pushes the atom towards smaller magnetic fields, and if $\zeta < 0$, pushes it towards larger field. Graphically, consider ^{39}K in Figure 6.5: the difference in the slope of all four upper levels is greater than the slope of either lower level. Furthermore, the slope difference is greater for the lower $F = 1$ state than for the $F = 2$ state, and we would thus expect the trapping force to be stronger for the $1 \rightarrow 1'$ transition than for $2 \rightarrow 1'$.

We see that this argument is also true for ^{41}K . In ^{41}K , all the upper state “slopes” are greater than those of the two lower states, and thus the two trapping laser frequencies should be σ^+ in order to push the atoms towards lower field. Note that

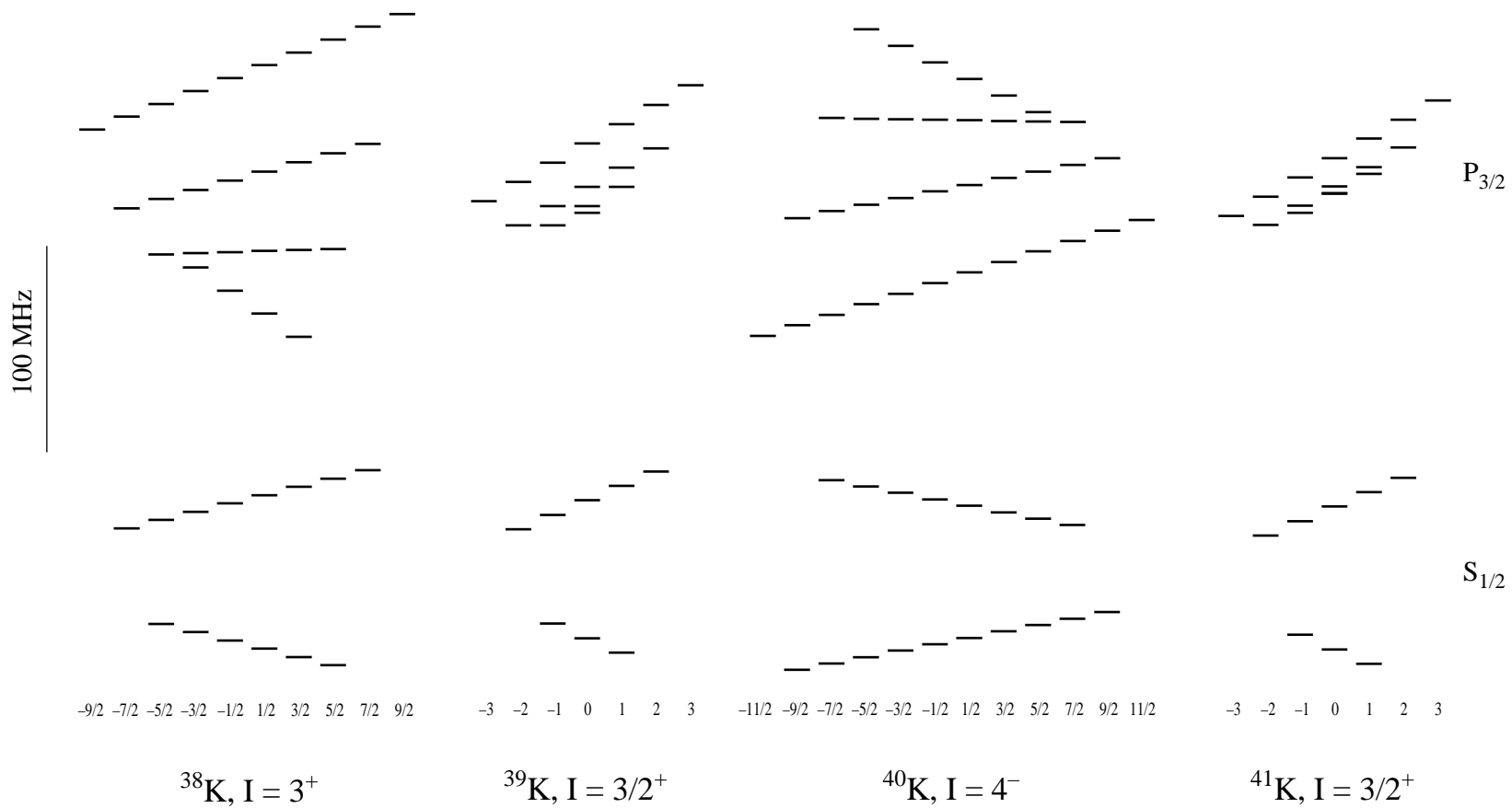


FIGURE 6.5: Zeeman sublevels of $P_{3/2}$ and $S_{1/2}$ levels of potassium isotopes at $B = 10$ G. Hyperfine structure of $S_{1/2}$ levels and gross structure is not to scale. ^{37}K is not shown explicitly because it's structure is nearly identical to ^{41}K (see Figure 6.2).

potassium-37 is not shown in Figure 6.5 but has a hyperfine and Zeeman level structure almost identical to ^{41}K and is trapped in a completely analogous manner.

Now consider ^{38}K and ^{40}K , where g_F for the excited-states changes sign and therefore ζ changes sign. This is not so serious in ^{40}K because the hyperfine structure is inverted, and we still trap by tuning the lowest-energy F' levels, $7/2$ and $9/2$, both with $\zeta > 0$. And if we try trapping ^{38}K as outlined in the previous section (a sodium “type I” trap), this is also the case. But this method has not yet worked for us, and we know also that there is a hard limit on the maximum capture velocity imposed by heating from the two lowermost excited state levels ($F' = 3/2, 5/2$).

A promising scheme we have not yet tried is to tune one laser below the $F = 7/2$ to $F' = 9/2$ transition, and the other below the $F = 5/2$ to $F' = 3/2$ transition. Our six-level model seems to indicate this approach has a moderate capture velocity similar to ^{40}K and no strict limit like the sodium “type I” detuning scheme. However, referring again to Figure 6.5, note that the lower transition has $\zeta < 0$ and the upper one, $\zeta > 0$, meaning that each color will need opposite circular polarization. This also happens to be the approach used by Flemming et al. [1997] to trap sodium using the D_1 transition. However, they do not directly discuss loading rates, so we cannot easily use their data to predict the performance of this scheme in potassium.

6.3.3 Trapping of ^{40}K

Here we briefly discuss the results we obtained using the effusive beam-loaded trap described in chapter 4 to trap ^{40}K ; in section 6.6. By switching the hyperfine AOM and tuning the frequencies to the $F = 9/2 \rightarrow 11/2'$ and $F = 7/2 \rightarrow 9/2'$ transitions, we were able to successfully load the MOT with about 400 atoms from an extremely feeble beam of only $2.8 \cdot 10^5$ ^{40}K atom/s. Figure 6.6 shows the loading rate, using transverse collimation, as a function of detuning, peaking at about 2 atom/s for a detuning of -80 MHz. Loading was observed over a range of about 20 MHz, slightly narrower than the 30 MHz range observed in ^{39}K (see Figure 4.6).

The peak loading rate corresponds to a total efficiency $\eta_{\text{tot}} = 7 \cdot 10^{-6}$, considerably smaller than the $\eta_{\text{tot}} = 5 \cdot 10^{-5}$ obtained for ^{39}K under similar conditions. This implies a lower capture velocity for ^{40}K which one would expect based on the fact that the trapping is done using individual levels rather than an entire manifold. This fact is also borne out in force versus velocity graphs for ^{40}K done using our model (§2.4). We

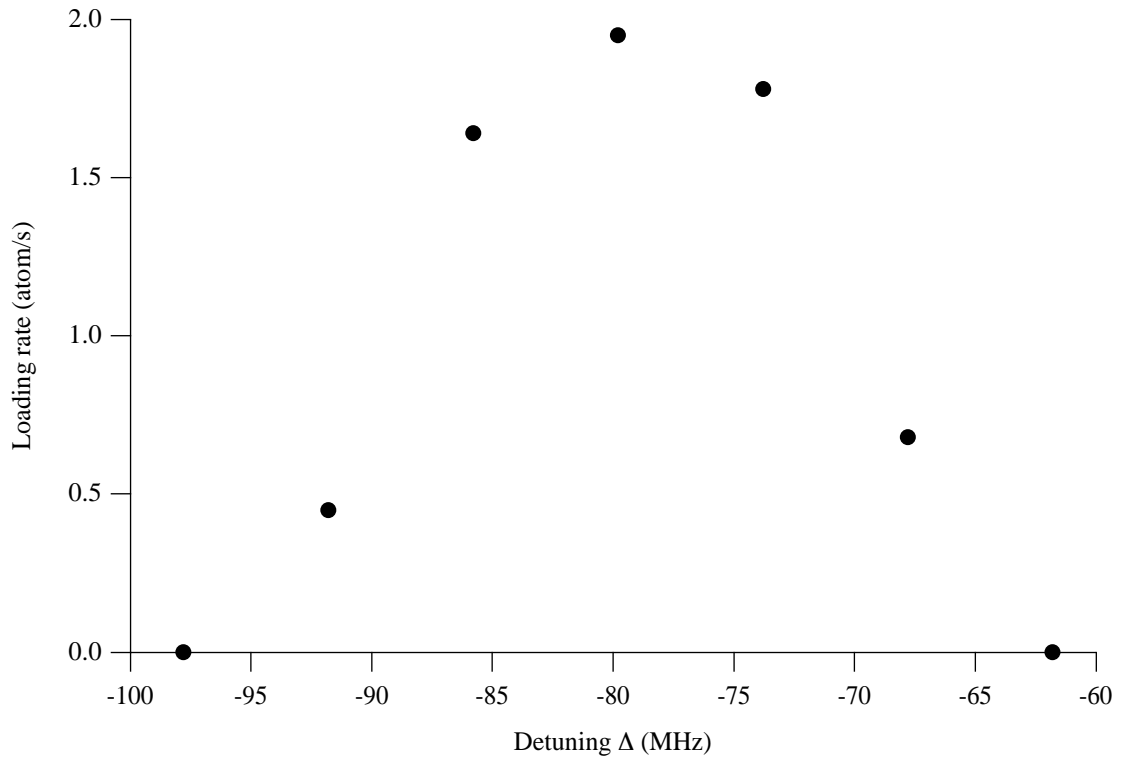


FIGURE 6.6: Loading rate of ^{40}K into trap loaded from an effusive beam. Atomic beam collimation on with $I_{\text{col}} = 276 \text{ mW/cm}^2$. Trapping beam intensity $I_{\text{tot}} = 108 \text{ mW}$, quadrupole field gradient $dB/dz = 15 \text{ G/cm}$.

will return to discussing ^{40}K trapping using our atomic funnel and target system in section 6.6.

6.4 System description

6.4.1 Target

Creating a short-lived radioactive beam of alkalis in a UHV or near-UHV environment places demands on all aspects of the target. We must effectively utilize the capabilities of the accelerator facilities to create enough radioactive material to trap. The produced alkali isotope must be able to escape the target region into free space quickly and in a manner which allows us to accumulate and manipulate them. The target materials must not outgas rapidly or have high vapor pressures. The target material must be robust enough not to degrade too quickly under bombardment, and must not create unacceptable backgrounds.

The University of Wisconsin's tandem electrostatic accelerator is capable of producing beams of protons, deuterons, ^4He , and some light nuclei (lithium, for example). Protons and deuterons can be accelerated up to an energy of 12 MeV, others more. With these facilities, we have determined that the most efficient, accessible production mechanism for ^{38}K is $^{40}\text{Ca}(d, \alpha)^{38}\text{K}$, and for ^{37}K , $^{40}\text{Ca}(p, \alpha)^{37}\text{K}$. The Q -value for the ^{37}K reaction is -5.18 MeV [McNally, 1966] and for ^{38}K it is $+4.67$ MeV. At 12 MeV beam energies, both of these reactions should progress readily.

Our design was inspired by the early work of Ames et al. [1965], who created an effusive beam of Na^{21} (lifetime 23 s) using an 18 MeV beam of protons on natural magnesium-40, using the Princeton cyclotron. A schematic of his oven design is shown in Figure 6.7. A fine powder of magnesium (explosive!) was placed in a stainless steel block with holes drilled for heaters, and a foil placed over the entrance to allow the proton beam to enter. The oven was heated to 450°C (melting point of Mg is 651°C) to keep the radioactive sodium in the vapor phase and to encourage it to diffuse out of the magnesium. The output of the oven was collected on a copper flag and moved to a region where the decays were counted and further experiments performed.

Although quite novel and functional, we need to make a number of changes and improvements in this design to work in our environment. Obviously we need to use calcium instead of magnesium to make potassium rather than sodium. Then by sub-

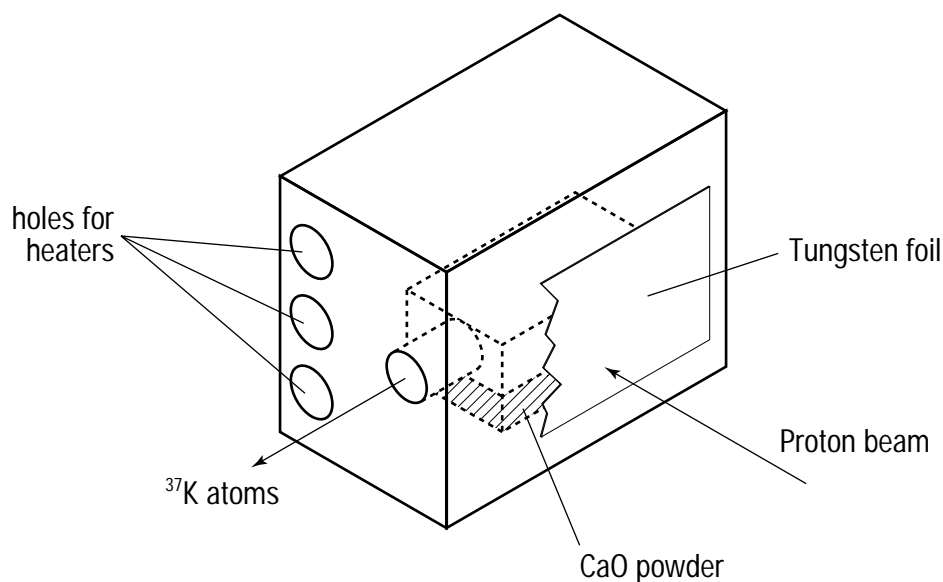


FIGURE 6.7: Original oven design of Ames et al. [1965], used on the Princeton cyclotron. The entire block is heated by inserted cartridge heaters to about 900°C . The cyclotron beam passes through the tungsten foil, hitting the magnesium powder and producing Na^{21} , which diffuses out of the powder and through the beam outlet.

stituting calcium oxide instead of calcium metal, we make two simultaneous improvements. First, the melting point of CaO is 2614°C , much higher than calcium metal (839°C), reducing its vapor pressure to nearly insignificant levels. The Ames design produced a significant amount of magnesium vapor, at pressures that would interfere with the operation of our funnel. Second, CaO is much easier to work with than the highly reactive metallic form; it can be handled in open air, and it comes in a variety of particle sizes or can be easily ground to a specified size.

We can make a simple estimate of the optimal particle size, based on a balance between the time it takes for the newly-made potassium to diffuse out of an individual CaO particle and the time it takes for the potassium to travel from where it was made in the bulk powder to the surface. If the particles are too small, the atoms will spend too much time bouncing between particles and not getting out of the powder, and if the particles are too big, they will spend all of their time diffusing out of the bulk CaO .

Let's call the average diameter of a CaO particle d and the distance from where the reaction occurs to the surface of the powder l . The time it takes the potassium to

become free is

$$t_{\text{free}} = \frac{d^2}{D} + \frac{l^2}{d\alpha}, \quad (6.7)$$

where D is the diffusion constant for K in CaO, and α is the most probable thermal velocity of hot K. The first term results from a solution to the diffusion equation and the second term is the solution to a random walk between particles. We want to minimize t_{free} with respect to the particle diameter d :

$$\frac{\partial t_{\text{free}}}{\partial d} = \frac{2d}{D} - \frac{l^2}{d^2\alpha} = 0. \quad (6.8)$$

This is satisfied by

$$d = \left(\frac{Dl^2}{2\alpha} \right)^{1/3}. \quad (6.9)$$

For typical values $D \approx 10^{-5} \text{ cm}^2/\text{s}$, $\alpha \approx 10^5 \text{ cm/s}$, and $l \approx 0.3 \text{ cm}$, we find that $d \approx 2 \mu\text{m}$. Based on this calculation and some additional testing, we decided to use 3–5 μm diameter CaO particles.

Figure 6.8 is a scale schematic of the entire target to which we will refer often in the rest of this section. The CaO powder is held in a tantalum backed cup, formed by wrapping and spot welding a small sheet of tantalum foil around a stainless steel cylinder 1.7 cm in diameter. The cylinder is cut at an oblique angle (7°) both to keep the powder fairly level and to spread the incoming proton beam over the surface of the powder, which is 2 mm thick in its holder. The choice of tantalum is multi-faceted: it can withstand high temperature; as a pure material, it contains very little embedded hydrogen; and its high Z ensures that it stops the proton beam before it hits the stainless steel. (Stainless steel contains many elements and irradiating it produces a plethora of radioactive compounds.)

This holder is mounted to a stainless steel L -bracket held on a conflat flange. Between the tantalum/steel holder is inserted a ceramic washer and a small loop of coaxial heater wire[‡] that can provide additional target heating to enhance diffusion out of the target. The ceramic washer provides electrical isolation, allowing us to measure the total amount of beam current deposited on the target. In addition, at the end of the bracket is a small rectangle of tantalum with a small hole near the center, electrically isolated from the bracket. The deuteron beam passes through the

[‡]Thermocoax, Philips Industrial Automation.

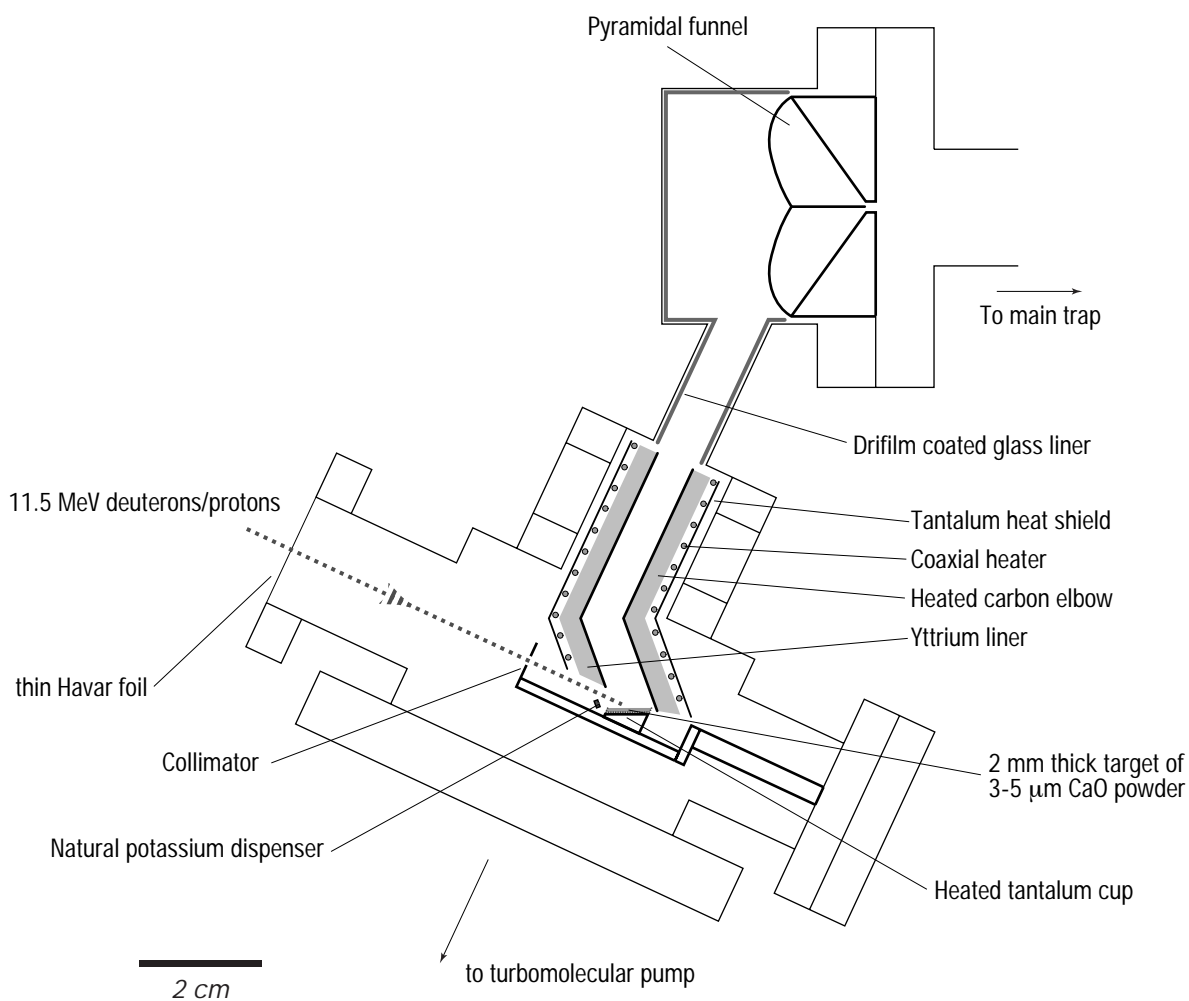


FIGURE 6.8: Schematic of the Wisconsin target system. Protons or deuterons of 11.5 MeV from the UW tandem impinge on a CaO powder with particle size 3-5 μm , which is 2 mm thick overall and backed by tantalum foil to stop the p^+/d^+ beam. The radioactive potassium isotopes, produced in the powder by either $^{40}\text{Ca}(p, \alpha)^{37}\text{K}$ or $^{40}\text{Ca}(d, \alpha)^{38}\text{K}$, diffuse out and bounce on the hot (roughly 900 $^{\circ}\text{C}$) yttrium tube, moving towards the pyramidal funnel. The funnel and cell walls are lined with dryfilm-coated glass. A thin 2.5 μm Havar foil separates our turbo-pumped target vacuum from the tandem vacuum. For testing, a small dispenser of natural potassium is located near the target.

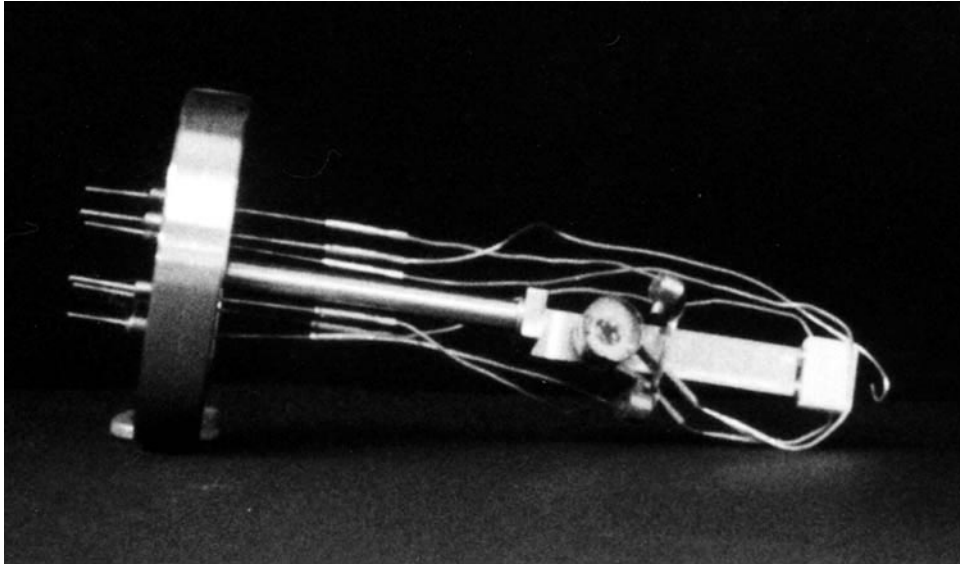


FIGURE 6.9: Photo of target flange assembly.

hole, and the beam current measured from the isolated tantalum provides a means of determining beam collimation and steering.

The target holder assembly also carries a natural potassium metal dispenser, consisting of a potassium salt that is reduced by hydrogen released by a SAES-type St101 getter.[§] When the getter is heated to roughly 500°C by passing a current through it, it releases the potassium from the matrix. The amount of material emanating from the dispenser is notoriously difficult to calculate, with an exponential dependence on current and a poorly known threshold. Nevertheless, the dispenser holds a total of about 3 mg of material and can emit it at the rate of a few $\mu\text{g/h}$. We use this to test the operation of the whole transport system as well as to “cure” the dryfilm (discussed in Appendix C).

Figure 6.9 is an actual photograph of the target flange assembly. To the left is the 2-3/4" flange and electrical feedthroughs. Provided are connections to the target heater, potassium dispenser, collimator current, and target current. All connections are UHV compatible, using BeCu connectors and OFHC copper wires. The insulating ceramics are made of Macor, a machinable ceramic. Near the center right of the photo you can see the CaO holder (no CaO present in photo), and to the right of that is the potassium dispenser. On the far right you can see the ceramic insulator and tantalum

[§]alkali metal dispenser type K/NF/2.9/12/FT 10+10, SAES Getters USA, Inc., Colorado Springs, CO

collimator.

6.4.2 Transport

Transporting neutral alkali atoms with high efficiency is not easy. The schemes of our “competitors,” who have the luxury of isotope separators and/or large production yield, begin with a moderately energetic beam of alkali ions which can be collimated, transported, and focused using electrostatic optics. However, our target is designed to optimize yield using our relatively low-energy accelerator and to produce neutral potassium straight out of the target; changing the potassium into an ion as an interim stage would introduce additional complexity we wanted to avoid.

We therefore must transport our potassium atoms out of the CaO target and towards our funnel cell as neutral atoms. The problem with this approach is that the valence electron of any alkali makes it highly chemically reactive with many materials. For the remainder of materials with which it does not react chemically, it is typically adsorbed to the surface with exceedingly long lifetimes, given by the Arrhenius expression

$$\bar{\tau} = \tau_0 e^{E_d/kT}, \quad (6.10)$$

where $\bar{\tau}$ is the mean surface lifetime and E_d is the desorption energy [Scheer et al., 1971].

Thus we need a material with a low desorption energy and high resistance to radiation. Stephens et al. [1994], among others, has suggested pyrex and alkali resistant glass. Although these materials have low adsorption energies, their chemical reaction rate is quite high, especially at elevated temperatures. Recall that the CaO target is at roughly 800°C and thus materials near it are heated radiatively. Warm sapphire has a low adsorption energy, but the surface must be carefully prepared to maintain a low reaction rate.

We next turn to materials with low work functions, below the ionization potential of potassium (4.34 eV). This ensures that the atoms comes off the metal primarily as neutrals (via the Saha-Langmuir relation). This also means the metal has a small adsorption energy, which is proportional to the work function. For this material we chose yttrium, since it has a good balance of work function (3.1 eV), workability (available as a foil), temperature and radiation resistance (melting point 1800 K), and vacuum compatibility. In addition, Paul Voytas has had experience using yttrium in

a related application while at Stony Brook [Simsarian et al., 1996a].

Again, referring to Figure 6.8, we see the target and transport scheme. The thin yttrium foil lines a machined graphite tube[¶] that is wrapped by a solenoid of coaxial heater wire. In turn, this assembly is wrapped with a few layers of thin tantalum foil, which acts as a heat shield, protecting the nearby stainless steel chamber. Graphite was chosen as a support because it is readily machinable, thermally conductive, withstands very high temperature, and holds relatively little hydrogen in its matrix (most machinable metals, even pure elements, harbor immense amounts of hydrogen in their structure that outgas constantly at high temperature). After being machined, the graphite tube was vitriated^{||} to seal some of the pores and further improve outgassing properties. We have not tested to see if this vitriation process has a significant effect.

Figure 6.10 is a photo taken from the underside of the target chamber; the facing flange is a standard 6" conflat. The elliptical shape near the bottom of the chamber is the entrance to the yttrium/graphite tube. The U-shaped bracket at the center, bolted to the inside of the chamber, holds two spring-loaded screws horizontally that support the entrance of the graphite elbow. The feed-through on the right and wires visible in the photo supply current to the coaxial heater wire. The output end of the elbow (nearest the funnel cell, see Figure 6.8) is supported by a stainless steel mesh annulus that centers the graphite tube in the close-coupler mounted to the top of the chamber, not visible in this photo.

6.4.3 Vacuum system

Description

The main chamber of the vacuum system is the same as described in §4.4 and illustrated in Figure 4.4, except that we have now replaced the room-temperature potassium “oven” with the funnel described in chapter 5 and added an all-metal bakeable valve which serves as an intermediate, differentially pumped chamber. The target chamber and funnel cell are connected using a novel “close-coupling” adapter** that allows two tapped flanges to be connected with minimal clearance. The entire tar-

[¶]AXF-5Q grade, Poco graphite Inc, Decatur, TX. This grade has high density and zero effective porosity.

^{||}Vitre-cell Inc., Bay City, MI.

**Kimball Physics

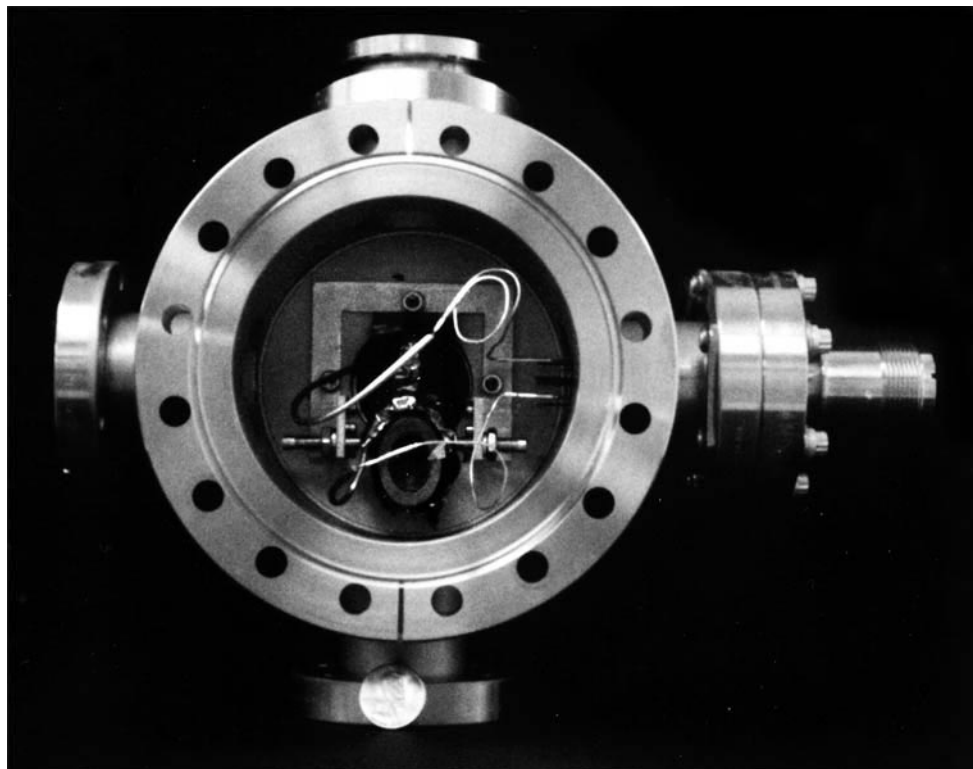


FIGURE 6.10: Photo showing inside of target chamber. The ellipse near the bottom of the chamber is the yttrium-tube inlet, supported on either side by spring-loaded screws. The screws are held in place by the U-shaped bracket which is bolted to tapped holes inside the chamber. The coiled wires provide current to the thermocoax heaters, used to heat the yttrium tube to 900°C .

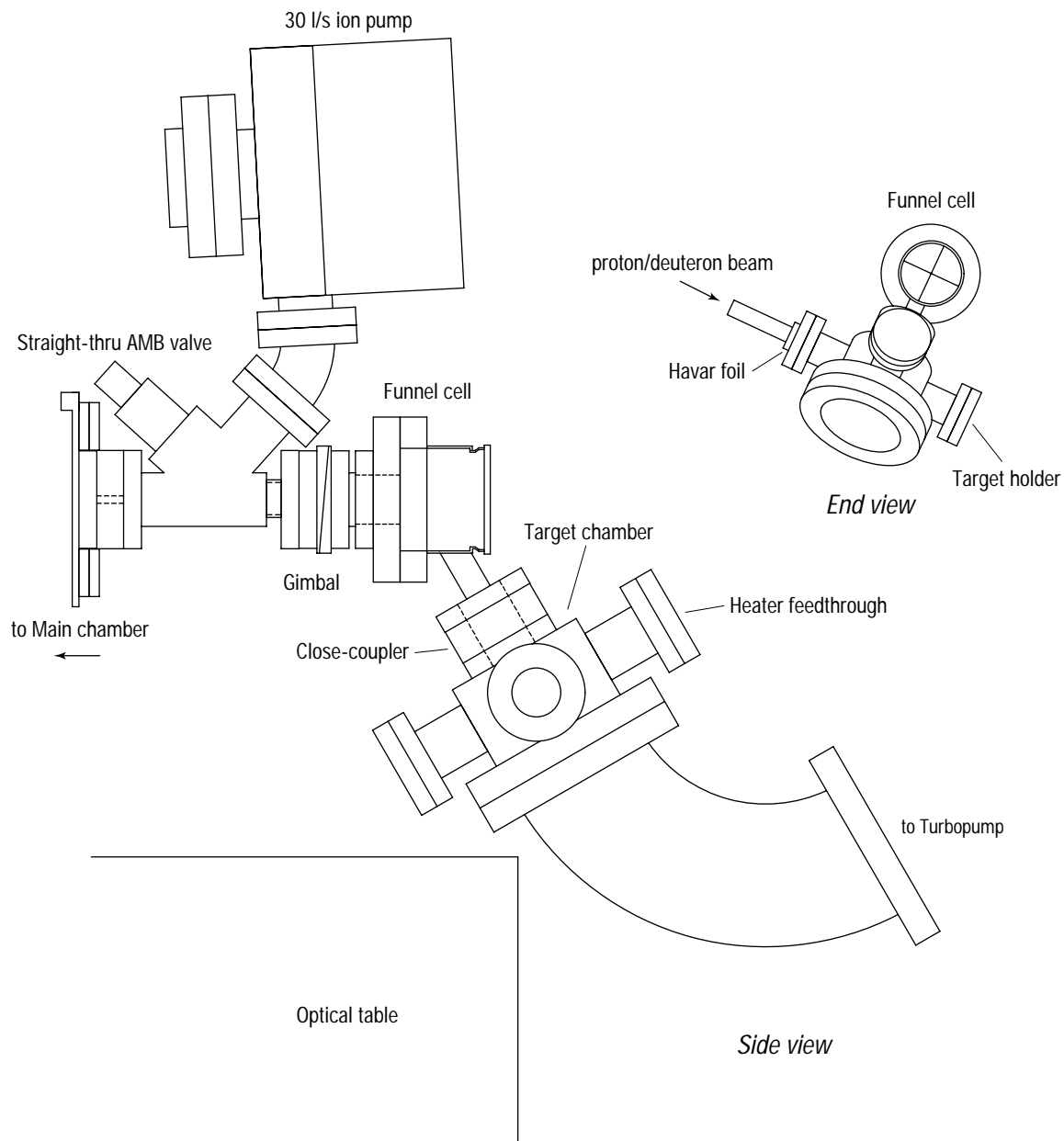


FIGURE 6.11: High vacuum system for target and funnel viewed from side; inset is end view. For clarity, optics, magnetic field coils, suspended optical breadboard, and accelerator vacuum components are not shown. The target chamber and funnel cell correspond to chamber “1” in Figure 6.12, the AMB valve to chamber “d”, and the main chamber to “0.”

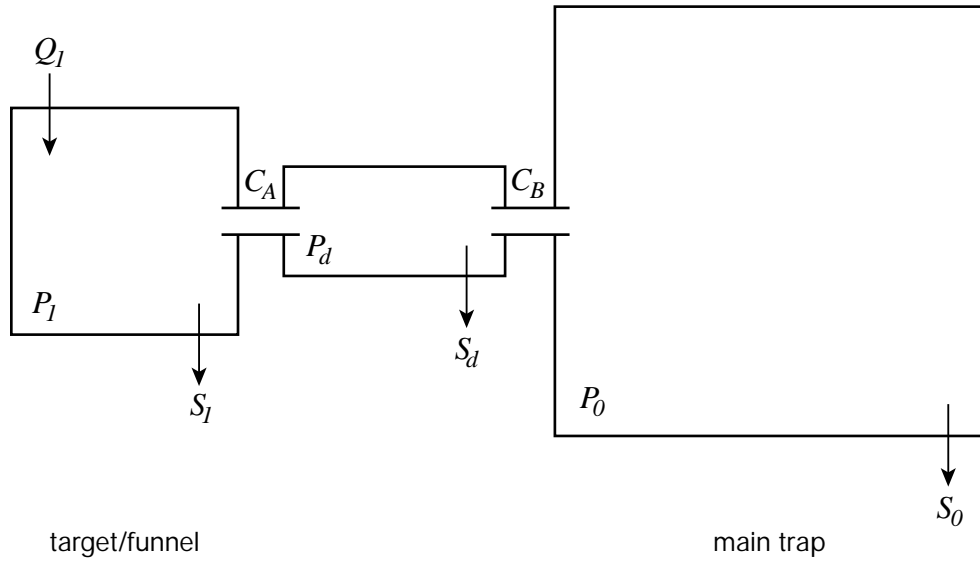


FIGURE 6.12: Schematic of gas load and pumping considerations, showing target chamber, differentially pumped region, and main trapping chamber.

get chamber is pumped by a 220 l/s turbopump^{††} backed by a dry diaphragm pump^{‡‡}, which eliminates the threat of oil contamination. The entire funnel and target vacuum system is illustrated in Figure 6.11.

This system is separated from the relatively dirty low-vacuum of the tandem by a thin ($2.5 \mu\text{m}$) Havar foil mounted between two polished copper gaskets. The sandwich of gasket-Havar-gasket is mounted as a single conventional gasket would and carefully clamped; the polished gasket surfaces form a robust seal with the Havar and each other. The Havar foil is thin enough that minimal scattering of the accelerator beam occurs. The foil is therefore quite fragile and the target and tandem vacuum systems must be roughed together. Furthermore, the tandem and foil are separated by a gate valve which can be closed when not operating to reduce the risk of foil breakage. When closed, the vacuum between the valve and Havar foil is maintained by a small appendage ion pump.

Gas load analysis

A simplified schematic, showing the essential elements of the differential pumping, is shown in Figure 6.12. Chamber 1 represents the target chamber and funnel combination; for this analysis, we consider that the funnel and target are at the same pressure. In reality there is a small pressure drop between them due to the conductance of the yttrium tube assembly (for H_2 , this conductance is approximately 10 l/s, so our approximation isn't too bad). The middle chamber d is the all-metal bakeable valve and ion pump. Chamber 0 is the main trapping vacuum chamber, pumped by a TSP and ion pump.

The target gas load Q and turbopump S_1 balance one another to produce an equilibrium pressure $P_1 = Q_1/S_1$ in the target. This gas load is roughly divided between out-gassing from the extremely hot yttrium foils, carbon elbow, and coaxial heater wire (which is filled with alumina powder as an insulator) and by the gas and heating generated by the deuteron beam. The proton/deuteron beam itself generates a significant gas load; if we assume that the entire beam recombines into H_2/D_2 after thermalizing, for a $2 \mu\text{A}$ beam and a roughly 1 l target volume we get an effective gas load $Q = 2 \cdot 10^{-4} \text{ torr l/s}$. Since our turbopump's speed is about 200 l/s for hydrogen and we achieve target pressures $P_1 = 4 \cdot 10^{-8} \text{ torr}$ while running, we suspect that the protons and deuterons are being implanted in the tantalum.

Next we consider the gas load presented by the funnel. Referring again to Figure 6.12, the gas flux through channel A is given by

$$S_d P_d = C_A (P_1 - P_d) \quad (6.11)$$

and through channel B by

$$S_0 P_0 = C_B (P_d - P_0) + f C_A (P_1 - P_d) \quad (6.12)$$

where f is the fraction of gas “channeled” through, passing directly through from chamber 1 to chamber 0, unaffected by the differential pumping. Since we are working in the UHV range where inter-gas collisions are rare, the differential chamber is short, and there is a large pressure drop from chamber 1 to chamber 0, this can be a significant

^{††}Balzers Model TMU 260. This pump runs at 60,000 rpm and has nearly full pumping speed for hydrogen.

^{‡‡}Leybold, Inc.

source of gas load on the main chamber.

Under the conditions that $f \ll 1$, $C_A \ll S_d$, and $C_B \ll S_0$, we find the pressure ratio

$$\frac{P_0}{P_1} = \frac{C_A}{S_0} \left(\frac{C_B}{S_d} + f \right); \quad (6.13)$$

thus to achieve a big pressure drop, we obviously want large pumping speeds, low conductance between chambers, and little channelling.

The gas conductance from the funnel hole, which is really a tube, is well-known (for example, Roth [1982]):

$$C = 3.81 \sqrt{\frac{T}{m}} \frac{D^3}{L} [l/s] \quad (6.14)$$

where T is the absolute gas temperature, m is the mass in amu, and D and L are the tube dimensions in centimeters. For thermal hydrogen and our funnel orifice $C_A = 11/s$ ($D = 2$ mm, $L \approx 3.8$ mm).

The differential pumping region is served by a 301/s pump, and the second hole out to the main vacuum system has $C_B = 3.51/s$ for H_2 . The main chamber is pumped by a combination of a 1501/s differential ion pump and a Varian mini-Ti-ball titanium sublimation pump. Factoring in relative pumping efficiencies and conductances, they have a speed of about $P_0 = 13001/s$ combined for H_2 at the trap location in the main chamber. (For N_2 and similar gases, they have a combined speed of about 6001/s and about 401/s for inert gases.)

For our orifice geometry, the channeled fraction $f \sim 10^{-4}$ and is negligible. Combining these values into equation 6.13 above, we get $P_0/P_1 = 10^{-4}$; with about $2 \mu A$ of d^+ beam on target and the yttrium tube is at typical 1000 – 1100 K operating temperature (no direct target heating), $P_1 = 4 \cdot 10^{-8}$ torr, for a pressure $P_0 = 4 \cdot 10^{-12}$ torr.

Measurements

Using the trap loss-rate methods described in §4.5.3, we measure the hot-background gas limited trap lifetime to be 170 s, consistent with this estimated pressure. When the yttrium tube is cold and with no beam on the target, the target pressure $P_1 \sim 4 \cdot 10^{-10}$ torr, and the trap lifetime is approximately 400 s. These excellent pressures were achieved without baking; the entire system was baked out thoroughly when first assembled, but has been up to air several times and has not been baked since.

From these measurements of γ we can actually estimate a pressure. Using a magnetostatic trap operating in a cryogenic environment to produce very low pressure, Willems and Libbrecht [1995] have estimated van der Waals cross sections for He-Cs collisions. They report an integrated cross-section of $2 \cdot 10^{-9} \text{ cm}^3/\text{s}$ for 300 K He and typical MOT trap depths. By assuming the van der Waals interaction strength between helium and cesium is similar to the interaction between H_2 and potassium, we find that $1/\alpha = 400 \text{ s}$ corresponds to a pressure of $4 \cdot 10^{-11} \text{ torr}$. This may actually underestimate the vacuum quality since the van der Waals interaction for helium is stronger than for H_2 [Willems and Libbrecht, 1995].

6.4.4 Optical system

The $\text{Ti:Al}_2\text{O}_3$ laser, acousto-optic modulators, and locking electronics are located in a separate room, well-shielded from radiation and kept fairly clean. Other options were considered, but limited space in the accelerator area and desire for accessibility were strong motivators. This also extends the life of the sensitive laser optics and makes them completely accessible even while running the accelerator, allowing us to change our laser setup to switch to any isotope while still leaving the accelerator running.

The main drawback of this approach is the requirement of transporting nearly a watt of single-mode laser light about 45 m from the laser room to the trap optical table located at the end of the accelerator. Running a single-mode fiber of that length is quite simple, but at such high powers, stimulated Brillouin scattering in the fiber limits the amount of power we can transport [Smith, 1972].

Brillouin scattering is a nonlinear optical process whereby the propagating (pump) light induces an index grating in the medium that scatters the pump light through Bragg diffraction off the induced grating. The bandwidth for this process (proportional to the inverse phonon lifetime) is only about $\Delta\nu_B = 10 \text{ MHz}$, and the shift in the scattered light (for our fiber and wavelength) is about 20 GHz below the pump frequency [Agrawal, 1989]. Since any light that is generated by the process is shifted far from any possible atomic resonances and almost all of it is counterpropagating, this light should not pose a problem.

For a fiber whose length is short compared to the attenuation length (clearly our situation, with $\sim 3 \text{ db/km}$ attenuation), the threshold for this process is approximately

given by

$$P_{\text{crit}} \simeq 21 \frac{A_{\text{eff}}}{\gamma_B l_{\text{eff}}} \quad (6.15)$$

where A_{eff} is the effective cross-sectional area of the fiber, $\gamma_B \approx 5 \cdot 10^{-9} \text{cm/W}$ is the gain coefficient for Brillouin scattering in silica, and l_{eff} is the length of the fiber. For our 45 m fiber (3M Type 4611, polarization-maintaining, $5.3 \mu\text{m}$ mode field diameter), this threshold is about 200 mW.

It is interesting to note that in the early stages of our experiments, before we knew of Brillouin scattering, we observed all of these characteristics experimentally, including the sharp power threshold and the bandwidth — when the laser frequency was swept or was multi-mode, the power through the fiber rose substantially.

To overcome these limitations, we made a variety of changes. First we shortened the fiber to the minimum length necessary. Next, we placed our hyperfine AOM, which has about 60% efficiency, before the fiber rather than after it. The benefits of this are twofold: it reduces the total amount of power launched into the fiber, and it divides the launched power into two different frequencies of light, well separated by a frequency $\nu_{\text{hyp}} \gg \Delta\nu_B$. Thus each color scatters individually, allowing us to launch nearly 200 mW of each color rather than total.

Finally, we use a polarization-preserving fiber and launch one color along the slow axis, and the other along the fast, which may have some additional benefit in raising the critical power. The output end of the fiber is angle-polished and connectorized, and the input end is left bare. The angle-polishing (typically 8° to normal) prevents étalon effects which can cause the output power to fluctuate, and leaving the input end bare allows the fiber to be easily re-cleaved when the fiber is damaged from the high incident laser intensity.

The essential optical layout before the fiber is shown in Figure 6.13. As described in chapter 2, we pick off some of the laser light, shift its frequency using an AOM, and lock it to a heated vapor cell of potassium. The second hyperfine AOM is used to produce the other color required for trapping. The AOMs and some associated mirrors are mounted on kinematic magnetic bases so that they can be removed and replaced quickly, allowing us to readily switch between trapping any isotope. In addition, each AOM can be single- or double-passed, with only a minor amount of mirror tweaking. Changing the setup for different isotopes takes about twenty minutes. In the case of ^{38}K and ^{40}K , only the frequency of the modulators needs to be changed and the switch

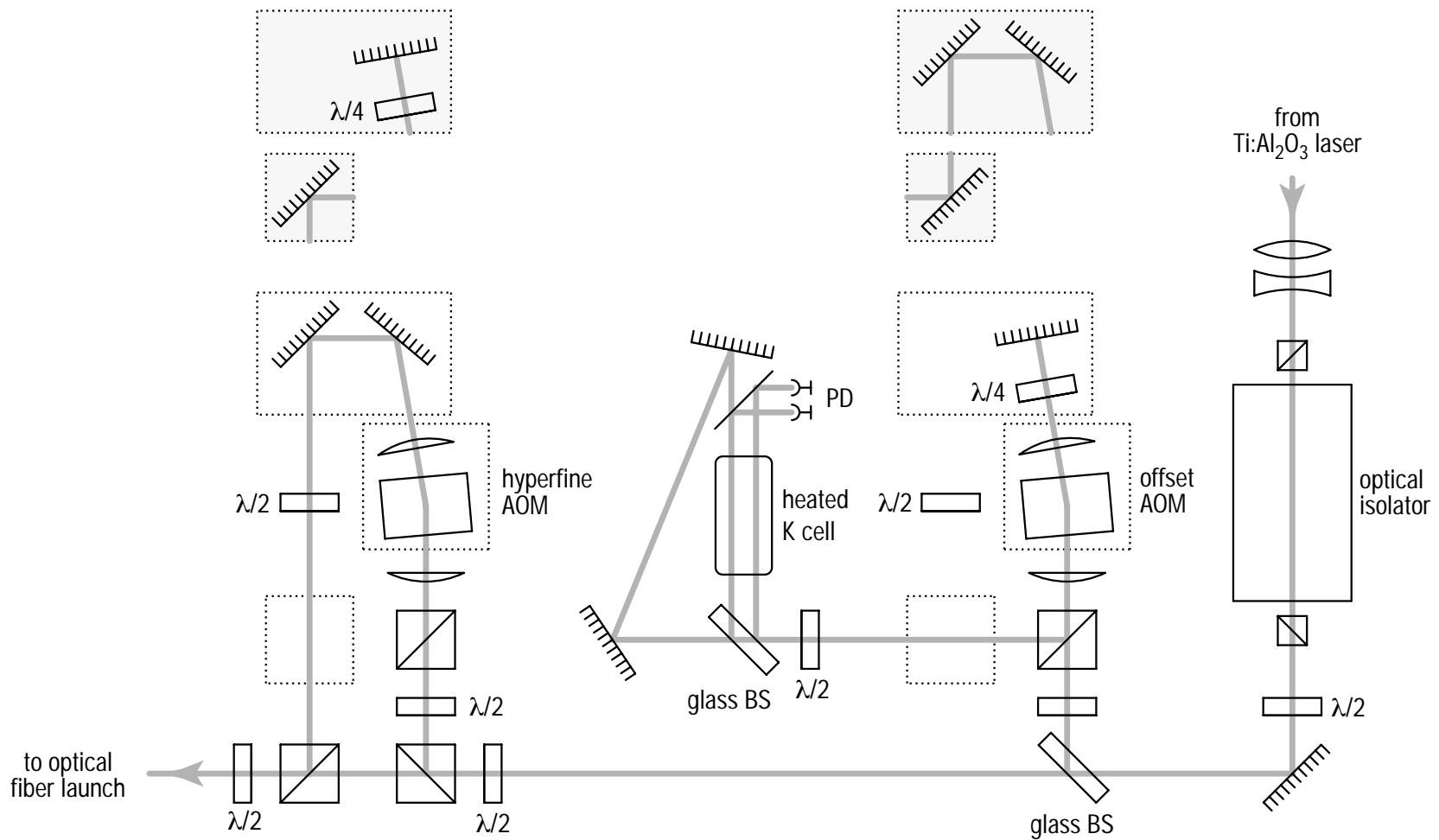


FIGURE 6.13: Optical table layout for producing trapping light. The AOM's and associated optics are mounted on kinematic magnetic mounts and can be swapped in a few minutes. Either AOM can be single- or double-passed, which is necessary to be able to trap the $^{37-41}\text{K}$ isotopes.

can be done in only minutes, making ^{40}K a convenient test to ensure the entire system is working properly.

The optics surrounding the trapping chamber and funnel are the same as described in §5.4 and by Figure 5.7. As is clear from Figure 6.11, there is no easy way to place optics for launching the funnel beam. These optics are attached to a suspended 3/4" thick aluminum optical breadboard, which is bolted to the main vacuum chamber and main optical table using 1.5" diameter posts. This arrangement is quite sturdy and allows us to mount a telescope, waveplate, and steering periscope out of the way of the target chamber and pumping system.

6.5 System efficiency

6.5.1 Target and transport yields

Initial proof-of-concept measurements of our production mechanism were determined by measuring the characteristic gamma ray spectrum of ^{38}K using an intrinsic germanium detector. The 2.18 MeV γ of ^{38}K passes readily through the walls of the chamber, so simply measuring a spectrum and the detector solid angle gives the activity in the source, which for a 400 nA, 11 MeV d^+ beam gives a ^{38}K production rate of $3 \cdot 10^7 \text{ s}^{-1}$, measuring the total amount created regardless of where it goes. For ^{37}K , this diagnostic is much less sensitive, since a majority (98.1%) decay directly to ^{37}Ar (see Figure 6.1) and we were unable to detect a clear γ signal. Furthermore, due to the negative Q -value we expect to produce less ^{37}K overall.

Another early test involved measuring the transport efficiency of the yttrium tube assembly using natural potassium. Using a potassium dispenser (described in §6.4.1) and a hot-wire ionization detector, we measure the transport efficiency of the yttrium tube under various conditions and temperatures. The optimum value, achieved at about 900°C, was approximately 10%.

The yield of entire target and transport assembly together was tested by substituting the funnel cell (see Figure 6.11) with a standard 2-3/4" CF tee and allowing the potassium to deposit on the side of the tee. To detect the decays, one end of the tee was sealed with a thin Havar foil (as described in §6.4.3), allowing the beta particles to escape. The escaping positrons are measured using a $\Delta E - E$ telescope consisting of two stacked plastic scintillation counters operated in coincidence, the

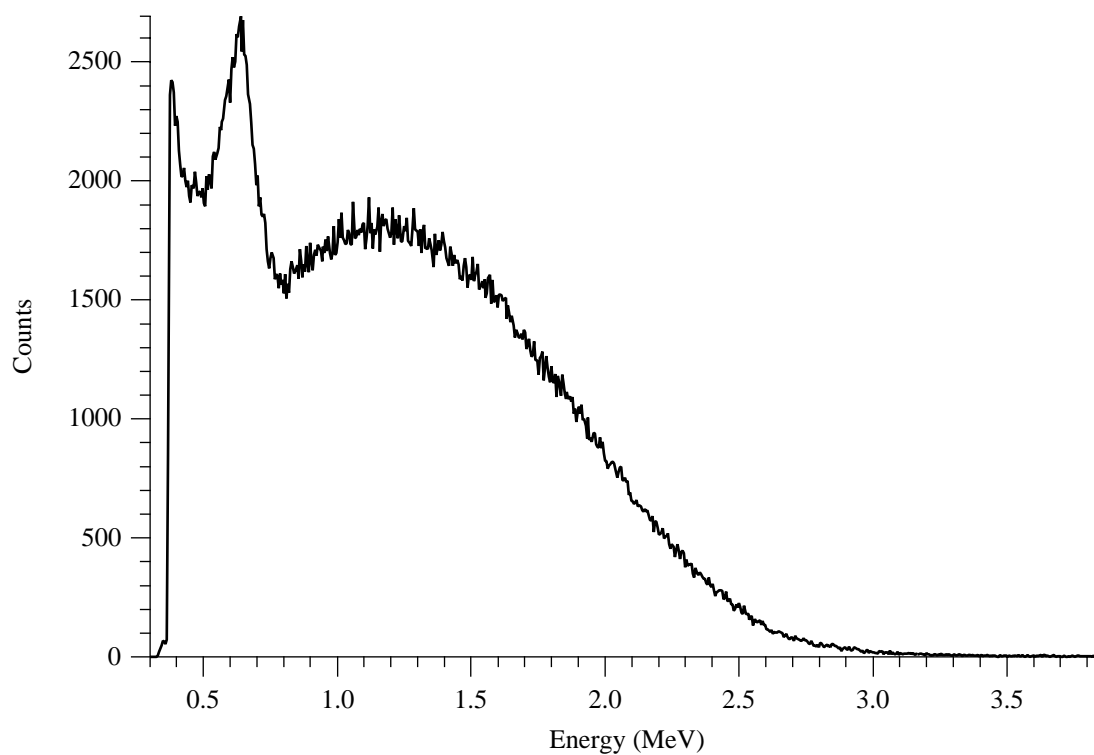


FIGURE 6.14: Beta spectrum of ^{38}K taken with a $\Delta E - E$ telescope using plastic scintillators; the energy scale is approximate. The endpoint energy for the prominent branch (99.333%) is 2.72 MeV. The two narrow peaks are not part of the β spectrum; the first results from pedestal suppression of noise, and the second is a Compton backscattering peak.

first one thin (ΔE), the second thick (E). The coincidence provides rejection against background gamma-rays and neutrons. A typical β spectrum we observe for ^{38}K is shown in Figure 6.14.

Using this technique we measure $3 \cdot 10^5 \text{ s}^{-1}$ of ^{38}K for 400 nA at 11 MeV, and $4.5 \cdot 10^4 \text{ s}^{-1}$ of ^{37}K for a beam current of $2 \mu\text{A}$. This gives us about 1% transport efficiency from the target to the tee. This efficiency combines three factors: the fraction of ^{38}K that effuse out the target, the portion of those that actually enter the yttrium tube, and of those, the amount that make it out the other end of the tube. Our separate tube transport measurements then imply that 10% of the potassium made in the powder escape and enter the tube.

6.5.2 Pyramid loading rates

Let's now consider the expected loading rate of the funnel from a flux of hot atoms q_0 , exiting the heated yttrium tube and entering the illuminated portion of the funnel. Using a large laser beam to illuminate the funnel results in a good fraction of the cell's volume V being filled by trapping light with intensity greater than saturation intensity I_{sat} . Cooling of the atoms in three dimensions occurs only inside the pyramid region, and in the cylindrical region in front of the pyramid, we cool only axially as there are no transverse beams here. However, on average, an atom rattling around in the cell will pass through the trap volume.

In passing through the capture volume, the atom has a probability η_v (equation 4.7) of being cooled and trapped (in this case, ejected from the funnel). If not captured by the trap, the atom bounces from the dryfilm-coated walls, re-thermalizes, and makes another pass through the trap. The ratio of the area of the inlet port from the yttrium tube to the surface area of the whole cell is about 1:80, and thus we expect the atoms to bounce about $N_b = 80$ times on average before bouncing out. Finally, once the atoms are cooled and ejected, they are trapped by the main MOT with a transfer efficiency η_T , which we measured experimentally and discussed in §5.5. Putting this all together we derive a loading rate

$$L_{\text{main}} = q_0 \eta_v N_b \eta_T = \frac{1}{2} q_0 \left(\frac{v_c}{\alpha} \right)^4 N_b \eta_T, \quad (6.16)$$

using the definition for η_v from equation 4.7.

It is instructive to consider this loading process from the vantage of a vapor-loaded

trap, and compare to the formulation above. Due to the many bounces possible in the cell, the incoming beam of flux q_0 entering the cell is essentially turned into a vapor of density n

$$n = \frac{q_0 \tau N_b}{V_{\text{cell}}}, \quad \tau = \frac{d}{\bar{v}}, \quad (6.17)$$

where τ is the mean time between bounces, given roughly by the diameter of the cell d and $\bar{v} = (2/\sqrt{\pi})\alpha$, the mean thermal velocity. We can then use the vapor cell loading rate coefficients ℓ we have measured and studied with our simple six-level model (§2.4). The loading rate of this vapor cell is then just

$$L'_{\text{main}} = n\ell\eta_T. \quad (6.18)$$

We might expect these two formulations to agree with one another. Let us ignore for the moment our loading rate coefficient measurements and recall the simple vapor-cell loading model of Monroe et al. [1990] discussed in section 2.3:

$$\ell_{\text{vap}} = \frac{1}{2} V_{\text{trap}}^{2/3} \frac{v_c^4}{\alpha^3}, \quad (6.19)$$

which results from a simple statistical analysis of a thermal beam of atoms crossing a spherical surface of diameter d . Combining this loading model with equation 6.18 above we arrive at

$$L'_{\text{main}} = \frac{1}{2} q_0 \left(\frac{v_c}{\alpha} \right)^4 N_b \eta_T \left(\frac{\sqrt{\pi} d V_{\text{trap}}}{2 V_{\text{cell}}} \right) \quad (6.20)$$

differing from L (equation 6.16) only by a purely geometric factor that accounts for differences in the trap to overall cell size.

6.6 Preliminary results

We have attempted to trap ^{38}K using our funnel-MOT system, but have not yet observed it. Based on our measured target yield and transport efficiency, the funnel loading rate and transfer efficiency measured in chapter 5, and the enhancement of a dryfilm coated funnel cell, we should be able to trap at least 100 ^{38}K atoms in the main trap. Here we will justify this estimate and attempt to diagnose reasons for not trapping based on measurements we have made of the entire system using natural potassium.

We test the entire system beginning at the target using the natural potassium dispenser, which emits atoms at the target region. As discussed before (§6.4.1), it is very difficult to calibrate or measure the amount of potassium coming out of the dispenser due to the non-linear nature of the release mechanism.

For the hot yttrium tube transport system we rely on our earlier measurements (§6.5.1) using a conflat tee and $\Delta E - E$ telescope, which gave a tube transport efficiency of about 10% and a total target to tube exit efficiency of 1%. Furthermore, because we have measured a flux of ^{37}K with this method, we know that the dwell time on hot tube must be not much longer than the ^{37}K half-life, 1.2s.

We have little reason to believe these numbers have changed since the funnel cell was attached in place of the tee, but nevertheless we performed a in-situ test of the dwell time by turning the dispenser on and allowing it to reach steady-state. By turning it off abruptly and measuring the loading rate as a function of time since the dispenser was turned off, we put an upper limit on the dwell time of less than a minute.

Though we cannot directly measure the natural potassium flux entering the cell, we can measure it indirectly by blocking the funnel laser light and loading the main MOT from the effusive beam formed by the vapor cell that results. To be certain that we are loading from the effusive beam and not from some residual background vapor, we close the AMB valve that separates the funnel and main MOT; we see no discernible loading when it is closed. With the valve open, the MOT loads only from the atoms effusing out of the funnel's apex hole. We measure a loading rate $L = 0.3 \text{ atom/s}$ with $I_{\text{tot}} = 80 \text{ mW/cm}^2$, detuning $\Delta = -43 \text{ MHz}$, and a field gradient of 12 G/cm , with $2w_0 = 3.4 \text{ cm}$ diameter beams.

These loading-rate measurements can be used to calculate the effective atom density in the funnel, which we can compare with the density of radioactives we expect using our flux estimates in section 6.5.1. From the Scoles angular distribution discussed in section 4.2.1 and calculating the solid angle determined by the second aperture separating the differentially pumped region from the main chamber (see Figure 6.11), we determine that a fraction $\eta_{\Omega} = 1.4 \cdot 10^{-4}$ of the total flux will enter the trap. In section 4.5, we used our effusive-beam loading measurements (Figure 4.6) to estimate $\eta_v \approx 9 \cdot 10^{-4}$ under those conditions. Here we are using similar beam sizes, but approximately half the intensity; based on our simple model and measured results (see Figure 2.6) we note the loading rate scales roughly as the intensity, giving us

$\eta_v \approx 6 \cdot 10^{-4}$ for our conditions.

The total loading rate for this effusively-loaded MOT is then just the product

$$L_{\text{main}} = q_{\text{eff}}\eta_{\Omega}\eta_v, \quad (6.21)$$

where q_{eff} is the total flux effusing from the funnel apex hole. Combining this with the equation 4.1 relating q_0 to n_{vap} , and our estimates of η_{Ω} , η_v above, and our loading rate of 0.3 atom/s, we find that n_{vap} (^{39}K) is $3 \cdot 10^4 \text{ cm}^{-3}$.

When the funnel is operating and optimized to the best of our ability under the same conditions, we observe a loading rate of 5300 atom/s, an 18 000-fold improvement over the effusive case.

In order to use these values to make predictions about ^{38}K , it is helpful to see the effect of loading ^{40}K , which should have capture velocity and loading characteristics more similar to ^{38}K . However, ^{40}K is 8000 times less abundant than ^{39}K and thus there is not enough effusive flux to perform the above procedure directly, so we use $n_{\text{vap}}[40] = n_{\text{vap}}[39]/7970 = 4 \text{ cm}^{-3}$. We measure a loading rate of the funnel-loaded MOT for ^{40}K of $L = 0.3 \text{ atom/s}$. This corresponds to a $\eta_v[40] \approx 3 \cdot 10^{-4}$, half that of what we observe for ^{39}K , a reasonable result considering ^{40}K lacks the hyperfine-structure enhancement of v_c .

We can directly scale these results to make a prediction for the loading of ^{38}K by using equation 6.17 to convert the known flux $q_0 = 300\,000 \text{ s}^{-1}$ of ^{38}K emanating from the end of the yttrium transport tube into a density. For the dimensions of our cell and assuming 80 bounces, we expect $n = 10 \text{ cm}^{-3}$ of ^{38}K ‘‘vapor,’’ more than twice as much as we have of natural ^{40}K from the dispenser. Assuming similar capture rates for ^{38}K and ^{40}K , this predicts a loading rate into the main MOT of about 0.7 atom/s; with a trap lifetime of 170 seconds, we expect more than 100 trapped ^{38}K atoms. Our detection system is capable of sensing fewer than 20 trapped atoms.

We have also directly measured the loading rate of the funnel operating as a MOT, now using natural potassium from the dispenser near the target (our method is described in detail in §5.5.2). Because of the higher pressures the funnel now operates under (due to out-gassing from the heated yttrium tube assembly and target), the trap loads more quickly than our fairly slow CCD camera can resolve. Nonetheless, we can set a lower limit on the funnel loading rate and can measure the loading rate of the cold funnel beam loading the main MOT to give an upper transfer efficiency limit

of $\eta_T = 3\%$. We suspect this value is low due to misalignment of the funnel symmetry axis with respect to the atomic beam axis (defined by the vacuum apparatus) and with respect to the funnel laser axis. Although the misalignment is only about 2° and the push beam still propagates exactly down the atomic beam axis, the transverse cooling beams in the funnel are misaligned and push the atoms off-axis as they leave the funnel. Steps are currently being taken to correct this misalignment.

In addition, it appears the funnel itself has poor capture efficiency from the vapor. By combining the vapor density ($1.7 \cdot 10^6 \text{ cm}^{-3}$) derived from our effusively-loaded main MOT with the loading rate made directly in the funnel operating as a MOT ($7 \cdot 10^6 \text{ s}^{-1}$), we find $\ell_{\text{funn}} = 4 \text{ cm}^3/\text{s}$. Using very conservative values for the funnel parameters of $V^{2/3} = 100 \text{ cm}^2$ and $v_c = 30 \text{ m/s}$, and equation 6.19 we get a lower-limit for the expected loading rate of $90 \text{ cm}^3/\text{s}$. This points either to an error in our method of estimating the vapor pressure from effusive loading, or that the funnel has extremely poor loading efficiency. One source of error in the effusive estimation technique could be an anomalous source of atoms located between the valve and funnel exit, but we have no evidence of this.

Comparison with another pyramidal MOT points to inefficient funnel loading. Using the values given for the rubidium pyramidal MOT Lee et al. [1996] with 1.5 cm beams and 7 mW of total power we estimate his loading rate coefficient to be $3 \text{ cm}^3/\text{s}$. Considering our much higher power, larger beam diameters, and larger capture velocity for potassium, our value of ℓ should be much higher than his. Currently we are attempting to understand the poor funnel loading rate, among other things.

Chapter 7

Conclusions and Outlook

In this dissertation I have described a series of experiments leading to the construction of a funnel-loaded MOT system suitable for trapping radioactive potassium isotopes with lifetimes of several minutes. Our immediate goal is to measure the angular distribution of decaying positrons from a cold sample of radioactive ^{38}K to determine the beta asymmetry parameter, which is highly sensitive to any possible deviations from the Standard Model of weak interactions.

As part of this process we have studied various methods of loading a MOT and modeled them using a simple rate-equation model. We observe that the populous isotopes of potassium ^{39}K and ^{41}K , because of their small hyperfine structure, are trapped in a manner slightly different from other alkalis, tuning below the entire hyperfine manifold. This has the effect of giving the potassium MOT a broad tuning range and high capture velocity, significantly enhancing our loading rates. Trap loading measurements confirm the predictive power of our model, thus allowing us to rely upon its results in directing our experimental approach.

We have thoroughly characterized the vapor-cell loaded MOT for potassium, the first trap for potassium ever made. We have measured the trap density and loading rates as a function of trap parameters, including trapping beam intensity and diameter, and laser detuning. In this apparatus we observe evidence of cold collisions between trapped potassium atoms with a collisional rate coefficient comparable to that measured in other alkalis (on the order of $10^{-10}\text{ cm}^3/\text{s}$). We see a significantly lower collisional loss rate in ^{41}K than in ^{39}K , an effect that has also been observed in other alkalis.

We have also created a beam-loaded potassium MOT with an extremely long

background-pressure limited lifetime of a few hundred seconds. The trap was loaded from a very feeble effusive atomic beam of natural potassium to which we added a two-dimensional magneto-optical collimator. The collimator improved the trap loading rate by a factor of eight, and the addition of simple longitudinal slowing improved this by another factor of two. Using our measurements of the loading rate, we estimate a ^{39}K trap capture velocity in excess of 60 m/s.

The next development towards readying our beam-loaded trap for radioactive potassium was to create an atomic funnel capable of producing a cold, collimated beam of potassium. This enables us to maintain substantial trap lifetimes in an extremely high vacuum environment while loading from a moderate-pressure beam source containing a substantial amount of undesirable species. Our atomic funnel consists of four mirrors arranged to form a hollow pyramidal shape, with a hole drilled at the apex to allow atoms and light to escape. The funnel is illuminated by a large-diameter laser beam, reflecting from the four mirrors in a manner that creates a six-beam trapping configuration. A portion of the laser beam leaking from the hole pushes cold atoms out to form a collimated beam. We couple this cold atomic beam to our low-pressure MOT and see a transfer efficiency between the funnel and trap of about six percent.

To create the radioactive potassium needed for our eventual asymmetry measurements, we have built a unique target and transport system used with the 12 MeV tandem accelerator. The target is capable of producing a thermal beam of neutral ^{37}K and ^{38}K in quantities which should be sufficient to make a trap of ^{38}K with enough activity for good signal-to-noise in the β detectors. We have coupled the target with our funnel and trap and have successfully transferred natural potassium from the target region to the main trap. Although we have not yet trapped radioactive ^{38}K , we are in the process of carefully diagnosing each stage of the system to determine why. Among the many technical reasons that may be hindering our efforts is the possibility that we simply have not hit upon the right laser frequency tuning scheme that matches the unique level structure of ^{38}K .

The prospects for these experiments are very exciting. Once we begin trapping ^{38}K , it will become possible to carefully optimize each element of the system to maximize the number of trapped atoms. To reach a benchmark rate of one detected positron per second, roughly the rate needed to achieve good statistics in a reasonable time, we will need to trap about 10 000 ^{38}K . This will give us statistics of better than 1% while counting for only a few hours; we expect that systematic effects and second-order

nuclear corrections will be below the 1% level.

A ΔE - E detection system has already been constructed to fit a thin re-entrant UHV-compatible beryllium window for our chamber, with a total detector solid angle of about 2%. The low-noise electronics and counting equipment are currently being tested. Since the velocity of cold, collimated atomic beam is well-matched to the main MOT, there should be little source of background decays from untrapped ^{38}K in the main chamber. Shielding between the trap and target region will likely be necessary to reduce the number of accidental counts. We have also investigated adding a channel electron multiplier and electrostatic collection system to detect low-energy shake-off electrons from the argon decay daughter to provide additional background rejection (however, the charge state of the final product is poorly understood, see Carlson et al. [1968]; Nesnidal [1995]).

In addition we have constructed a diode laser operating at 770 nm to perform optical pumping on the $P_{1/2}$ state. Light from this laser can also be used to probe the trapped atom sample to measure the polarization, possibly via non-destructive Faraday-rotation or absorption measurements. Although our group has developed an inherently spin-polarized MOT [Walker et al., 1992a], we expect that a gated time-sequence of trapping and spin-polarization will produce larger polarization and reduce systematic error contributions.

We can also use this stable, narrow-band diode laser to measure the hyperfine structure constants and isotope shift of ^{38}K and ^{37}K . The isotope shift in ^{38}K currently has an error of ± 5 MHz, and the excited-state hyperfine structure constants have never, to our knowledge, been measured. Using a precision saturated-absorption technique to lock to our laser to stable ^{39}K will allow measurements of the ^{38}K isotope shift and $P_{1/2}$ splitting constants, but the unresolved hyperfine structure in the $P_{3/2}$ level of ^{39}K may hinder investigations of this level. A stabilized étalon may be a possible frequency reference.

Overall, this project has been quite successful and there is great promise for trapping radioactive potassium ^{38}K and ^{37}K , and we have an exciting program of nuclear and atomic experiments lined up for the years to come.

Appendix A

Stabilized titanium-sapphire laser

Here we describe the stabilization and locking technique used with our Ti:Al₂O₃ laser. In the first section we describe the cavity and optics, in the second we present the stabilization technique and electronics used, and in the third we briefly discuss the saturated absorption spectra observed in a natural potassium cell used to lock the laser on transition.

A.1 Laser cavity

An argon-ion pumped CW Ti:Al₂O₃ laser system was chosen over a diode system for two main reasons: desire for high power and lack of availability of laser diodes operating near 767 nm. High power is essential for efficient capture and slowing of the small number of radioactive atoms we make. High-power laser diodes that operate reliably at 767 nm are not yet available.*

Our laser system consists of a Coherent Innova 310 12 W argon-ion laser pumping a highly modified Schwartz Electro-Optics Titan-CW Ti:Al₂O₃ laser. The Ti:Al₂O₃ ring cavity (shown in Figure A.1) consists of four mirrors, an optical diode, an étalon and a Lyot filter (or birefringent filter, BRF), all mounted on a Super Invar[†] baseplate for improved temperature stability. The argon-ion light is focused and mode-matched into the Ti:Al₂O₃ crystal by an adjustable lens system (not shown in Figure A.1). The optical diode, consisting of a Faraday rotator and waveplate, prevents the competing,

*Recently our group built a chilled diode laser cavity that produces ~ 4 mW of 767 nm light from a nominal 780 nm diode.

[†]Carpenter Industries, Inc.

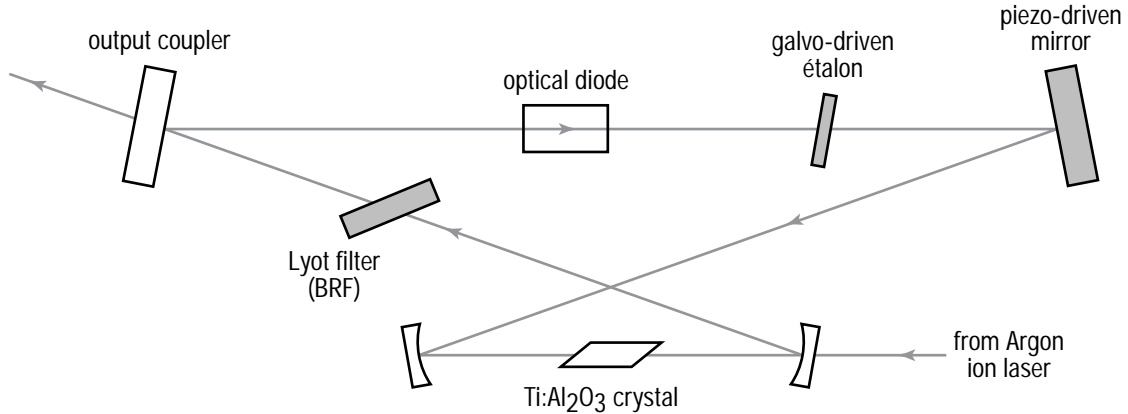


FIGURE A.1: Layout of stabilized $\text{Ti:Al}_2\text{O}_3$ ring cavity, with frequency-selective elements shown in grey. The galvo-driven étalon and piezo-driven mirror are electronically controlled by the system shown in Figure A.2.

oppositely propagating ring mode from lasing. The cavity has a free spectral range (FSR) of about 300 MHz. The stabilization technique we describe here uses elements of Vassen et al. [1990].

The laser cavity has been hermetically sealed and is kept at a slight positive pressure of nitrogen to keep out atmospheric oxygen (O_2). Molecular oxygen has a well-known absorption feature near 766 nm (see for example, Nguyen et al. [1994]) which destabilizes the laser when it is on the D_2 transition of potassium. This absorption is negligible for a beam propagating in air, but the high finesse laser cavity (about 200) makes the absorption losses substantial enough to compete with the gain of the $\text{Ti:Al}_2\text{O}_3$ crystal, forcing the cavity to lase at another wavelength.

Figure A.1 shows the three main tuning elements shaded in grey, but the reflective dielectric coatings of the four cavity mirrors themselves are the primary limit to the laser's tunable wavelength range (about 100 nm). The BRF (manually controlled) further reduces the linewidth to about a nanometer. Finally, the overall cavity itself restricts the laser to a comb of narrow longitudinal modes separated by 300 MHz. To select only one of these modes, a thin coated étalon is placed in the cavity.

This étalon, 1 mm thick and coated for $\sim 20\%$ reflectivity, is one of two active cavity-stabilization elements. It is mounted on a stabilized galvanometer to allow angle tuning. To control the cavity length, one mirror is driven by a high-voltage piezo (Burleigh Instruments) with $5\ \mu\text{m}$ of travel, or about 10 FSR, giving a total of 3 GHz of sweep overall.

A.2 Stabilization

The étalon angle and cavity length need to be controlled synchronously, in order to prevent mode hops (transitions from one longitudinal mode to another) as the length of the laser cavity changes with temperature, and to allow the laser to be continuously swept without mode hopping over a reasonable range. Synchronization is performed by making the étalon motion follow the piezo mirror’s motion. We do this passively by adjusting the amplitude and offset of the voltage sent to the galvo with respect to the voltage sent to the piezo. In addition, to make up for the nonlinear response between the lasing wavelength selected by the étalon’s angle, a small quadratic component is added to the étalon drive signal. In other words, if the signal sent to the piezo is $s(t)$, then the galvo receives

$$s'(t) = a + bs + cs^2, \quad (\text{A.1})$$

where a , b , and c are user-adjustable parameters. These parameters are determined empirically by the user, who adjusts the appropriate gain knobs (described in a moment) to make the laser sweep a continuous mode-hop free spectrum.

The laser frequency is stabilized by locking to a potassium absorption cell, heated to about 80°C by small kapton heaters (Minco). These cells are made of glass, about 5 cm long, and evacuated to approximately 10^{-8} torr and filled with a small amount of potassium metal. As shown in Figure 2.4, a small amount of laser light is picked off, sent through an acousto-optic modulator (AOM) into the saturated absorption spectrometer (optical layout details appeared in Figure 6.13). As described earlier in §6.4.4, the AOM allows us to trap various isotopes of potassium while always locking to the populous ^{39}K isotope.

Figure A.2 is a block diagram of the locking electronics. We begin in the lower left-hand corner with a ramp generator used for sweeping the laser frequency, which is sent into the locking box. The locking box serves a dual purpose: to adjust the sweep range and center frequency when sweeping, and to adjust the gain of the feedback loop when locking to an atomic line. The sweep synchronizer associates the motion of the piezo and galvo so that mode hops do not occur; in this box, offset, (coarse/fine) gain, and quad adj correspond to parameters a , b , and c in equation A.1 above. By sweeping the laser across many FSR and observing a saturated absorption signal, the sweep synchronizer can be adjusted to give 3 GHz of continuous sweep. The HV amplifier is a high-bandwidth circuit based on a design by Andrea [1988] at JILA, and the galvo

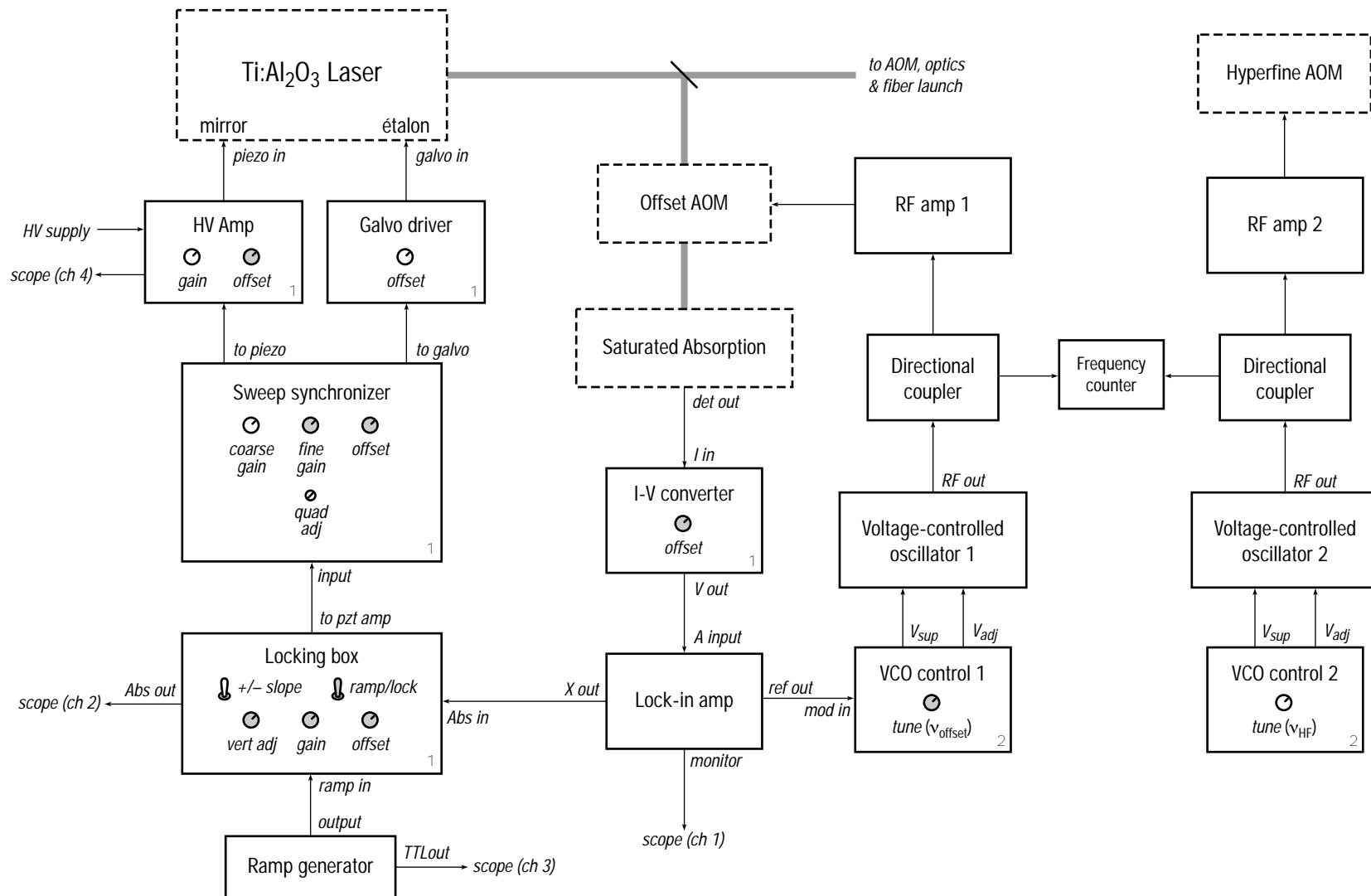


FIGURE A.2: Block diagram of our unique Ti:Al₂O₃ laser locking scheme.

$4^2S_{1/2} \rightarrow 4^2P_{1/2} (\nu = 770.1098 \text{ nm})$
 $4^2S_{1/2} \rightarrow 4^2P_{3/2} (\nu = 766.7017 \text{ nm})$

$F \rightarrow F'$	f (MHz)	$F \rightarrow F'$	f (MHz)
$2 \rightarrow 1'$	-207.9	$2 \rightarrow 1'$	-189.1
$2 \rightarrow 1' 2'$	-180.1	$2 \rightarrow 1' 2'$	-184.45
$2 \rightarrow 2'$	-152.3	$2 \rightarrow 2'$	-179.8
$1 2 \rightarrow 1'$	22.95	$2 \rightarrow 2' 3'$	-169.3
$1 2 \rightarrow 1' 2'$	50.75	$2 \rightarrow 3'$	-158.8
$1 2 \rightarrow 2'$	78.55	$1 2 \rightarrow 0' 1'$	40.15
$1 \rightarrow 1'$	253.8	$1 2 \rightarrow 1'$	41.75
$1 \rightarrow 1' 2'$	281.6	$1 2 \rightarrow 0' 2'$	44.8
$1 \rightarrow 2'$	309.4	$1 2 \rightarrow 1' 2'$	46.4
		$1 2 \rightarrow 2'$	51.05
		$1 2 \rightarrow 1' 3'$	56.9
		$1 2 \rightarrow 2' 3'$	61.55
		$1 \rightarrow 0'$	269.4
		$1 \rightarrow 0' 1'$	271
		$1 \rightarrow 1'$	272.6
		$1 \rightarrow 1' 2'$	277.25
		$1 \rightarrow 2'$	281.9

FIGURE A.3: Transitions in saturated absorption spectroscopy of ^{39}K . The notation “1 2” refers to crossover transitions in the SA spectrum.

driver is from Cambridge Technology, Inc.

Let us again examine Figure A.2, this time considering the locking box as the gain portion of a feedback loop. Amplifier RF amp 1 drives the offset AOM whose center frequency ν_{offset} is adjusted for the appropriate isotope of potassium. Imposed on this frequency is a small modulation generated by the lock-in amplifier (Stanford Research Systems Model 810), allowing the lock-in to generate the derivative of the saturated absorption peak. This derivative signal (“X out”) is used as an error signal for the feedback loop to lock the laser. With this simple technique, we can keep the laser locked for many hours with an average linewidth of 4 MHz FWHM.

A.3 Saturated absorption spectroscopy

Here we simply present the saturated absorption spectroscopy transitions in potassium to which we lock our laser. Preston [1996] has provided an excellent introduction to saturated absorption spectroscopy written at the undergraduate level. Two papers providing a detailed theoretical analysis of saturated absorption line shapes for the D_1 and D_2 transitions in the alkalis have been written by Nakayama [1984, 1985].

The table in Figure A.3 labels all of the observed frequencies for the D_1 and D_2 lines in ^{39}K , showing both direct peaks and crossovers. Note that because the ground-state hyperfine splitting is smaller than the Doppler linewidth (about 900 MHz for our hot cell), we observe crossover transitions not just between pairs of excited state levels, but also between pairs of ground state levels as well. We lock our laser to the $4^2S_{1/2}(F=1) \rightarrow P_{3/2}$ transition, which is unresolved. Locking to the derivative spectrum using a dithered signal and lock-in amplifier gives us about ± 3 MHz knowledge of our lock location.

In figures A.4 and A.5 we present measured spectra, taken using the setup shown in Figure 6.13, with linearly polarized light in both the pump and probe beams, and the orientation adjusted to enhance the overall height of the peaks. The traces represent an average of about 10 sweeps, digitized and summed using our LeCroy 9310 digital oscilloscopes. Although the spectra do not represent completely conditions, they do represent typical spectra useful for locking our lasers. The theoretical transition frequencies are indicated by vertical lines; long lines represent ^{39}K transitions, short ones represent ^{41}K transitions.

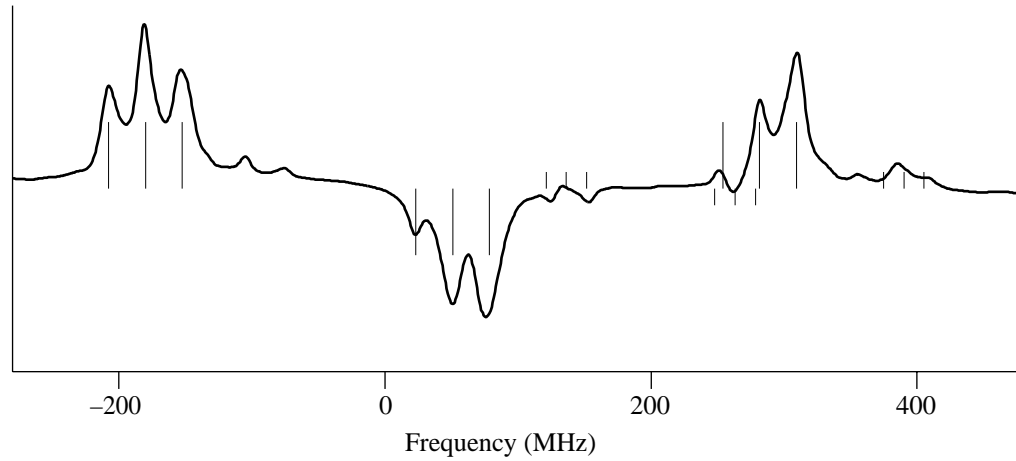


FIGURE A.4: Measured saturated absorption spectra of ^{39}K and ^{41}K $S_{1/2} \rightarrow P_{1/2}$ transition.

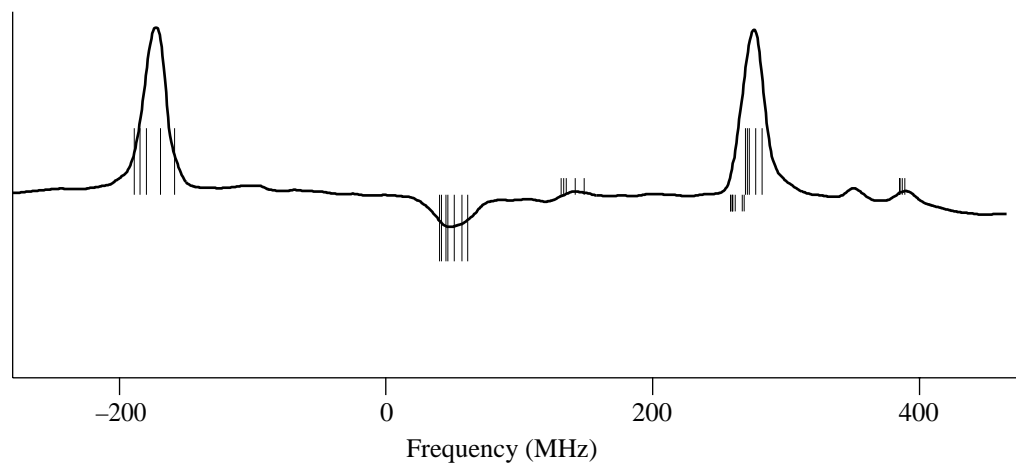


FIGURE A.5: Measured saturated absorption spectra of ^{39}K and ^{41}K $S_{1/2} \rightarrow P_{3/2}$ transition. Vertical lines indicate calculated peak locations; long lines for ^{39}K and short lines for ^{41}K .

Appendix B

Ultrasensitive detection scheme

While target development was progressing, we pursued a short side project intended to create an ultrasensitive detection scheme potentially capable of observing a single trapped atom. One group has already detected single trapped atoms [Hu and Kimble, 1994], but this experiment benefitted from having plenty of atoms available to load an extremely weak MOT. The single atoms were detected using the fluorescence of the trapped atom, detected just as we normally do. However, these single-atom MOTs are made weak by reducing the laser intensity used, which also significantly reduces the amount of stray light scattered into the detector.

At this point, we introduced a liquid-nitrogen-cooled CCD camera as part of the detection system that would soon become necessary for detection of the rarer isotope ^{40}K and of other radioactive isotopes we will produce.

We use a liquid-nitrogen cooled CCD camera* for sensitive detection. We convert from counts to the number of atoms in a manner analogous to equation 2.24

$$N_{\text{atoms}} = \frac{C g_{\gamma} \tau}{t_{\text{exp}} \eta_{\Omega} \eta_{\text{opt}} \rho_e}, \quad (\text{B.1})$$

where

τ is the excited-state lifetime of the atom

ρ_e is the excited-state fraction, calculated using our six-level rate equation model

*Princeton Instruments model LN/CCD-512-TKB/1; it uses a back-illuminated SiTE (Tektronix) detector.

C is the number of counts generated by the A-D converter and sent to the computer

$g_{\gamma c}$ is the number of photons per count (or ADU, analog-to-digital units, as referred to by Princeton Instruments); for the amplifiers in our particular unit, it is 2.2, 4.3, and $8.7 e^-/\text{count}$ in the most, middle, and least sensitive settings

η_{opt} is the optical efficiency; note that in addition to the external optical losses including the lens, the camera alone has six uncoated surfaces from three glass windows, one between the lens and shutter to protect the shutter, one to provide a vacuum seal for the camera, and one mounted to the CCD inside the vacuum

t_{exp} is the exposure time of the shutter; note this large shutter is rather slow and has an inherent lag of 12 ms beyond the nominal exposure time, thus $t_{\text{exp}} = t_{\text{nom}} + 12 \text{ ms}$. Exposures shorter than 200 ms suffer from significant smearing of the image across the CCD and this must be taken into account.

Finally, the solid angle, using our 50 mm Nikon lens, is

$$\eta_{\Omega} = \frac{1}{16} \left(\frac{50/f_{\#}}{o} \right)^2, \quad (\text{B.2})$$

where $f_{\#}$ is the f -stop of the camera, and o is the object-lens distance. The image-object distance d is more readily measured from the experimental geometry, and since we know that the back principal plane of the lens is 51.6 mm from the back focus, $o = d - 51.6 \text{ mm}$.

In the case of ^{40}K or radioactive isotopes made on-line, the source of atoms is extremely feeble and a large amount of laser power is needed to efficiently load the trap; reducing the laser power would result in even fewer atoms. By adding a second laser wavelength to excite the atoms from the $P_{3/2}$ state to a higher level, we can stimulate the atoms to fluoresce at a wavelength far removed from the trapping wavelength, allowing us to filter the unruly trapping light away.

The excitation scheme we use for this is shown in the level diagram in Figure B.1. The two trapping laser frequencies constantly cycle the atoms between the $4S_{1/2}$ and $4P_{3/2}$ levels, with an excited state fraction ρ_e in the $P_{3/2}$ level of typically 0.1–0.4 for

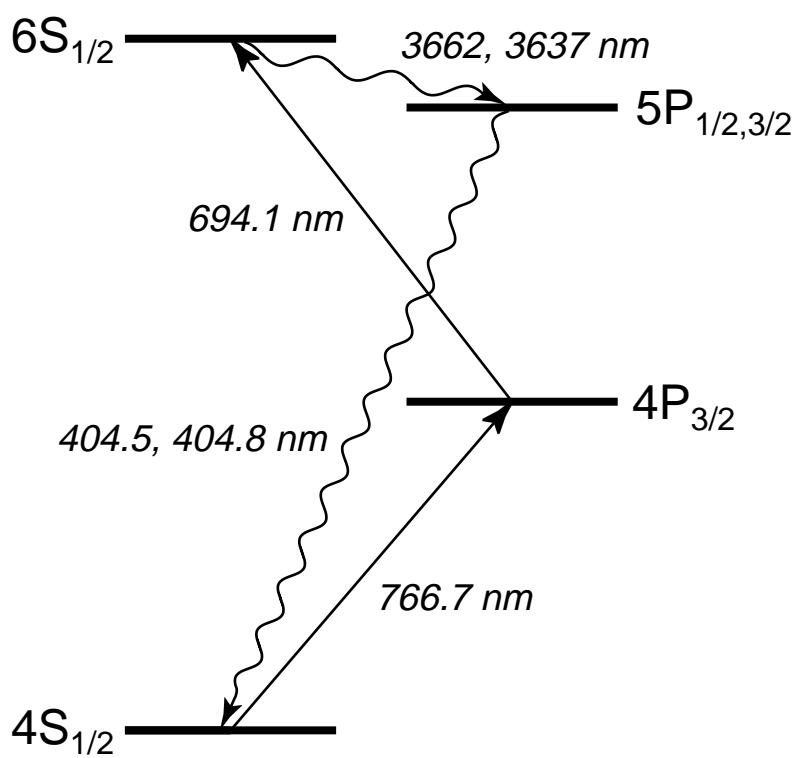


FIGURE B.1: Atomic level scheme for ultrasensitive blue photon detection.

our trap laser detunings and intensities. We further excite some of these atoms by adding another laser tuned to the 694.1 nm $4P_{3/2} \rightarrow 6S_{1/2}$ transition. They promptly decay to the $5P_{1/2,3/2}$ levels from which they again decay to the $4S_{1/2}$ level, emitting an ultraviolet photon at 404 nm.

To produce the 694 nm light we built an external-cavity diode laser, using a very simple-to-machine and build design, based on the collective design experience of the members of the lab and myself.[†] We use a 30 mW 690 nm laser diode[‡] which we heat slightly to get near 694 nm. The cavity consists of the diode, collimating lens and holder (of our own design) and a mirror mount to which is mounted a grating and piezo actuator. The grating is used in the Littrow configuration, and adjusting the mirror mount provides coarse laser tuning. Fine tuning is done by using a low-voltage piezo stack, which adjusts the length of the short (2 cm) laser cavity. The laser puts out roughly 5 mW, which is more than enough for this purpose.

For these initial experiments, the laser was tuned on transition using a Burleigh WA-1500 wavemeter with an absolute accuracy of 50 MHz.[§] In the future it should be possible to stabilize the laser by locking it to the two-photon transition by using a potassium vapor cell illuminated with trapping light and looking for absorption of the 694 nm laser light.

[†]This design has also become popular with a fellow research group because of its straightforward design.

[‡]Mitsubishi model ML1412R

[§]The WA-1500 is a “moving-cart Michelson interferometer” that sends a stabilized HeNe reference laser and the test laser through nearly identical optical paths. By changing the path length and counting and comparing the number of fringes of each laser to within a fraction of a fringe, this device can measure wavelengths to within a few tens of MHz. We have actually built a similar device, but it is much less convenient to use than the Burleigh.

Appendix C

Procedure for coating glass with SC-77 dryfilm coating

Here we describe the procedure used to coat our funnel cell (§5.4) with dryfilm. All of the glass surfaces of the pieces shown in Figure 5.4 were coated.

It is important that the glassware be carefully cleaned before dryfilming. The first step is to clean all surfaces to be coated with Alconox cleaner* and hot water, scrubbing thoroughly. Rinse all traces of cleaner with hot water, then follow with two rinses each of distilled water, methanol, acetone, and methanol again.

The final cleaning step is to use a solution which is also used to remove dryfilm coatings [Fedchak et al., 1997]; we have chosen this one because it is relatively benign† and can be safely used on glass-to-metal seals. It consists of 45% ethanol, 45% distilled water, and 10% KOH by volume. The solution is mixed thoroughly and pieces are placed in it directly or it is poured into the vessel to be coated and allowed to soak for a few hours. To strip previously dryfilmed pieces, we recommend allowing an overnight soak followed by ultrasonic agitation. The pieces are then dried overnight or in a clean 80–100°C oven for about an hour. The pieces must be very clean and dry before applying the dryfilm coating or it will be cloudy.

Our recipe for dryfilming with SC-77 is similar to that of others [Fedchak et al., 1997; Stephens et al., 1994; Swenson and Anderson, 1988]. We are able to get optically

*Fisher Scientific Co., cat. no. 04-322-4

†Other groups have used dryfilm stripping solutions of hydrofluoric acid or ammonium bifluoride [Stephens et al., 1994] or a solution affectionately called “piranha” [Voytas, 1996], because it eats flesh rather quickly.

clear, durable coatings with this method. A glass jar is carefully cleaned with Alconox and rinsed with distilled water and ethanol and distilled water again. Then put 5 mL of distilled water into the jar. Add 10 mL of SC-77 (dichlorodimethylsilane, or DCDMS)[‡]; the reaction occurs with vigorous bubbling and evolution of HCl gas. Allow it to react for 10 s, then cover the jar with a rubber stopper and glass tube. Place the vessel to be coated over the tube and allow the vapor to deposit. The time for deposition depends on the total surface area; we have an area of roughly 150 cm² and find that 30 s exposure works well. The coating should be invisible. Before continuing, the piece is allowed to ‘rest’ for an hour or so to allow the evolved HCl gas to dissipate.

We do all of our coating work inside a nitrogen-purged glove bag which itself is inside a fume hood. The fume hood is necessary to remove the noxious HCl fumes that are generated by the reaction, and the nitrogen-purged glovebag is needed to keep the humidity low while the dryfilm is being deposited. In climates with lower ambient humidity this may be unnecessary. Low ambient humidity appears to be an important factor in producing optically clear coatings.

We then use an after-wash procedure described by Fedchak et al. [1997] who did AFM scans of a dryfilmed surface before and after passivation, showing significant reduction in the surface roughness. The after-wash begins as a solution of 95% methanol and 5% deionized water to which a small amount of acetic acid is added to reduce the pH to 4.5–5.5. The solution is allowed to rest for about 5 minutes and 2% trimethylmethoxysilane[§] is added and the mixture stirred. This is poured into the glassware (or the piece is soaked in it) and allowed to stand for 2 minutes. The solution is poured out and the piece is rinsed with methanol.

The coating is then cured in a vacuum oven for a few hours at about 200°C at 10⁻³ torr. Heavy hydrocarbons will be evolved which can damage or clog ion pumps and gauges, so the use of a sorption pump or a liquid-nitrogen trapped roughing pump is recommended. Once this is done, the coating is stable and will outgas at a rate of about 2 · 10⁻¹⁰ torr l s⁻¹ cm⁻² [Stephens et al., 1994].

You can test the coating by putting a few drops of distilled water on the surface. It should bead up tightly and not wet the surface as you would see on clean, uncoated glassware. At this point the pieces can be installed in the final vacuum system, and a second type of curing is done by extended exposure of the dryfilm to a vapor of alkali

[‡]Silar Laboratories, Scotia, NY, cat. no. 0077

[§]Silar Laboratories, cat. no. 1282

(10^{13} atom s^{-1} cm^{-2}). This is necessary because all dryfilm coatings react quickly with the alkali at first, then 'cures' to a constant reaction rate [Stephens et al., 1994].

Bibliography

- Govind P. Agrawal. *Nonlinear fiber optics*. Academic Press, Boston, 1989.
- O. Ames, E. A. Phillips, and S. S. Glickstein. Spin, hyperfine structure, and nuclear magnetic dipole moment of 23-sec Na²¹. *Physical Review B* **137**, 1157–63, 1965.
- Davide I. Andrea. A high voltage, high speed DC amplifier for piezoelectric crystal driving applications. Unpublished, 1988.
- M. R. Andrews, C. G. Townsend, H.J. Miesner, D. S. Durfee, D. M. Kurn, and W. Ketterle. Observation of interference between two Bose condensates. *Science* **275**, 637–41, 1997.
- E. Arimondo, M. Inguscio, and P. Violino. Experimental determinations of the hyperfine structure in the alkali atoms. *Reviews of Modern Physics* **49**, 31–76, 1977.
- A. Ashkin and J. P. Gordon. Stability of radiation-pressure particle traps: an optical Earnshaw theorem. *Optics Letters* **8**, 511–3, 1983.
- F. Bardou, O. Emile, J.-M. Courty, C. I. Westbrook, and A. Aspect. Magneto-optical trapping of metastable helium: collisions in the presence of resonant light. *Europhysics Letters* **20**, 681–6, 1992.
- Thomas E. Barrett, Samuel W. Daport-Schwartz, Mark D. Ray, and Gregory P. Lafaytis. Slowing atoms with σ^- polarized light. *Physical Review Letters* **67**, 3483–6, 1991.
- J. A. Behr, A. Gorelov, T. Swanson, O. Häusser, K. P. Jackson, M. Trinczek, U. Giesen, J. M. D’Auria, R. Hardy, T. Wilson, P. Choboter, F. Leblond, L. Buchmann, M. Dombisky, C. D. P. Levy, G. Roy, B. A. Brown, and J. Dilling. Magneto-optic trapping of β -decaying ³⁸K^m, ³⁷K from an on-line isotope separator. *Physical Review Letters* **79**, 375–8, 1997.
- N. Bendali, H. T. Duong, and J. L. Vialle. High-resolution laser spectroscopy on the D_1 and D_2 lines of ^{39,40,41}K using RF modulated laser light. *Journal of Physics B* **14**, 4231–40, 1981.

- H. J. Besch, U. Köpf, E.-W. Otten, and Ch. von Platen. Nuclear magnetic moment of ^{37}K . *Physics Letters B* **26**, 721–2, 1968.
- C. C. Bradley, C. A. Sackett, and R. G. Hulet. Bose-Einstein condensation of lithium: observation of limited condensate number. *Physical Review Letters* **78**, 985–9, 1997.
- C. C. Bradley, J. G. Story, J. J. Tollett, J. Chen, N. W. M. Ritchie, and R. G. Hulet. Laser cooling of lithium using relay chirp cooling. *Optics Letters* **17**, 349–51, 1992.
- Thomas A. Carlson, C. W. Nestor Jr., Thomas C. Tucker, and F. B. Malik. Calculation of electron shake-off for elements from $Z = 2$ to 92 with the use of self-consistent-field wave functions. *Physical Review* **169**, 27–36, 1968.
- Yat Chan and Natarajan D. Bhaskar. Cooling of cesium atomic beam with light from spectrally broadened diode lasers. *Journal of the Optical Society of America B* **12**, 2347–51, 1995.
- S. Chu, J. Bjorkholm, A. Ashkin, and A. Cable. Experimental observation of optically trapped atoms. *Physical Review Letters* **57**, 314, 1986.
- S. Chu, L. Hollberg, J. Bjorkholm, A. Cable, and A. Ashkin. Three-dimensional viscous confinement and cooling of atoms by resonance radiation pressure. *Physical Review Letters* **55**, 48, 1985.
- E. D. Commins and P. H. Bucksbaum. *Weak interactions of leptons and quarks*. Cambridge University Press, Cambridge, 1983.
- Jules Deutsch and Paul Quin. Symmetry-tests in semileptonic weak interactions: a search for new physics. In Paul Langacker, editor, *Precision tests of the standard electroweak model*, volume 14 of *Advanced series on directions in high energy physics*, pages 706–65. World Scientific, New Jersey, 1995.
- O. Dulieu, P. Julienne, and J. Weiner. Accuracy of molecular data in the understanding of ultracold collisions. *Physical Review A* **49**, 607–10, 1994.
- W. Ertmer, R. Blatt, J. L. Hall, and M. Zhu. Laser manipulation of atomic beam velocities: demonstration of stopped atoms and velocity reversal. *Physical Review Letters* **54**, 996–9, 1985.
- J. A. Fedchak, P. Cabuay, W. J. Cummings, C. E. Jones, and R. S. Kowalczyk. Silane coatings for laser-driven polarized hydrogen sources and targets. *Nuclear Instruments and Methods in Physics Research A* **395**, 1997.
- Paul Feng, Dominikus Hoffmann, and Thad Walker. Comparison of trap-loss collision spectra for ^{85}Rb and ^{87}Rb . *Physical Review A* **47**, R3495–8, 1993.

- J. Flemming, A. M. Tuboy, D. M. B. P. Milori, L. G. Marcassa, S. C. Tilio, and V. S. Bagnato. Magneto-optical trap for sodium atoms operating on the D_1 line. *Optics Communications* **135**, 269–72, 1997.
- K. E. Gibble, S. Kasapi, and S. Chu. Improved magneto-optic trapping in a vapor cell. *Optics Letters* **17**, 526–8, 1992.
- Kurt Gibble, Seongsik Chang, and Ronald Legere. Direct observation of s-wave atomic collisions. *Physical Review Letters* **75**, 2666–9, 1995.
- G. Gwinner, J. A. Behr, S. B. Cahn, A. Ghosh, L. A. Orozco, G. D. Sprouse, and F. Xu. Magneto-optical trapping of radioactive ^{79}Rb . *Physical Review Letters* **72**, 3795–8, 1994.
- T. Hänsch and A. Schawlow. Cooling of gases by laser radiation. *Optics Communications* **13**, 68, 1975.
- D. Hoffmann, P. Feng, R. S. Williamson III, and T. Walker. Excited-state collisions of trapped ^{85}Rb atoms. *Physical Review Letters* **69**, 753–6, 1992.
- J. Hoffnagle. Proposal for continuous white-light cooling of an atomic beam. *Optics Letters* **13**, 102–4, 1988.
- B. R. Holstein. *Weak interactions in nuclei*. Princeton University Press, Princeton, 1989.
- Z. Hu and H. J. Kimble. Observation of a single atom in a magneto-optical trap. *Optics Letters* **19**, 1888–90, 1994.
- D. S. Jin, M. R. Matthews, J. R. Ensher, C. E. Wieman, and E. A. Cornell. Temperature-dependent damping and frequency shifts in collective excitations of a dilute Bose-Einstein condensate. *Physical Review Letters* **78**, 764–7, 1997.
- Hidetoshi Katori and Fujio Shimizu. Laser cooling and trapping of argon and krypton using diode lasers. *Japanese Journal of Applied Physics* **29**, L2124–6, 1990.
- Wolfgang Ketterle, Kendall B. Davis, Michael A. Joffe, Alex Martin, and David E. Pritchard. High densities of cold atoms in a dark spontaneous-force optical trap. *Physical Review Letters* **70**, 2253–6, 1993.
- Wolfgang Ketterle, Alex Martin, Michael Joffe, and David E. Pritchard. Slowing and cooling atoms in isotropic laser light. *Physical Review Letters* **69**, 2483–6, 1992.
- Thomas J. Killian. Thermionic phenomena caused by vapors of rubidium and potassium. *Physical Review* **27**, 578–87, 1926.

- J. A. Kim, K. I. Lee, H. R. Noh, W. Jhe, and M. Ohtsu. Atom trap in an axicon mirror. *Optics Letters* **22**, 117–9, 1997.
- Takayuki Kurosu and Fujio Shimizu. Laser cooling and trapping of calcium and strontium. *Japanese Journal of Applied Physics* **29**, L2127–9, 1990.
- K. I. Lee, J. A. Kim, H. R. Noh, and W. Jhe. Single-beam atom trap in a pyramidal and conical hollow mirror. *Optics Letters* **21**, 1177–9, 1996.
- Zhong Lin, Kazuko Shimizu, Mingsheng Zhan, Fujio Shimizu, and Hiroshi Takuma. Laser cooling and trapping of Li. *Japanese Journal of Applied Physics* **30**, L1324–6, 1991.
- K. Lindquist, M. Stephens, and C. Wieman. Experimental and theoretical study of the vapor-cell Zeeman optical trap. *Physical Review A* **46**, 4082–90, 1992.
- Z.-T. Lu, C. J. Bowers, S. J. Freedman, B. K. Fujikawa, J. L. Mortara, S.-Q. Shang, K. P. Coulter, and L. Young. Laser trapping of short-lived radioactive isotopes. *Physical Review Letters* **72**, 3791–4, 1994.
- Z.-T. Lu, K. L. Corwin, M. J. Renn, M. H. Anderson, E. A. Cornell, and C. E. Wieman. Low-velocity intense source of atoms from a magneto-optical trap. *Physical Review Letters* **77**, 3331–4, 1996.
- Z.-T. Lu, K. L. Corwin, K. R. Vogel, C. E. Wieman, T. P. Dineen, J. Maddi, and Harvey Gould. Efficient collection of ^{221}Fr into a vapor cell magneto-optical trap. *Physical Review Letters* **79**, 994–7, 1997.
- J. H. McNally. Reactions leading to ^{37}Ar and ^{37}K energy levels. *Nuclear Physics* **88**, 257–72, 1966.
- J. D. Miller, R. A. Cline, and D. J. Heinzen. Far-off-resonance optical trapping of atoms. *Physical Review A* **47**, R4567–70, 1993.
- C. Monroe, W. Swann, H. Robinson, and C. Wieman. Very cold trapped atoms in a vapor cell, 1990.
- P. N. Murgatroyd and Bruce E. Bernard. Inverse Helmholtz pairs. *Review of Scientific Instruments* **54**, 1736–8, 1983.
- C. J. Myatt, N. R. Newbury, R. W. Ghrist, S. Loutzenhiser, and C. E. Wieman. Multiply loaded magneto-optical trap. *Optics Letters* **21**, 290–2, 1996.
- Shigeru Nakayama. Theoretical analysis of Rb and Cs D_2 lines in saturation spectroscopy with optical pumping. *Japanese Journal of Applied Physics* **23**, 879–83, 1984.

- Shigeru Nakayama. Doppler-free laser spectroscopic techniques with optical pumping in D_1 lines of alkali atoms. *Journal of the Optical Society of America B* **2**, 1431–7, 1985.
- J. Nellesen, J. Werner, and W. Ertmer. Magneto-optical compression of a monoenergetic sodium atomic beam. *Optics Communications* **78**, 300–8, 1990.
- Renée Nesnidal. Calculation of energies in positive beta decay. unpublished, 1995.
- Quang-Viet Nguyen, Robert W. Dibble, and Timothy Day. High-resolution oxygen absorption spectrum obtained with an external-cavity continuously tunable diode laser. *Optics Letters* **19**, 2134–6, 1994.
- Daryl Preston. Doppler-free saturated absorption: laser spectroscopy. *American Journal of Physics* **64**, 1432–6, 1996.
- E. L. Raab, M. Prentiss, Alex Cable, Steven Chu, and D. E. Pritchard. Trapping of neutral sodium atoms with radiation pressure. *Physical Review Letters* **59**, 2631–4, 1987.
- Norman F. Ramsey. *Molecular beams*. Oxford University Press, Oxford, 1956.
- Erling Riis, David S. Weiss, Kathryn A. Moler, and Steven Chu. Atom funnel for the production of a slow, high-density atomic beam. *Physical Review Letters* **64**, 1658–61, 1990.
- Nicholas William M. Ritchie. *A study of collisional trap loss in ultra-cold trapped lithium-6 and lithium-7 (lithium)*. PhD thesis, Rice University, 1994.
- Alexander Roth. *Vacuum technology*. Elsevier Science Publishers, The Netherlands, 1982.
- M. S. Santos, P. Nussenzveig, L. G. Marcassa, K. Helmerson, J. Flemming, S. C. Zilio, and V. S. Bagnato. Simultaneous trapping of two different atomic species in a vapor-cell magneto-optical trap. *Physical Review A* **52**, R4340–3, 1995.
- Milton D. Scheer, Ralph Klein, and John D. McKinley. Surface lifetimes of alkali metals on molybdenum. *Journal of Chemical Physics* **55**, 3577–84, 1971.
- Giacinto Scoles, editor. *Atomic and molecular beam methods*, volume 1. Oxford University Press, New York, 1988.
- K. Sengstock, U. Sterr, G. Hennig, D. Bettermann, J. H. Müller, and W. Ertmer. Optical Ramsey interferences on laser cooled and trapped atoms, detected by electron shelving. *Optics Communications* **103**, 73–8, 1993.

- D. Sesko, T. Walker, C. Monroe, A. Gallagher, and C. Wieman. Collisional losses from a light-force atom trap. *Physical Review Letters* **63**, 961–4, 1989.
- B. Sheehy, S.-Q. Shang, R. Watts, S. Hatamian, and H. Metcalf. Diode-laser deceleration and collimation of a rubidium beam. *Journal of the Optical Society of America B* **6**, 2165–70, 1989.
- Fujio Shimizu, Kazuko Shimizu, and Hiroshi Takuma. Laser cooling and trapping of Ne metastable atoms. *Physical Review A* **39**, 2758–60, 1989.
- J. E. Simsarian, A. Ghosh, G. Gwinner, L. A. Orozco, G. D. Sprouse, and P. A. Voytas. Magneto-optic trapping of ^{210}Fr . *Physical Review Letters* **76**, 3522–5, 1996a.
- J. E. Simsarian, W. Shi, L. A. Orozco, G. D. Sprouse, and W. Z. Zhao. $7\text{S}_{1/2} \rightarrow 9\text{S}_{1/2}$ two-photon spectroscopy of trapped francium. *Optics Letters* **21**, 1939–41, 1996b.
- R. G. Smith. Optical power handling capacity of low loss optical fibers as determined by stimulated Raman and Brillouin scattering. *Applied Optics* **11**, 2489–94, 1972.
- M. Stephens, R. Rhodes, and C. Wieman. Study of wall coatings for vapor-cell laser traps. *Journal of Applied Physics* **76**, 3479–88, 1994.
- T. B. Swanson, N. J. Silva, S. K. Mayer, J. J. Maki, and D. H. McIntyre. Rubidium atomic funnel. *Journal of the Optical Society of America B* **13**, 1833–6, 1996.
- D. R. Swenson and L. W. Anderson. Relaxation rates for optically pumped Na vapor on silicone surfaces. *Nuclear Instruments and Methods in Physics Research* **29**, 627–42, 1988.
- F. Touchard, P. Guimbal, S. Büttgenbach, R. Klapisch, M. De Saint Simon, J. M. Serre, C. Thibault, H. T. Duong, P. Juncar, S. Liberman, J. Pinard, and J. L. Vialle. Isotope shifts and hyperfine structure of $^{38-47}\text{K}$ by laser spectroscopy. *Physics Letters B* **108**, 169–71, 1982.
- C. G. Townsend, N. H. Edwards, K. P. Zetie, C. J. Cooper, J. Rink, and C. J. Foot. High-density trapping of cesium atoms in a dark magneto-optical trap. *Physical Review A* **53**, 1702–14, 1996.
- Wim Vassen, Claus Zimmermann, Reinald Kallenbach, and Theodor Hänsch. A frequency-stabilized titanium-sapphire laser for high-resolution spectroscopy. *Optics Communications* **75**, 435–40, 1990.
- Paul A. Voytas. Personal communication, 1996.
- Paul Andrew Voytas. *A target for producing polarized ^{21}Na by optical pumping*. PhD thesis, University of Wisconsin – Madison, 1993.

- M. Walhout, H. J. L. Megens, A. Witte, and S. L. Rolston. Magneto-optical trapping of metastable xenon: isotope-shift measurements. *Physical Review A* **48**, R879–82, 1993.
- T. Walker. Three-dimensional analytical calculation of the magneto-optical trapping forces on a stationary $J = 0 \rightarrow J = 1$ atom. *Laser Physics* **4**, 965–8, 1994.
- T. Walker and P. Feng. Measurements of collisions between laser-cooled atoms. *Advances in Atomic, Molecular, and Optical Physics* **34**, 125, 1993.
- T. Walker, P. Feng, D. Hoffmann, and R. S. Williamson III. Spin-polarized spontaneous-force atom trap. *Physical Review Letters* **69**, 2168–71, 1992a.
- T. Walker, D. Hoffmann, P. Feng, and R. S. Williamson III. A vortex-force atom trap. *Physics Letters A* **163**, 309–12, 1992b.
- T. Walker and D. Pritchard. Effects of hyperfine structure on alkali trap-loss collisions. *Laser Physics* **4**, 1085–92, 1994.
- Thad Walker, David Sesko, and Carl Wieman. Collective behavior of optically trapped neutral atoms. *Physical Review Letters* **64**, 408–11, 1990.
- H. Wang, P. L. Gould, and W. C. Stwalley. Photoassociative spectroscopy of pure long-range molecules. *Zeitschrift für Physik D* **36**, 317–23, 1996a.
- H. Wang, P. L. Gould, and W. C. Stwalley. Photoassociative spectroscopy of ultracold ^{39}K atoms in a high-density vapor-cell magneto-optical trap. *Physical Review A* **53**, R1216–9, 1996b.
- H. Wang, J. Li, X. T. Wang, C. J. Williams, P. L. Gould, and W. C. Stwalley. Precise determination of the dipole matrix element and radiative lifetime of the ^{39}K $4p$ state by photoassociative spectroscopy. *Physical Review A* **55**, R1569–72, 1997.
- R. N. Watts and C. E. Wieman. Manipulating atomic velocities using diode lasers. *Optics Letters* **11**, 291–3, 1986.
- W. L. Wiese and G. A. Martin, editors. *Wavelengths and Transition Probabilities for Atoms and Atomic Ions, Part II, Transition Probabilities*. U.S. Government Printing Office NSRDS-NBS 68, Washington, 1980.
- P. A. Willems and K. G. Libbrecht. Creating long-lived neutral atoms traps in a cryogenic environment. *Physical Review A* **51**, 1403–6, 1995.
- R. S. Williamson III, P. A. Voytas, and T. Walker. A funnel-loaded magneto-optic trap. Preprint (unpublished), 1997.

- R. S. Williamson III and T. Walker. Magneto-optical trapping and ultracold collisions of potassium atoms. *Journal of the Optical Society of America B* **12**, 1393–7, 1995.
- J. Yu, J. Djemaa, P. Nosbaum, and P. Pillet. Funnel with orientated Cs atoms. *Optics Communications* **112**, 136–40, 1994.
- X. Zeng, Z. Wu, T. Call, E. Miron, D. Schreiber, and W. Happer. Experimental determination of the rate constants for spin exchange between optically pumped K, Rb, and Cs atoms and ^{129}Xe nuclei in alkali-metal–noble-gas van der Waals molecules. *Physical Review A* **31**, 260–78, 1985.
- W. Z. Zhao, J. E. Simsarian, L. A. Orozco, W. Shi, and G. D. Sprouse. Measurement of the $7p^2P_{3/2}$ level lifetime in atomic francium. *Physical Review Letters* **78**, 4169–72, 1997.
- M. Zhu, C. W. Oates, and J. L. Hall. Continuous high-flux monovelocity atomic beam based on a broadband laser-cooling technique. *Physical Review Letters* **67**, 46–9, 1991.

Index

- Agrawal [1989], 98
- alignment, 107
 - of trapping beams, 50
- Ames et al. [1965], ix, 86, 87
- Andrea [1988], 113
- Andrews et al. [1997], 56
- angular momentum, 6, 59
- anti-Helmholtz coils, 48
- AOM, 22
- apparatus
 - beam-loaded, 44
 - funnel-loaded, 68
 - vapor-loaded, 21
- apparatus, target, 88
- Arimondo et al. [1977], 11, 78
- Arrhenius, 91
- Ashkin and Gordon [1983], 5
- asymmetry measurements, 74
- asymmetry parameter, 76
- atomic beam, 2
 - cold, 59
 - thermal, 38
- atomic funnel, 8
 - others, 57
- axicon, 59
- Bali, Samir, iii
- ballistic expansion, 26
- Bardou et al. [1992], 9
- Barrett et al. [1991], 43, 57
- Beer's law, 14
- Behr et al. [1997], 28, 74, 79
- Bendali et al. [1981], 11, 78
- Besch et al. [1968], 78
- beta asymmetry, 2
- beta decay, 74
- bounces, 104
- bounces in cell, 65
- Bradley et al. [1992], 43
- Bradley et al. [1997], 56
- Brillouin scattering, 98
- Cabbibo, 74
- calcium, 87
- calcium oxide, 87
- capture efficiency, 41
- capture velocity, 10, 14, 19, 79
 - Doppler limit, 42
- Carlson et al. [1968], 110
- CCD camera
 - cooled, 118
 - to measure trap density, 31
- chamber
 - beam-loaded, 46
 - funnel, 61
 - vapor-cell, 22
- Chan and Bhaskar [1995], 43
- channelling of gas, 97
- chirped
 - cooling, 43
 - slowing, 58
- Chu et al. [1985], 4
- Chu et al. [1986], 2
- collimation, 42
- collision rate
 - isotopic difference, 36
 - versus trap density, 31
- collisional rate coefficient, 31
 - versus detuning, 35
- collisions, 29

- with background gas, 54
- Commins and Bucksbaum [1983], 74
- copper, 61
- crossover transitions, 116
- current-to-voltage converter, 22
- cylindrical channel, 39
- desorption energy, 91
- detuning
 - definition, 16
 - definition of, 15
 - for various isotopes, 80
 - range of funnel, 70
- deuteron beam, 96
- Deutsch and Quin [1995], 73
- differential pumping, 68, 96
- diffusion time, 87
- diode laser, 7
 - 694 nm, 121
 - not available for potassium, 31
- Doppler
 - effect, 4
 - limit, 41
 - shift, 19
- “Drag”, iii
- dryfilm, 65, 72, 122
- Dulieu et al. [1994], 36
- Earnshaw theorem, 4
- efficiency, overall, 101
- effusive source, 38
- electrostatic optics, 91
- Ertmer et al. [1985], 43
- étalon, 99, 112
- excitation rates, 17
- excited-state
 - collisions, 29
 - fraction, 15
- Fedchak et al. [1997], 122, 123
- Feng et al. [1993], 36
- Feng, Paul, ii
- Flemming et al. [1997], 13, 84
- fluorescence, 31
- force
 - model calculation, 18
 - on atom, 10
- funnel
 - construction details, 61
 - diagram, 60
 - operating as MOT, 66, 71
- Gamov-Teller transition, 76
- gas conductance, 97
- gas load, 96
- Gibble et al. [1992], 16
- Gibble et al. [1995], 57
- glass capillary array, 42
- glass liner, 61
- gold electroplate, 61
- Gower, Melissa Erin, iv
- graphite, 92
- Gwinner et al. [1994], 73
- Havar, 95
- hermetically sealed, 112
- Hoffmann et al. [1992], 7, 31
- Hoffmann, Dominik, ii
- Hoffnagle [1988], 43
- Holstein [1989], 74
- Hu and Kimble [1994], 118
- hyperfine structure, 10, 13, 79
 - small, 16
- Hänsch and Schawlow [1975], 4
- intensity
 - of light in funnel, 68
- isotope shift, 11, 110
- isotopes
 - abundant, 10
- isotropic slowing, 43
- Jhe, Won-ho, 58
- Jin et al. [1997], 56
- Kadlecek, Steve, iii
- Katori and Shimizu [1990], 10

- Ketterle et al. [1992], 43
 Ketterle et al. [1993], 31
 Killian [1926], 13
 Kim et al. [1997], 59, 71
 Kurosu and Shimizu [1990], 9
- Landé g -factors, 81
- laser
 - beam diameter, 19
 - catalysis, 31
 - locking, 21
 - stabilization, 113
- leaky-MOT, 58
- Lee et al. [1996], 8, 58, 59, 71, 107
- lifetime of trap, 54
- Lin et al. [1991], 9, 80
- Lindquist et al. [1992], 16, 18, 25
- lithium, 10, 80
- Littrow configuration, 121
- loading
 - benefits of direct, 44
 - of potassium-40, 84
 - problems with vapor, 57
- loading rate
 - efficiency of funnel, 71
 - from effusive beam, 51
 - funnel cell, 70, 107
 - model, 19
 - model results, 23, 25
 - of axicon, 59
 - of funnel cell, 103
 - vapor, 15
 - versus beam diameter, 25
 - versus detuning, 23
 - versus intensity, 25
 - with longitudinal slowing, 52
- locking box, 113
- locking of laser, 21
- loss rate, 23, 30
- Lu et al. [1994], 73
- Lu et al. [1996], 8, 57, 58
- Lu et al. [1997], 74
- LVIS, 58
- magnesium, 86
- magnetic field
 - coils
 - main gradient, 46
 - shim and bucking, 48
 - funnel coil configuration, 65
 - gradient, 25
 - little effect on model, 19
 - shim, 22
- magnetic field coils, 46
- Maxwell-Boltzmann distribution, 14, 26, 41
- McNally [1966], 86
- Miller et al. [1993], 31
- mirror decay, 76
- molecular spectroscopy, 29
- Monroe et al. [1990], 15, 20, 36, 57, 104
- MOT
 - 3D, 6
 - cesium, vapor-loaded, 16
 - first, 2
 - for other atoms, 10
 - potassium
 - others, 27
 - sodium, 13
 - vapor-cell, 13
- MOT, radioactive, 2
- Murgatroyd and Bernard [1983], 48
- Myatt et al. [1996], 57
- Nakayama [1984], 116
- Nakayama [1985], 116
- Nellessen et al. [1990], 57
- Nelson, Ian, iii
- Nesnidal [1995], 110
- Nesnidal, Renée, ii
- Newton, 19
- Nguyen et al. [1994], 21, 112
- Nikon lens, 119
- normalization of populations, 18
- nuclear magnetic moments, 10

- nuclear spin, 17
- optical breadboard, 101
- optical fiber, 98
- optical molasses
 - first, 4
 - moving, 58
 - transverse, 43
- optical pumping, 3, 10, 15, 73, 81
- oscillator strength, 79
- oscillator strengths, 16
- oven
 - Ames-style, 86
 - our design, 91
- oven, our scheme, 88
- oxygen absorption line, 21, 112
- particle diameter, 88
- photodiode, 22
- polarization-gradient cooling, 27
- populations, level, 17
- potassium
 - hyperfine structure, 110
 - unique, 10
 - vapor pressure, 13
- power broadening, 10, 79
- pressure
 - operation of funnel at high, 72
 - ultimate limit, 97
- Preston [1996], 116
- prism, for retroreflection, 22
- production mechanism, 101
- pyramidal mirror, 59
- pyrex, 61
- Quin, Paul, ii
- Raab et al. [1987], 9, 13, 81
- radiation-trapping, 30
- radioactive target, 8
- radioactive trapping by other groups, 74
- Ramsey [1956], 14, 39
- rate-equation model, 15
- release and recapture, 26
- Riis et al. [1990], 57, 58
- Ritchie [1994], 36
- Roth [1982], 97
- SAES getter, 90
- sailing, ii
- Santos et al. [1995], 27
- saturated absorption, 21, 116
- saturation intensity, 15, 18
- Scheer et al. [1971], 91
- Scoles [1988], 39
- Sengstock et al. [1993], 9
- Sesko et al. [1989], 9
- Sheehy et al. [1989], 43
- Shimizu et al. [1989], 10
- silicon dioxide, 61
- silicon photodiode, 22
- Simpson's rule, 20
- Simsarian et al. [1996a], 73, 92
- Simsarian et al. [1996b], 73
- Sisyphus effect, 27
- Slotten, Ed, iii
- slowing, 42, 52
- Smith [1972], 98
- sodium, 84
- solid angle, 23, 77
- spectroscopy, 2
- spin polarization, 76
- spin-polarized trap, 7
- spontaneous force, 3, 19
- standard model, 2
- Standard Model, 74
- Stephens et al. [1994], 72, 91, 122–124
- stopping distance, 20
- Sukenik, Charles, iii
- Swanson et al. [1996], 57, 58
- Swenson and Anderson [1988], 122
- symmetry tests, 73
- systematic errors, 3
- tantalum, 88, 92

- target vacuum system, 92
- temperature, of trap, 26
- thin-walled orifice, 38
- Ti:sapphire, 7, 21, 111
- titanium sublimation pump, 46
- Touchard et al. [1982], 78
- Townsend et al. [1996], 31
- transfer efficiency, 71, 103, 106, 107
- transport efficiency, 101
- trap
 - density, 22, 30, 31
 - measurement, 33
 - double system, 57
 - optimization, 50
 - temperature, 26
- trapping beam, effective diameter of, 20
- TSP, 46
- two-level atom, 3, 15

- ultracold collisions, 29
- undesirable gas, 42

- vacuum chamber
 - desiderata, 46
 - figure of main, 46
- vapor cell, 99
- vapor pressure, 13
- Vassen et al. [1990], 112
- velocity
 - mean thermal, 104
 - most probable, 14
- velocity distribution
 - of atomic beam, 41
- viewports, 44
- vitriation, 92
- Voytas [1993], 77
- Voytas [1996], 122
- Voytas, Paul, ii, 91

- Walhout et al. [1993], 10
- Walker and Feng [1993], 29
- Walker and Pritchard [1994], 35
- Walker et al. [1990], 30
- Walker et al. [1992a], 7, 110
- Walker et al. [1992b], 7, 9
- Walker [1994], 59
- Walker, Thad, ii
- Wang et al. [1996a], 27
- Wang et al. [1996b], 27
- Wang et al. [1997], 17, 27
- Watts and Wieman [1986], 43
- Wiese and Martin [1980], 17
- Willems and Libbrecht [1995], 98
- Williamson III and Walker [1995], 7, 17, 30, 70
- Williamson III et al. [1997], 8
- wind, ii
- windsurfing, ii
- Wisconsin, ii

- XHV, 7

- yttrium foil, 92
- Yu et al. [1994], 57

- Zeeman
 - levels, 81
 - shift, 6
 - splitting
 - of various isotopes, 81
 - sublevels, 5, 15
 - tuned slower, 43
- Zeng et al. [1985], 13
- Zhao et al. [1997], 73
- Zhu et al. [1991], 43